

**MULTI-SPACECRAFT STUDIES
OF PLASMA BOUNDARIES AT MARS**

*Thesis submitted for the degree of
Doctor of Philosophy
at the University of Leicester*

by

Niklas Johan Theodor Edberg
Department of Physics and Astronomy
University of Leicester

September 2009

Abstract

Multi-spacecraft studies of plasma boundaries at Mars by Niklas Johan Theodor Edberg

We study the solar wind interaction with Mars and the location, shape, dynamics and controlling factors of the magnetic pileup boundary (MPB) and the bow shock (BS), which form as a result of this interaction, by using single as well as two-spacecraft measurements.

By using Mars Global Surveyor (MGS) measurements we produce statistical models of the shapes of the two boundaries. The influence on the boundaries from the crustal magnetic fields of Mars is also studied. We find that the MPB is pushed to higher altitudes depending on the strength of the underlying crustal fields while the BS is found at higher altitudes over the entire southern hemisphere of Mars, where the crustal fields are strongest.

By using the simultaneous measurements from Rosetta and Mars Express (MEX) we study the boundaries during high and low solar wind dynamic pressure. During low pressure, simultaneous two-spacecraft measurements provide leverage on the accuracy of the shape of the MPB and BS. Their previously modelled shapes are found to be in agreement with the shapes derived from these two-point measurements. During high pressure, we observe how the boundaries become asymmetric in their shapes, possibly due to increased plasma outflow over one hemisphere, which lowers the plasma pressure on that side of the planet and results in an asymmetric shape.

By using MGS and MEX measurements we study the altitude of the boundaries as functions of solar wind dynamic pressure, solar EUV flux and crustal magnetic field strength. We also examine the effect of the direction of the interplanetary magnetic field on the boundaries. We find that the dynamic pressure, EUV flux and crustal magnetic fields are the main governing factors of both the MPB and the BS.

Acknowledgements

First of all I wish to thank my excellent supervisor Mark Lester for always providing useful input when needed but also for allowing me to roam freely within the realm of Mars and explore and study whatever I have found interesting. I am also very grateful to my second adviser Stan Cowley for many questions answered.

During the fall of 2007 I was given the opportunity to visit Anders Eriksson at the Swedish Institute of Space Physics in Uppsala, Sweden. For this I am also very grateful. The result from that visit now constitutes a large fraction of this thesis. It also enabled me to catch my breath back in Sweden. With newly gathered strength from the homeland, I visited David Brain at the Space Sciences Laboratory of UC Berkeley, USA, during the fall of 2008. I owe David many thanks for taking me in and enlightening me on many things related to the science of Mars but also on many things related to the non-science part of science. I would not have been able to finish my thesis without those two visits.

Furthermore, I wish to thank Ronan Modolo for always providing help and comments. Stas Barabash and Markus Fränz are greatly acknowledged for letting me use, and helping me getting started with, Mars Express ASPERA-3 data. The MGS MAG/ER and Rosetta RPC teams are also acknowledged for providing me with their data.

On a more personal note, I have had the fortunate opportunity to experience a life in the UK for three years. Curries, tea breaks (coffee, really), pub trips, cricket, football, rugby, movie nights and poker nights as well as the wonder of wall-to-wall carpeting have truly fulfilled my time. For this I especially wish to thank the many members of the RSPP group. Thanks to you all!

Finally, I also wish to thank Karin for sharing a life in science as well as in the real world.

Declaration

The following papers have been produced during the time of these doctoral studies, out of which the first four constitute the bulk of this Thesis

- I. **Edberg, N. J. T.**, Lester, M., Cowley, S. W. H. and Eriksson, A. I., Statistical analysis of the location of the Martian magnetic pileup boundary and bow shock and the influence of crustal magnetic fields, *J. Geophys. Res.*, 113, A08206, 2008
- II. **Edberg, N. J. T.**, Eriksson, A. I., Auster, U., Barabash, S., Boesswetter, A., Carr, C. M., Cowley, S. W. H., Cupido, E., Fränz, M., Glassmeier, K.-H., Goldstein, R., Lester, M., Lundin, R., Modolo, R., Nilsson, H., Richter, I., Samara, M. and Trotignon, J. G., Simultaneous measurements of Martian plasma boundaries by Rosetta and Mars Express, *Planet. Space Sci.*, 57, 1085-1096, doi:10.1016/j.pss.2008.10.016, 2009
- III. **Edberg, N. J. T.**, Brain, D. A., Lester, M., Cowley, S. W. H., Modolo, R., Fränz, M. and Barabash, S., Plasma boundary variability at Mars as observed by Mars Global Surveyor and Mars Express, *Ann. Geophys.*, 27, 3537-3550, 2009
- IV. **Edberg, N. J. T.**, Auster, U., Barabash, S., Boesswetter, A., Brain, D. A., Burch, J. L., Carr, C. M., Cowley, S. W. H., Cupido, E., Duru, F., Eriksson, A. I., Fränz, M., Glassmeier, K.-H., Goldstein, R., Lester, M., Lundin, R., Modolo, R., Nilsson, H., Richter, I., Samara, M. and Trotignon, J. G., Rosetta and Mars Express observations of the influence of high solar wind dynamic pressure on the Martian plasma environment, Submitted to *Ann. Geophys.*, 2009
- V. Boesswetter, A., Auster, U., Richter, I., Fränz, M., Langlais, B., Simon, S., Motschmann, U., Glassmeier, K.-H., **Edberg, N. J. T.**, and Lundin, R., Rosetta swing-by at Mars - an analysis of the ROMAP

measurements in comparison with results of 3d multi-ion hybrid simulations and MEX/ASPERA-3 data, *Ann. Geophys.*, 27, 2383-2398, 2009

- VI. Odzimek, A., Clausen, L. B. N., Kanawade, V., Cnossen, I., **Edberg, N. J. T.**, Faedi, F., Del Moro, A., Ural, U., Byckling, K., Krzaczkowski, P., Iwanski, R., Struzik, P., Pajek, M., and Gajda, W., SPARTAN Sprite-Watch Campaign 2007, In: 15th Young Scientists Conference on Astronomy and Space Physics. Proceedings of Contributed Papers, edited by V.Ya. Choliy and G. Ivashchenko, Logos, Kyiv, pp. 64-67, 2009.
- VII. Iwanski, R., Odzimek, A., Clausen, L.B.N., Kanawade, V., Cnossen, I., **Edberg, N. J. T.**, Meteorological study of the first observation of red sprites from Poland, *Acta. Geophysica*, 57-3, 760-777, 2009.
- VIII. Eriksson, A. I., Gill, R., Wahlund, J.-E., Andre, M., Mälkki, A., Lybekk, B., Pedersen, A., Holtet, J. A., Blomberg, L. G., and **Edberg, N. J. T.**, RPC-LAP: The Langmuir probe instrument of the Rosetta plasma consortium, In *Rosetta: ESA's mission to the origin of the solar system*, eds. R. Schulz, C. Alexander, H. Boehnhardt and K.-H. Glassmeier, pp. 435-447. Springer, ISBN: 97 8-0-387-77517-3. doi:10.1007/978-0-387-77518-0_15_4, 2009

Contents

1	Introduction	1
1.1	Space plasma physics	2
1.1.1	Magnetohydrodynamics	2
1.1.2	Frozen-in flow	2
1.1.3	Parker spiral	4
1.1.4	Gyro-motion and $\mathbf{E} \times \mathbf{B}$ - drift	4
1.1.5	Debye length	7
1.1.6	Thermal, kinetic and magnetic pressure	8
1.2	The planet Mars	9
1.3	The solar wind interaction with Mars	11
1.3.1	The ionosphere and the photo-electron boundary	11
1.3.2	The bow shock and magnetic pileup boundary	14
1.3.3	The tail region	21
1.3.4	Crustal magnetic fields	22
1.3.5	Global models of the Martian plasma environment	25
1.3.6	Erosion of the atmosphere	26
2	Instrumentation	32
2.1	Mars Global Surveyor: magnetometer and electron reflectometer	32
2.2	Mars Express: ASPERA-3 and MARSIS	33
2.3	Rosetta: The Rosetta Plasma Consortium	37
2.4	Moments from ion and electron measurements	39
2.5	Rosetta and Mars Express density cross-calibration	41
3	Mars Global Surveyor measurements of the influence of the crustal magnetic fields	46
3.1	Introduction	46
3.2	Data analysis	47
3.2.1	Shape of bow shock and magnetic pileup boundary	50
3.2.2	The influence of crustal magnetic fields	54

3.2.3	Magnetic field strength at the magnetic pileup boundary	61
3.3	Summary and conclusions	64
4	Rosetta and Mars Express simultaneous measurements of the effects of low and high solar wind pressure	68
4.1	Introduction	69
4.2	Simultaneous observations during low solar wind pressure	69
4.2.1	Dayside bow shock crossing	71
4.2.2	Dayside MPB and PEB crossings	72
4.2.3	Flank MPB crossing	75
4.2.4	Flank magnetosheath and bow shock crossings	77
4.2.5	Mars Express observations	79
4.3	Shape and location of the plasma boundaries	82
4.4	Simultaneous observations during high pressure solar wind	86
4.4.1	Plasma boundary asymmetries	88
4.4.2	Cause of the asymmetries	95
4.4.3	Ion outflow and exosphere asymmetry	99
4.5	Boundary asymmetry linked to the ionospheric outflow	103
4.6	Summary and conclusions	107
5	Mars Express and Mars Global Surveyor measurements	111
5.1	Introduction	111
5.2	Measurements of and proxies for the dynamic pressure, IMF direction and solar EUV flux	112
5.3	Mars Express and Mars Global Surveyor observations	115
5.4	Case studies with simultaneous measurements	116
5.5	Statistical studies with simultaneous measurements	124
5.5.1	Influence of the solar wind dynamic pressure	124
5.5.2	Influence of the IMF direction	128
5.6	Influence of the crustal magnetic fields	131
5.7	Influence of the solar EUV flux	135
5.8	Summary and conclusions	136
6	Conclusions & future work	141
6.1	Conclusions	141
6.2	Future work	144

Chapter 1

Introduction

The Sun continuously emits plasma into space which forms the solar wind. The solar wind consists of mainly hydrogen and helium ions and electrons which propagate radially outward from the Sun. It continues to propagate outward into the solar system until it either encounters the interstellar medium at the edge of the solar system or it encounters a planetary body. It is this solar wind's interaction with planet Mars that is the topic of this Thesis. The average density of the solar wind is on the order of $\sim 2 \text{ cm}^{-3}$ at Mars and the average speed on the order of $\sim 400 \text{ km s}^{-1}$. The Sun also possesses a magnetic field which is convected outward by the solar wind forming the interplanetary magnetic field (IMF), which at Mars is on the order of $\sim 3 \text{ nT}$.

In this Chapter we will first describe the basic physics of the solar wind plasma and the general properties of the planet Mars before we summarize some of the key features which arise from the solar wind interaction with Mars.

1.1 Space plasma physics

1.1.1 Magnetohydrodynamics

The equations that describe the properties of the particles, currents and electric and magnetic fields that exist in the magnetised solar wind plasma are Maxwell's equations together with the equations for conservation of mass, momentum and energy in the so called magnetohydrodynamic (MHD) approximation. The plasma is then treated as a fluid and kinetic phenomena cannot be resolved. Maxwell's equations are given by

$$\nabla \cdot \mathbf{E} = \frac{\rho_q}{\epsilon_0} \quad (1.1)$$

$$\frac{\partial \mathbf{B}}{\partial t} = -\nabla \times \mathbf{E} \quad (1.2)$$

$$\nabla \times \mathbf{B} = \mu_0 \mathbf{j} + \mu_0 \epsilon_0 \frac{\partial \mathbf{E}}{\partial t} \quad (1.3)$$

$$\nabla \cdot \mathbf{B} = 0, \quad (1.4)$$

where \mathbf{E} is the electric field, ρ_q is the charge density, ϵ_0 is the permittivity of free space, \mathbf{B} is the magnetic field, t is the time, μ_0 is the permeability of free space and \mathbf{j} is the current density. For low-frequency phenomena it can be assumed that there are no displacement currents and the second term on the right hand side in Equation 1.3 can be dropped (this condition is not satisfied for e.g. radio waves).

1.1.2 Frozen-in flow

An important feature of the IMF is that it can be considered to be frozen into the solar wind plasma and hence travels with the solar wind. In order

to explain this we need to first consider Ampère's law

$$\mathbf{j} = \frac{\nabla \times \mathbf{B}}{\mu_0}, \quad (1.5)$$

and conclude that the size of the current density is on the order of

$$j \sim \frac{B}{\mu_0 L}, \quad (1.6)$$

where L is the scale length on which the magnetic field varies significantly.

Ohm's law gives

$$\mathbf{E} = -\mathbf{v} \times \mathbf{B} + \mathbf{j}/\sigma, \quad (1.7)$$

where \mathbf{v} is the bulk velocity of the plasma and σ is the conductivity, and by taking the curl of this and using Faraday's law (Equation 1.2) and Ampère's law (Equation 1.3) we obtain the induction equation

$$\frac{\partial \mathbf{B}}{\partial t} = \nabla \times (\mathbf{v} \times \mathbf{B}) + \eta \nabla^2 \mathbf{B}, \quad (1.8)$$

where $\eta = \frac{1}{\mu_0 \sigma}$. The first term on the right hand side of Equation 1.8 describes convection of \mathbf{B} with \mathbf{v} ('frozen-in' flow) and the second term is the magnetic diffusion. The dimensionless ratio of the first and second term is the magnetic Reynolds number

$$R_m = \frac{vL}{\eta} = \mu_0 \sigma v L, \quad (1.9)$$

which is a very large number ($\sim 10^6 - 10^{12}$) for most situations in the solar wind. On scales L such that R_m is very large then Equation 1.8 reduces to

$$\frac{\partial \mathbf{B}}{\partial t} \sim \nabla \times (\mathbf{v} \times \mathbf{B}), \quad (1.10)$$

and the magnetic field can therefore be considered to be frozen into the plasma. Ohm's law (Equation 1.7) then reduces to

$$\mathbf{E} + \mathbf{v} \times \mathbf{B} = 0, \quad (1.11)$$

where \mathbf{E} is sometimes called the convective electric field or motional electric field (note that the same result is obtained if the conductivity in equation 1.7 goes to infinity). As a consequence of Equation 1.10, the solar wind particles that are fixed within a magnetic flux tube at a certain time will always stay within that flux tube, as long as the frozen-in condition holds (e.g. across current sheets).

1.1.3 Parker spiral

Since the IMF is connected to the rotating Sun the magnetic field forms a spiral shape in interplanetary space. The magnetic field continuously propagates radially outward, frozen into the solar wind while still connected to the source region on the Sun, which rotates (with a revolution period of ~ 24 - 27 days, depending on latitude). This results in a spiral shape of the IMF known as the Parker spiral. The Parker spiral shape of the IMF is shown schematically in Figure 1.1. In particular, this means that at Mars the IMF is normally oriented in the ecliptic plane with an angle of 57° from the Sun-Mars line.

1.1.4 Gyro-motion and $\mathbf{E} \times \mathbf{B}$ - drift

There are many drifts and motions of plasma particles in the presence of an electric field \mathbf{E} and a magnetic field \mathbf{B} in space. We will not describe them

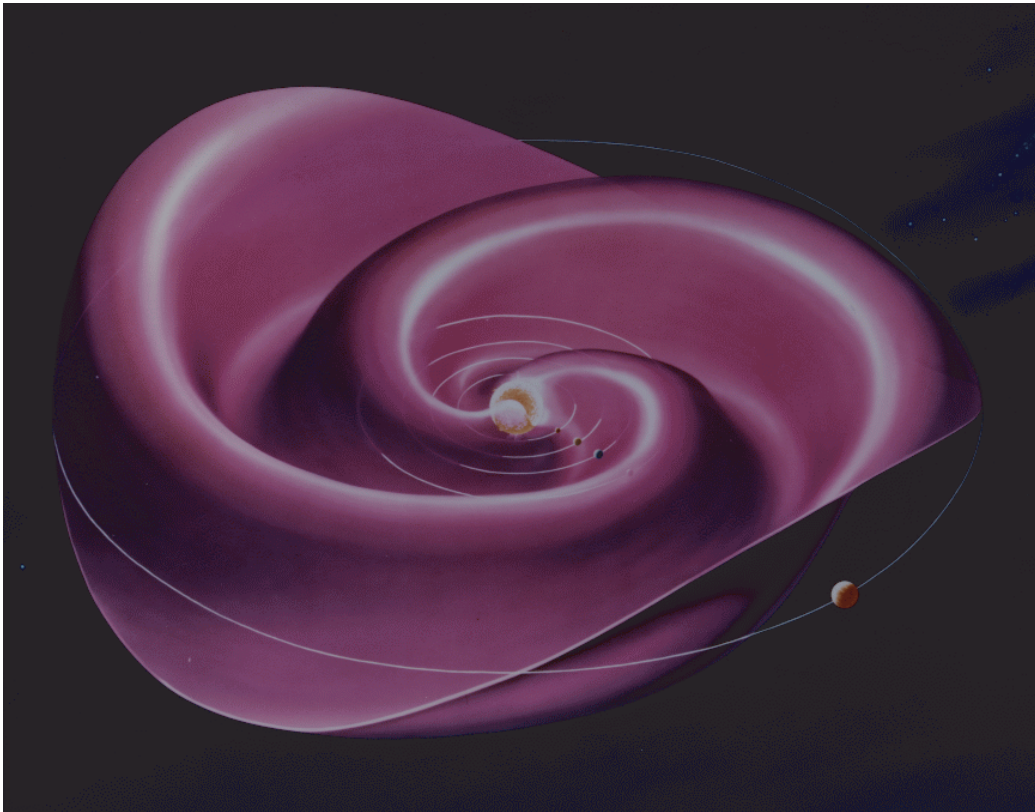


Figure 1.1: A schematic representation of the Parker spiral of the IMF. Mercury, Venus, Earth, Mars and Jupiter and their orbits are also shown in the figure. Courtesy of NASA.

all but rather focus on two of them in the following Section.

The Lorentz forces that act upon a single particle with charge q and velocity \mathbf{v} are

$$\mathbf{F} = q(\mathbf{E} + \mathbf{v} \times \mathbf{B}). \quad (1.12)$$

Applying this to Newton's second law

$$\mathbf{F} = m\mathbf{a}, \quad (1.13)$$

where m is the mass and \mathbf{a} is the acceleration gives

$$m \frac{d\mathbf{v}}{dt} = q(\mathbf{E} + \mathbf{v} \times \mathbf{B}). \quad (1.14)$$

Solving the above differential equation in the direction parallel and perpendicular to the magnetic field, gives rise to the two characteristic movements. First, the perpendicular components results in a motion where the ions and electrons gyrate around the magnetic field lines with a gyro frequency

$$\omega_c = \frac{qB}{m}, \quad (1.15)$$

and a gyro radius

$$r_c = \frac{mv_{\perp}}{qB}, \quad (1.16)$$

where v_{\perp} is the velocity component perpendicular to the magnetic field.

The second movement comes from the parallel components of Equation 1.14. The particles are accelerated by the electric field, in the direction of the electric field for the positively charged ions and in the opposite direction of the electric field for the negatively charged electrons. During one complete gyro-

cycle the magnetic force, always being perpendicular to the motion of the particle, averages out. But the electric force is always in the same direction. This leads to the gyro-motion of the particle not forming a perfect circle. On one half of each gyration is the particle accelerated by the electric field and on the other half is it being decelerated such that the particle travels a longer distance on one half than the other. This leads to a drift motion of the particles in a direction perpendicular to both \mathbf{E} and \mathbf{B}

$$\mathbf{v}_{E \times B} = \frac{\mathbf{E} \times \mathbf{B}}{B^2}. \quad (1.17)$$

Ions and electrons, with opposite charge, gyrate in different directions while their drifts, in a collisionless plasma, are in the same direction independent of charge q and mass m .

1.1.5 Debye length

In a plasma, a single ion whose electrostatic potential is

$$\Phi(r) = \frac{q}{4\pi\epsilon_0 r}, \quad (1.18)$$

where r is the radial distance, will attract electrons while ions, with their larger masses, will be only somewhat repelled. This will change the potential to

$$\Phi(r) = qe^{-r/\lambda_D}/(4\pi\epsilon_0 r), \quad (1.19)$$

where

$$\lambda_D = \left(\frac{\epsilon kT}{nq^2} \right)^{1/2} \quad (1.20)$$

is the Debye length, T is the temperature and k is Boltzmann's constant. In a cloud of plasma particles where a Maxwellian distribution of the energy of the particles can be assumed we get collective behaviour of the plasma rather than a collection of individual particles. The Debye sphere is then a shielding sphere of radius λ_D outside of which charges and electric fields are screened off. The Debye length is a useful quantity since it is a measure of the length over which charge separation can occur and the distance over which a charge separation influence its surroundings. In the solar wind this quantity is typically on the order of ~ 10 m. The charge-density separation between electrons and ions also gives rise to an oscillation of the particles with a plasma frequency

$$\omega_{ps} = \left(\frac{nq^2}{\epsilon_0 m} \right)^{1/2}. \quad (1.21)$$

1.1.6 Thermal, kinetic and magnetic pressure

Finally, there are three types of pressure associated with the solar wind plasma. First, the thermal gas pressure is

$$p_{Th} = n_e k T_e + n_i k T_i, \quad (1.22)$$

where n_i and n_e are the ion and electron densities and T_i and T_e the ion and electron temperatures, respectively. The magnetic pressure is

$$p_B = \frac{B^2}{2\mu_0} \quad (1.23)$$

and the dynamic pressure

$$p_{Dym} = \rho v^2, \quad (1.24)$$

where ρ is the mass density.

1.2 The planet Mars

The planet Mars is the fourth planet from the Sun and the second smallest of all planets in the solar system with a radius of 3397 km and a mass of $6.4 \cdot 10^{23}$ kg ($\sim 11\%$ of the Earth's mass). Consequently, the gravitational acceleration on Mars is 3.72 m s^{-2} . The orbit of Mars is more elliptic than the Earth's orbit and its distance from the Sun varies between 1.37 AU and 1.67 AU (1 AU = $1.5 \cdot 10^8$ km = the average Sun-Earth distance). The orbital period (a Martian year) is 687 days and a revolution period (a Martian day or a 'sol') is 24h 40 min making a Martian year 668 sols. Mars's revolution axis is tilted by 25° , which is similar to the Earth's tilt of 23° , and hence there are spring, summer, autumn, and winter seasons on Mars as well.

The atmosphere of Mars is very different from that at Earth. The surface pressure is only 0.007 bars and the main constituents are carbon dioxide, CO_2 (95.3%), nitrogen, N_2 (2.7%) and argon, Ar (1.6%). There is very little oxygen, O_2 (0.13%) and even less water, H_2O (0.03%). Clouds can form on Mars and even snowfall has been detected by the recent Phoenix Mars lander mission. The polar regions are also covered by water ice and carbon dioxide ice, which sublimates in the summer and freezes again in the winter.

Mars does not possess a global intrinsic dipole-like magnetic field like the Earth but it does have strong crustal magnetic sources, which will be described in more detail in Section 1.3.4.

Over the past 50 years, there have been more than 40 attempts to send spacecraft missions to Mars. Only about 50% of these reached Mars and



Figure 1.2: A spacecraft image of planet Mars. Courtesy of NASA.

could be labelled successful and not all of these successful missions carried plasma instruments. Out of the ones that did carry plasma instruments we should mention Phobos 2 (arrived 1989), Mars Global Surveyor (MGS) (arrived 1997), Mars Express (MEX) (arrived 2003) and Rosetta (swingby 2007), which will all be referred to extensively in this Thesis.

1.3 The solar wind interaction with Mars

When the solar wind encounters a planet or any other major body in the solar system a complex interaction region is formed. This interaction region is characterized by various different plasma regimes with distinct boundaries. The solar wind interaction with celestial bodies is usually divided into three cases: interaction with a magnetised body, as for the case of Earth and the gas giant planets such as Jupiter and Saturn, interaction with a non-magnetised body with no significant atmosphere, as for the Moon and asteroids, and finally, interaction with a non-magnetised planet with an atmosphere, as for Venus, comets and Mars.

1.3.1 The ionosphere and the photo-electron boundary

The effective obstacle to the solar wind at Mars is the ionosphere. We will therefore first describe the features of the ionosphere before we describe its interaction with the solar wind.

The ionosphere is a thick (~ 200 - 300 km) region in the upper regions of the neutral atmosphere where planetary molecules have been ionised to form a mixture of some ions and electrons and lots of neutral gas. In situ measurements of the Martian ionosphere have only been performed by the two Viking

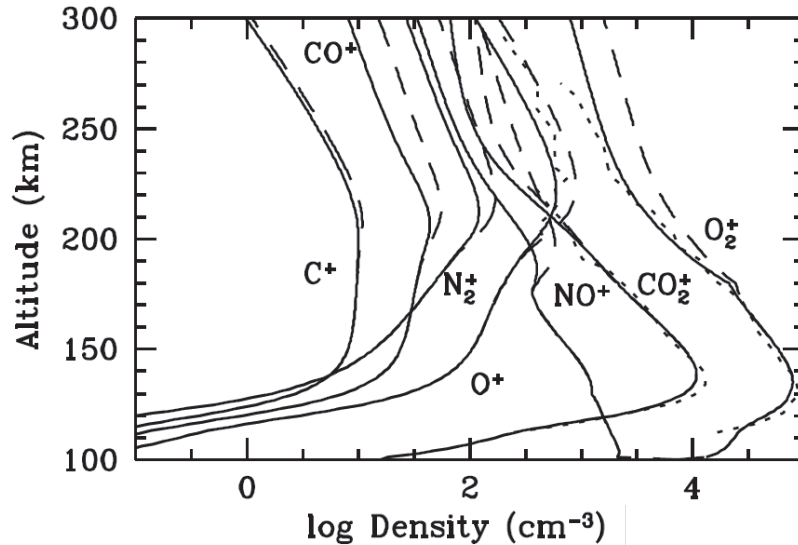


Figure 1.3: Modelled ionospheric altitude-density profiles from Fox (1997) of the most common ion species at Mars computed assuming loss of ions by upward flux (dashed lines) and no flux (solid lines) and measured profiles from the Viking landers (dotted lines) Hanson *et al.* (1977). Reproduced from Fox (1997).

landers (Hanson *et al.*, 1977). The measurements from the Viking landers in terms of altitude profiles of the ion density are shown in Figure 1.3 together with modelled values from Fox (1997). Remote measurements have been more extensive. In particular, thousands of radio occultation measurements from MGS and MEX have been performed during the last decade (Hinson *et al.*, 1999; Pätzold *et al.*, 2005). Furthermore, active ionospheric sounding from MEX have also provided data on the ionosphere. Even though CO_2 is the most common molecule in the atmosphere, CO_2^+ is not the most common ion due its slower ionisation rate (Withers, 2009). The Viking measurements showed that the most abundant ion species in Mars's ionosphere is O_2^+ (Hanson *et al.*, 1977). The peak density of O_2^+ in the ionosphere reaches about 10^5 cm^{-3} at an altitude of $\sim 130 \text{ km}$, as can be seen in Figure 1.3. The shape of

the altitude profiles are in reasonable agreement with what is expected from the commonly used Chapman theory (*Chapman*, 1931a,b). The density increases exponentially with decreasing altitude up to a point, and the density of the main peak falls off with solar zenith angle (SZA) (*Morgan et al.*, 2008; *Withers*, 2009).

The main ionisation source on the dayside of Mars is photoionisation by solar EUV photons which creates the main peak in the altitude profiles. Below the main peak, electron-impact processes and X-ray photons become more important and form a second layer (*Withers*, 2009). At even lower altitudes, meteoritic impacts can create a sporadic third layer (*Pätzold et al.*, 2005). Toward the nightside the ionosphere becomes more and more controlled by electron transport processes from the dayside but since the Martian ionosphere is generally magnetized this transport is rather weak (*Nagy et al.*, 2004). This is, however, an area that is poorly investigated and requires further study. Factors that have been shown to affect the properties of the ionosphere include crustal magnetic fields (*Withers et al.*, 2005) and solar energetic particles (*Espley et al.*, 2007).

At Venus, for instance, the transition into the ionosphere is usually very clear. A sharp increase (on inbound passes) in the ion and electron density, called the ionopause, is clearly visible in spacecraft data. At Mars, this transition is much more smeared out and the term ‘ionopause’ is not really adequate. There is no sharp transition into an ionosphere. A related boundary has, however, been observed by the electron spectrometers onboard MGS and MEX. This is not an ionopause in the normal sense but a boundary where a strong peak in the observed electron spectrum from photoionised CO₂ starts to appear at energies of $\sim 20\text{-}30$ eV. This boundary has been labelled the

photo-electron boundary (PEB) (*Frahm et al.*, 2006). The PEB is located at an altitude of about 250 km on the dayside of Mars and extends to at least 10 000 km downstream of Mars (where the farthest downstream measurements from MEX are made) in a cylindrical shape of approximately the planetary radius (*Frahm et al.*, 2006). The PEB was, however, also noted in earlier data from MGS (*Mitchell et al.*, 2001) but due to the low energy resolution of the electron spectrometer the nature of this boundary remained somewhat unclear until the arrival of MEX (*Frahm et al.*, 2006).

1.3.2 The bow shock and magnetic pileup boundary

The solar wind interaction with Mars leads to the formation of plasma regions with distinct boundaries which are the main topic in this Thesis. These boundaries form at altitudes of $\sim 1-2 R_M$ on the dayside and at even higher altitudes toward the nightside. For the case of an interaction with an unmagnetized body with an atmosphere, such as Mars, the main three boundaries are the bow shock (BS), the magnetic pileup boundary (MPB) and the photo-electron boundary (PEB). Figure 1.4 shows a schematic representation of the global plasma environment of Mars with the main boundaries and regions. The BS is the boundary where the supersonically flowing solar wind rapidly slows down to subsonic speeds and was first detected at Mars by the Mariner 4 spacecraft (*Smith et al.*, 1965). The velocity of the solar wind is faster than the compressional waves (magnetosonic waves) that travel in it and when the flow hits the planet a shock wave must form unless the planet completely absorbs the flow (*Mazelle et al.*, 2004). As the flow slows down the plasma density and magnetic field strength increase to satisfy the conditions of conservation of mass, momentum and energy. Beneath the BS follows a region

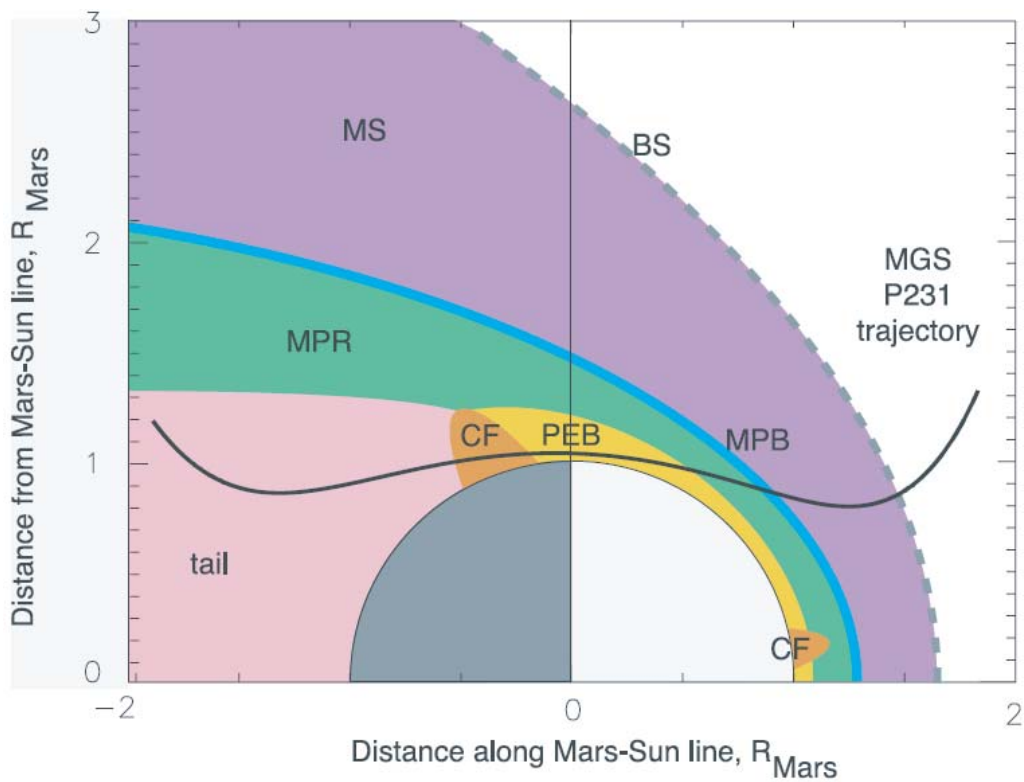


Figure 1.4: A cartoon of the Martian plasma environment showing the location of the various plasma boundaries and regions. A part of the MGS spacecraft trajectory is shown as a black line. Reproduced from Crider *et al.* (2003).

of shocked solar wind called the magnetosheath, characterized by heated and more turbulent solar wind plasma. The Mach number (sonic, magnetosonic and Alfvénic) in the solar wind determines how much deceleration and heating takes place at the BS (*Mazelle et al.*, 2004). The Martian exosphere, which is the uppermost region around Mars where upward travelling molecules can either escape into space if the velocity is high enough or be pulled back to the planet by the gravity, is rather extended outside the BS compared to Venus and Earth due to the low gravity on Mars. This is important as it affects the amount of waves upstream of the BS (*Mazelle et al.*, 2004).

The magnetosheath, downstream of the BS, is separated from the planetary plasma and the magnetic pileup region (MPR) by the MPB. At the MPB the IMF starts to pile up, since it cannot penetrate efficiently into the ionosphere, and drapes around the planet before it slips past around the sides of the obstacle (*Nagy et al.*, 2004). This boundary has been named the planetopause, magnetopause, protonopause or ion-composition boundary depending on which spacecraft sampled it and which instruments it used to measure the characteristics of the boundary (*Trotignon et al.*, 2006). The plasma population differs across this boundary, with mainly solar wind ions in the magnetosheath and planetary ions in the MPR.

Several spacecraft have sampled the Martian plasma environment and the amount of data has increased significantly during the last decade (from 1997) with the measurements from MGS and MEX. *Slavin and Holzer* (1981) presented early work on the shape of the BS at Mars using data from the early ‘Mars’ series of spacecraft. The BS has also been studied using Phobos 2 measurements by *Schwingschuh et al.* (1990) and *Trotignon et al.* (1991, 1993), while the MPB has been studied, referred to as the magnetopause

by *Lundin et al.* (1990), the planetopause by *Trotignon et al.* (1996) and the protonopause by *Sauer et al.* (1992) among others. The instrumentation on board Phobos 2 was more extensive than on MGS, but Phobos 2 did not complete as many orbits and did not provide data with such good spatial coverage as MGS. Also, Phobos 2 had its periapsis at 850 km which was too high to decisively determine the nature of the dayside MPB. The Martian plasma environment could therefore be more extensively studied with the MGS mission. Phobos 2 is the only spacecraft which have carried an instrument for studying electric fields at Mars, which, for instance, showed how the plasma turbulence increased when the BS was crossed and the magnetosheath was entered (*Grard et al.*, 1989).

The coordinate system that has been used to examine the location of the boundaries is the Mars solar orbital (MSO) system, where the x -axis points toward the Sun, the y -axis points approximately opposite to Mars' orbital motion, and the z -axis is directed parallel to the orbital angular momentum vector of Mars (*Slavin and Holzer*, 1981). This coordinate system is rotated by 4° about the z -axis to account for the aberration of the solar wind flow direction by the planetary orbital motion. The method used to determine the shape of the two boundaries developed by *Slavin and Holzer* (1981) has been to fit a conic section

$$r = \frac{L}{1 + \epsilon \cos(\theta)} \quad (1.25)$$

to the crossings, where r and θ are polar coordinates with origin at X_0 referenced to the x -axis, and L and ϵ are the eccentricity and semi-latus rectum, respectively (*Slavin and Holzer*, 1981).

Since the arrival of MGS the shape and structure of both the MPB and BS have been studied in more detail. *Vignes et al.* (2000) published results on the boundary shapes using data from the first year of the pre-mapping phase of the mission. The average position of the boundaries could be determined with more accuracy using the MGS measurements due to the many more crossings than obtained by Phobos 2. *Trotignon et al.* (2006) combined MGS and Phobos 2 data to produce a more realistic boundary shape farther downstream. The models of the BS and MPB from the study by *Trotignon et al.* (2006) are shown in Figure 1.5. *Bertucci et al.* (2005) on the other hand used a minimum variance technique to estimate the local normal vector at each MPB crossing to confirm the shape derived by *Vignes et al.* (2000). Due to the orbit configuration of MGS, no crossings of the MPB were observed below a SZA of $\sim 20^\circ$. This introduced an error in the fitting of a conic section to the boundary when using MGS boundary crossings. The standoff distance at the subsolar point (SZA = 0°) of the empirical models were in fact larger than the distance at SZA = 45° which does not seem reasonable. MEX on the other hand, could later on sample the boundary at lower SZAs and hence correct the problem.

There are a number of factors controlling the location of the MPB and BS. *Rosenbauer et al.* (1994) provided first experimental evidence, using Phobos 2 data, that the magnetic pressure in the Martian tail balanced the upstream solar wind dynamic pressure. *Verigin et al.* (1993) used the same data set to study the influence of the upstream dynamic pressure and magnetic field strength on the boundary locations. *Crider et al.* (2003) used MGS data and studied the variation of the magnetic field strength inside the MPB in the MPR and stated that this could be used as a proxy for upstream dynamic

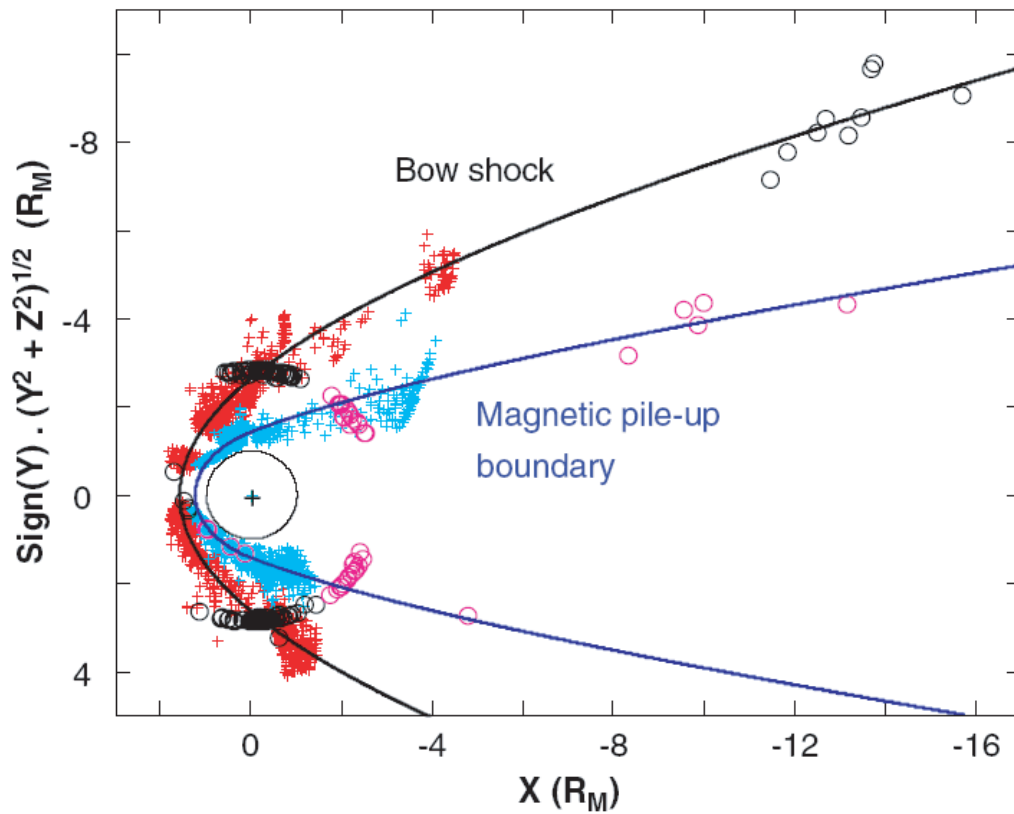


Figure 1.5: Martian BS (black rings) and MPB (purple rings) crossings from Phobos 2 as well as crossings of the BS (red crosses) and MPB (blue crosses) from MGS shown in cylindrical MSO coordinates. Best fit conic section models of the BS (black line) and MPB (blue line) are also shown. Reproduced from Trotignon *et al.* (2006).

pressure. The dynamic pressure as measured upstream of the planet was confirmed, by MEX measurements, to be one of the controlling factors of the location of the MPB when the magnetic pressure of the piled up field in the MPR was shown to balance the dynamic pressure of the solar wind (*Dubinin et al.*, 2006). In between the MPR and the solar wind is the magnetosheath where the thermal pressure balances the magnetic pressure from the inside and the dynamic pressure from the outside (*Dubinin et al.*, 2008a). The large data set from MEX enables a further statistical study of the dependence on upstream solar wind dynamic pressure on the plasma boundaries which is one of the topics in this Thesis (see Chapter 5).

The 11-year solar cycle dependence has proved to be weak since the locations of the MPB and BS were not found to be significantly different in Phobos 2 and MGS measurements which sampled the boundary in different parts of the solar cycle. Phobos 2 sampled the boundaries during the increasing phase of the solar cycle and MGS sampled the boundaries during solar minimum. MEX started sampling the boundaries during the declining phase of the solar cycle as well but will have the opportunity to sample them during solar maximum if it stays alive for another 5 years or so.

The effect of the IMF orientation has been studied and shown to influence the BS location (*Vignes et al.*, 2002). The explanation for this is that the IMF direction determines the direction of the convective electric field (Equation 1.11), which causes magnetosheath ions to move in the direction of the electric field and electrons the opposite way, creating an asymmetry which also causes the shape of the boundary to become asymmetric. However, in the study by *Vignes et al.* (2002) only a small subset of the crossings were used when the IMF was steady. This decreased the number of data points significantly.

As stated above, there are a number of factors that potentially influence the position and shape of the plasma boundaries, such as solar wind dynamic pressure, IMF direction and thermal pressure inside the BS. Added to that list are the crustal magnetic fields of Mars, which will be introduced in Section 1.3.4. All these factors are more or less important, which will be further investigated in Chapter 5, and when they mix with each other it becomes challenging to determine the cause of the dynamics of the boundaries, which will be discussed in Chapter 4.

1.3.3 The tail region

As the IMF piles up at the MPB, the field lines drape around the planet to form the induced tail and central plasma sheet behind the planet. The draped field lines, which are orientated according to the IMF direction on the dayside (*Brain et al.*, 2006), form two lobes of oppositely directed orientation when they meet again behind the planet and a Harris current sheet can form (*Halekas et al.*, 2006; *Halekas and Brain*, 2009). The plasma sheet is oriented according to the IMF direction. This tail extends far behind the planet with BS crossings being observed by Phobos 2 and Mariner 4 at a distance of $15 R_M$ downstream of Mars (*Slavin et al.*, 1991). This was the farthest downstream BS crossing until Rosetta arrived at Mars (see Section 4). MEX data have revealed that the tail region is also characterized by outflowing heavy planetary ions (*Barabash et al.*, 2006), which will be discussed further in Section 1.3.6. One regime of lighter planetary ions are located adjacent to the MPB and gain energies greater than 2000 eV before gradually decreasing in energy downtail, while heavier ions occupy the region in the optical shadow of Mars and are accelerated to the energy of the solar wind (*Fedorov et al.*,

2006).

1.3.4 Crustal magnetic fields

Even if we have classified the Mars solar wind interaction to be that of an unmagnetized body with an atmosphere, analysis of MGS data has indicated that Mars is not totally unmagnetized. MGS measurements did lead to the final conclusion that Mars does not possess an intrinsic global dipole-like magnetic field. However, strong crustal magnetic fields were discovered over large areas of the planet's surface (*Acuña et al.*, 1998). Strong peaks (~ 100 -1500 nT at an altitude of 400 km) observed in the magnetic field data, often in association with multiple reversals of the magnetic field direction were identified as magnetic fields originating from the crust of the planet (*Acuña et al.*, 1998, 1999; *Mitchell et al.*, 2001). As the measurements of magnetic fields around the planet proceeded, global maps of the planetary magnetic fields were produced and in Figure 1.6 we show such a map from *Connerney et al.* (2005). Such magnetic anomalies could be found over much of the planet's surface, while occurring most frequently in the southern hemisphere, with highly varying field strength. The field strength from the crustal sources was also shown to be largest at southern latitudes in the longitude range $90^\circ - 270^\circ$. *Brain et al.* (2003) studied the relative contributions from the IMF and the crustal magnetic field and concluded that there is a transition altitude (about 1300-1400 km over the strongest crustal field in the southern hemisphere) at which the IMF dominates above, and the crustal field below. *Brain et al.* (2003) also stated that the Martian pressure balance altitude (solar wind pressure balances the magnetic pressure) varies with location over the planet depending on the location of the crustal fields.

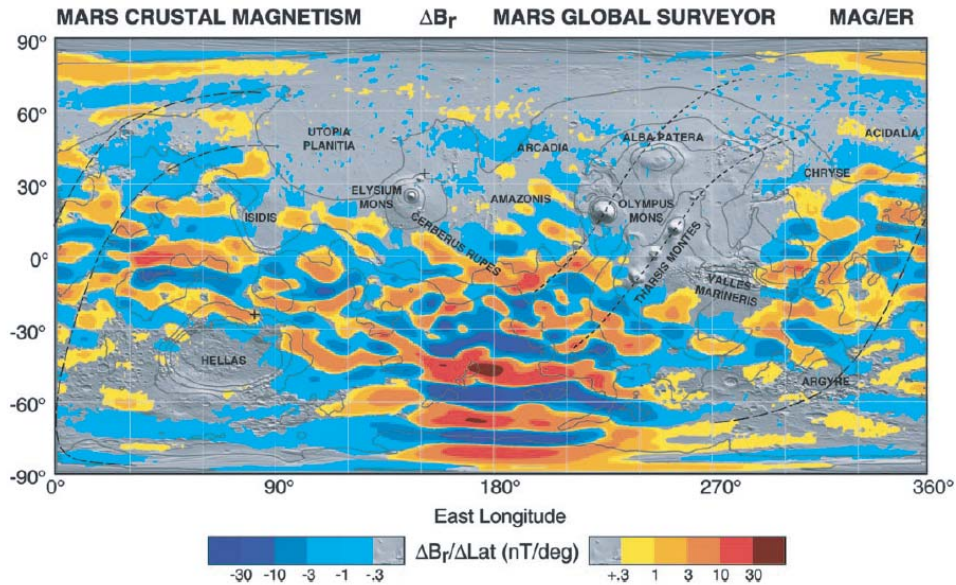


Figure 1.6: A map of the global distribution of the crustal magnetic fields of Mars. The colour shows the median radial magnetic field at 400 km from the filtered MGS measurements in each $1^\circ \times 1^\circ$ latitude/longitude bin. Reproduced from Connerney *et al.* (2005).

Subsequently, global models of the crustal magnetic fields have been produced (Purucker *et al.*, 2000; Cain *et al.*, 2003; Arkani-Hamed, 2004; Langlais *et al.*, 2004). These models are all based on the MGS measurements but use different methods. Cain *et al.* (2003) and Arkani-Hamed (2004) used spherical harmonics up to the 90th order fitted to the data to describe the crustal fields whereas Purucker *et al.* (2000) and Langlais *et al.* (2004) used binned MGS data directly. The measured MGS data which are used in each model (for either binning or for fitting to the spherical harmonic coefficients) are a combination of IMF and crustal fields which introduces an error. The IMF cannot be removed perfectly from the data. Secondly, the measurements from MGS are performed at a certain altitude and consequently the crustal field models are optimised for that altitude. Extrapolating to other altitudes

is not trivial and introduces further errors.

The crustal fields were subsequently shown to play a role in the structure of the Martian plasma environment. *Crider et al. (2002)* used MGS data to provide the first results that showed a latitude dependence of the altitude of the MPB. The altitude of the MPB was shown to be higher for crossings that occurred at high southern latitudes. In addition, within the longitude range $90^\circ - 270^\circ$ where the crustal fields are strong, the distribution of the terminator distances of the MPB was shown to be more scattered than for crossings that occurred outside this longitude range (*Crider et al., 2002*). *Mazelle et al. (2004)* used the same data set and discussed the possibility of the crustal fields also affecting the BS but could not readily show it. The effect of the crustal fields on the Martian plasma boundaries could be studied further by using a larger data set from the MGS mission and by studying the altitude of the BS as a function of the crustal field strength. This is a major part of Chapter 3 and will also be touched upon in Chapters 4 and 5.

From MEX data, it was also determined that the altitude of the MPB in terms of the altitude of magnetosheath electrons was dependent on the crustal field strength (*Fränz et al., 2006b*). In addition, *Dubinin et al. (2008b)* detected a north-south asymmetry in the BS location. The BS in the southern hemisphere was found to be located farther out than in the northern hemisphere, independent of IMF direction. The asymmetry was assumed to be caused by the crustal magnetic fields which pushed the boundary farther out in the southern hemisphere.

Simulations of the solar wind interaction with Mars that include the crustal sources do not appear to show any global changes in altitude of the BS, but on a smaller scale it can make a difference, whereas the MPB seems

to be affected more, and especially over strong crustal sources where it forms more of a magnetopause-like structure (*Harnett and Winglee, 2007*).

1.3.5 Global models of the Martian plasma environment

The global three-dimensional modelling of the Martian plasma environment has been quite extensive in the past. This has helped in understanding the solar wind interaction with Mars to a large extent. While spacecraft data give invaluable information of the plasma system, simulations of the system with global models help in testing theories of how the system is believed to function. Spacecraft data can reveal small scale (spatial or temporal) features while models tend to have much coarser spatial and temporal resolutions due to computer limitations. But models have the advantage of giving a view of the entire global picture at once, and it can also be used to study the dependence of upstream solar wind conditions in a more straightforward way, by changing the model's boundary conditions.

There are essentially two types of models being used at present. MHD models, which use the magnetohydrodynamic equations to describe the physics, treating the plasma as a fluid (*Ma et al., 2004; Terada et al., 2009*). Hybrid models, on the other hand, treating the electrons as a fluid while the ions are treated as individual, kinetic particles (*Modolo et al., 2006; Brecht and Ledvina, 2006; Harnett and Winglee, 2007; Kallio et al., 2008; Boesswetter et al., 2009*).

No model can perfectly accurately reproduce the picture of the Martian plasma environment that has risen from actual measurements. Figure 1.7 show an example of results from a simulation using the hybrid model of

Modolo et al. (2006) and Figure 1.8 shows an example of the results from a simulation using the MHD model of *Ma et al.* (2004). Both Figures show a map of the magnetic field strength around Mars, with the *Vignes et al.* (2000) models of the BS and the MPB superposed as black dashed and solid black lines. In both models the MPB and the BS are reproduced at approximately the same location as the empirical models suggest. The hybrid model takes into account kinetic effects, due to the finite ion gyro radius, which includes the asymmetry of the global environment caused by the convective electric field. The magnetic field strength is much larger in the MHD model than in the hybrid model in this case.

A recent study by *Brain et al.* (2009) shows the results of the first community-wide comparison of all the above mentioned models when using the same input conditions. The comparison shows a fairly large difference in terms of where the plasma boundaries are located even though the input conditions were the same. This reveals a weakness in the models in terms of their accuracy in describing the plasma system. The general picture was the same but large differences in details were also reported.

1.3.6 Erosion of the atmosphere

Since Mars does not have a strong global magnetic field the atmosphere is not shielded from the solar wind flow. This means that the ionosphere, consisting mainly of CO_2^+ , O^+ and O_2^+ , could continuously be eroded and swept away by the solar wind. This leads to an eventual erosion of the entire atmosphere. To what extent and through which exact processes this occurs has been studied extensively. The first measurements of plasma escape came from the Phobos 2 spacecraft where the oxygen ion escape rate was esti-

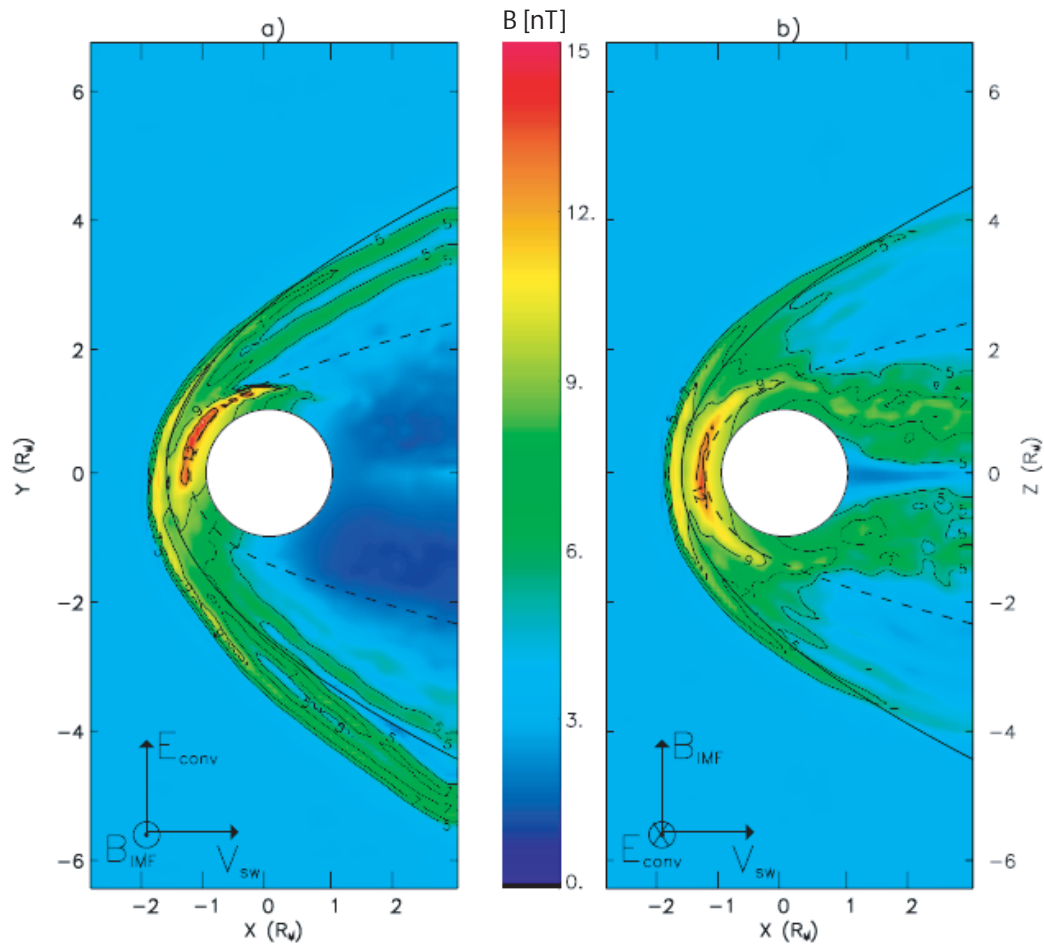


Figure 1.7: Maps of the magnetic field strength in the Martian plasma environment as results of a three-dimensional hybrid simulation. The results are shown in the (a) $x - y$ plane and (b) $x - z$ plane. The black lines show the model position of the (solid line) BS and (dashed line) MPB from Vignes *et al.* (2000). Reproduced from Modolo *et al.* (2006).

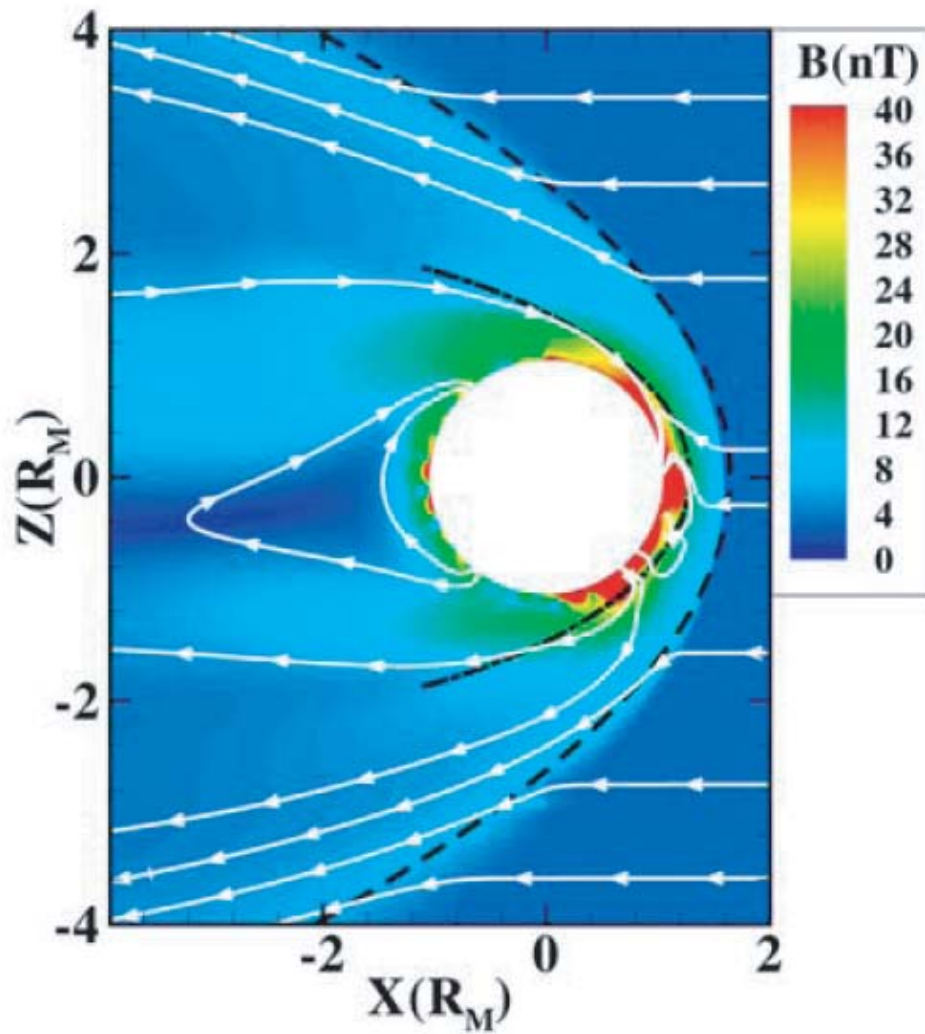


Figure 1.8: Maps of the magnetic field strength in the Martian plasma environment from a three-dimensional MHD simulation. The white lines indicate the magnetic field orientation. The dashed lines indicate the model position of the BS and MPB from Vignes *et al.* (2000). Reproduced from Ma *et al.* (2004).

mated to be on the order of $\sim 3 \cdot 10^{25} \text{ s}^{-1}$, corresponding to a loss of the present atmosphere in less than 100 million years (*Lundin et al.*, 1989). The physical process suggested for this escape to occur was ion pickup resulting from the mass-loading of the solar wind in the plasma environment, as well as ion beams from upward acceleration processes like those occurring in the Earth's auroral regions. Other possible processes that have been suggested later are thermal (Jeans) escape, sputtering, ion outflow from crustal magnetic field cusps and bulk plasma removal (e.g. detached ionospheric clouds caused by Kelvin-Helmholtz instabilities), see *Carlsson et al.* (2008) and references therein. Subsequently, more studies have been performed and after the arrival of MEX the estimated escape rates have been adjusted downward to be only on the order of $\sim 3 \cdot 10^{23} \text{ s}^{-1}$, significantly less than the first estimated values (*Barabash et al.*, 2007). Figure 1.9 shows a map from *Barabash et al.* (2007) of these integrated fluxes at Mars from MEX measurements. It was then suggested that water reservoirs, if there ever were any, could still be present on Mars or alternatively, unknown escape channels could exist. Solar forcing has been shown to increase the outflow as the observed ion escape increases during periods of high dynamic pressure and high solar EUV flux (*Lundin et al.*, 2008) and the convective electric field has been shown to govern in which hemisphere the outflow mainly takes place (*Fedorov et al.*, 2006). Sporadic outflow through ion beam events, when escaping planetary ions are observed over a short time and in a narrow angle (beamed), also predominantly occur in the hemisphere of locally upward convective electric field (*Carlsson et al.*, 2008). This can also be seen in Figure 1.9 where the ion fluxes are higher in the hemisphere of the locally upward electric field. Measurements of outflow at Mars have only been performed by MEX and

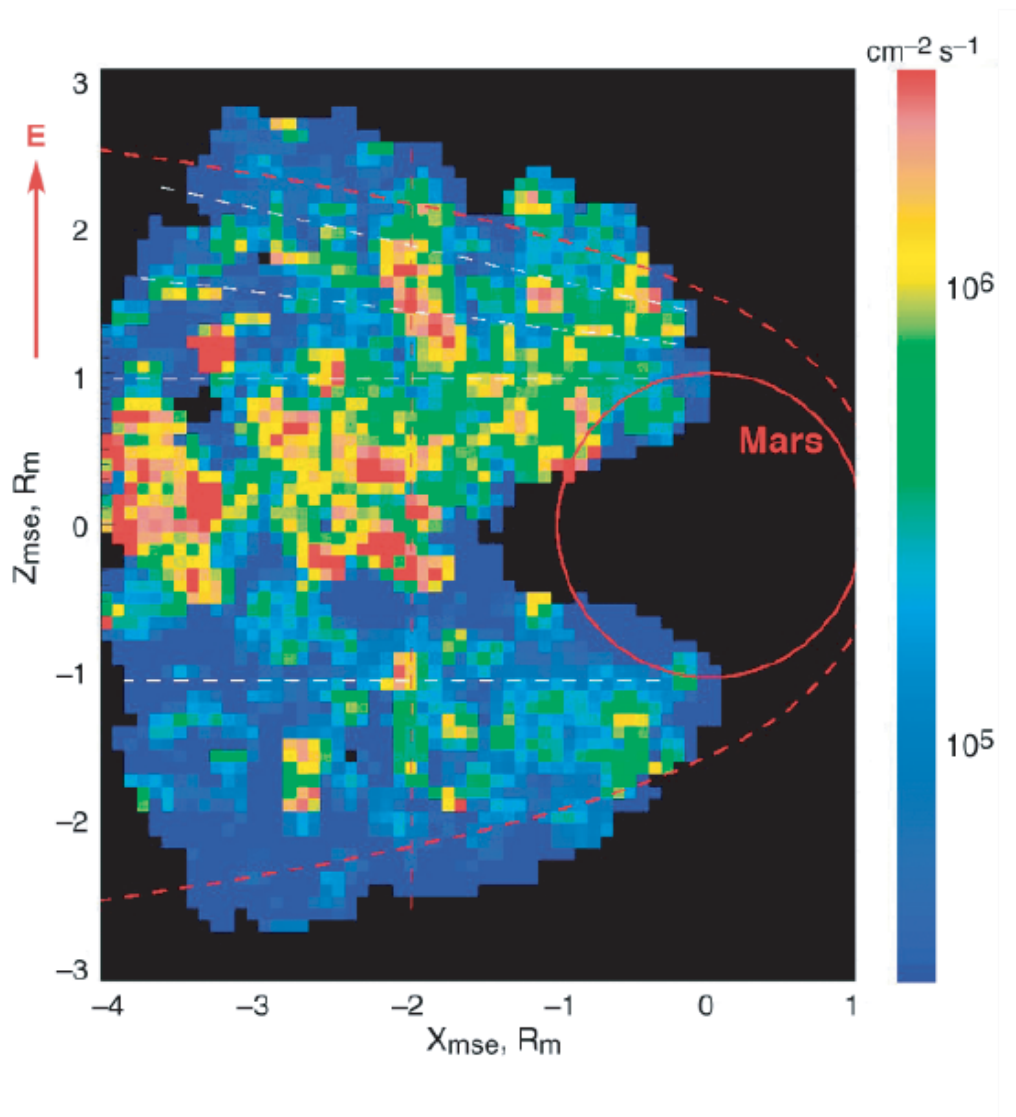


Figure 1.9: A map of the measured integrated fluxes of heavy planetary ions at Mars, averaged over $-0.8 R_M < y < 0.8 R_M$ in the $x - z$ plane in a coordinate system relative to the direction of the convective electric field. Reproduced from Barabash et al. (2007).

to some extent also by Phobos 2, but Phobos 2 did not have an adequate coverage of measurements. MEX on the other hand does not carry a magnetometer which is important for determining the direction of the outflow. It rather had to rely on magnetic field measurements from MGS during the time of mission overlap. Also, far downstream and far off the Mars-Sun line, measurements of the outflow have not been performed, which might be important for the total outflow rate. The measured outflow rates have been compared with modelled values but since the latter span an order of magnitude depending on which model is being used, this comparison does not really provide much information (*Brain et al.*, 2009). Measurements of the outflow are needed from when simultaneous magnetic field data are present. Also, estimates of the outflow rates during solar maximum are unknown and need to be determined. Neither MEX nor Phobos 2 sampled the Martian plasma environment during solar maximum. The cold ion population is not detectable by the ion mass analyzer instrument on MEX which could mean that a significant portion of the potentially escaping cold plasma is being missed.

Chapter 2

Instrumentation

In this Thesis we have used data from eight instruments onboard three spacecraft. These instruments will be described in this Chapter together with their host spacecraft and the spacecraft's orbital geometry.

2.1 Mars Global Surveyor: magnetometer and electron reflectometer

MGS arrived at Mars in September 1997 and stayed operational in orbit for 9 years, until November 2006. During the initial (pre-mapping) phase of the mission, which lasted from September 1997 until January 1999, MGS used an aerobreaking technique to slowly alter the spacecraft orbit. The orbit evolved from highly elliptical and precessing in local time to become almost circular, polar and fixed at 02h-14h local time when the 7.5 year long mapping phase began. Periapsis during the pre-mapping phase was at a minimum of ~ 100 km and apoapsis at a maximum of $\sim 17 R_M$ ($1 R_M = 3397$ km) and the nearly constant altitude during the mapping phase was ~ 400 km. The

orbital coverage during the pre-mapping phase and mapping phase is shown in Figure 2.1 in MSO coordinates.

Relevant for plasma studies, MGS carried a magnetic field investigation (MAG) (*Acuña et al.*, 1998) and an electron reflectometer (ER) (*Mitchell et al.*, 2001). The MAG instrument consisted of two fluxgate magnetometers mounted on the tips of the solar panels, about 5 m from the main spacecraft bus. It provided vector measurements of the magnetic field at a rate of 2 Hz – 16 Hz, depending on telemetry rate, in the range ± 4 nT – $\pm 65,536$ nT (*Acuña et al.*, 1998). The ER instrument measured the local electron distribution function in 30 energy levels in the range ~ 1 eV – 20 keV with a maximum time resolution of 0.5 Hz and energy resolution of 25%. The instrument had a field of view of $360^\circ \times 14^\circ$ divided on 16 sectors (*Mitchell et al.*, 2001). Plasma moments (density, velocity and temperature) can usually not be reliably calculated from the electron distribution measured by ER due to the poor energy resolution.

2.2 Mars Express: ASPERA-3 and MARSIS

MEX arrived at Mars in late 2003 and is still operational in orbit (as of 2009). It had almost three years of overlapping data coverage with MGS, until MGS died in late 2006. The orbit of MEX is highly elliptical and precessing in local time with periapsis at ~ 250 km and apoapsis at $\sim 3 R_M$. To get a rough idea of the orbital coverage during these years, the position of MEX every 3 hour is plotted in MSO coordinates in Figure 2.2.

MEX carries two instruments that have been used in this Thesis, the Analyzer of Space Plasmas and Energetic Atoms (ASPERA-3) (*Barabash*

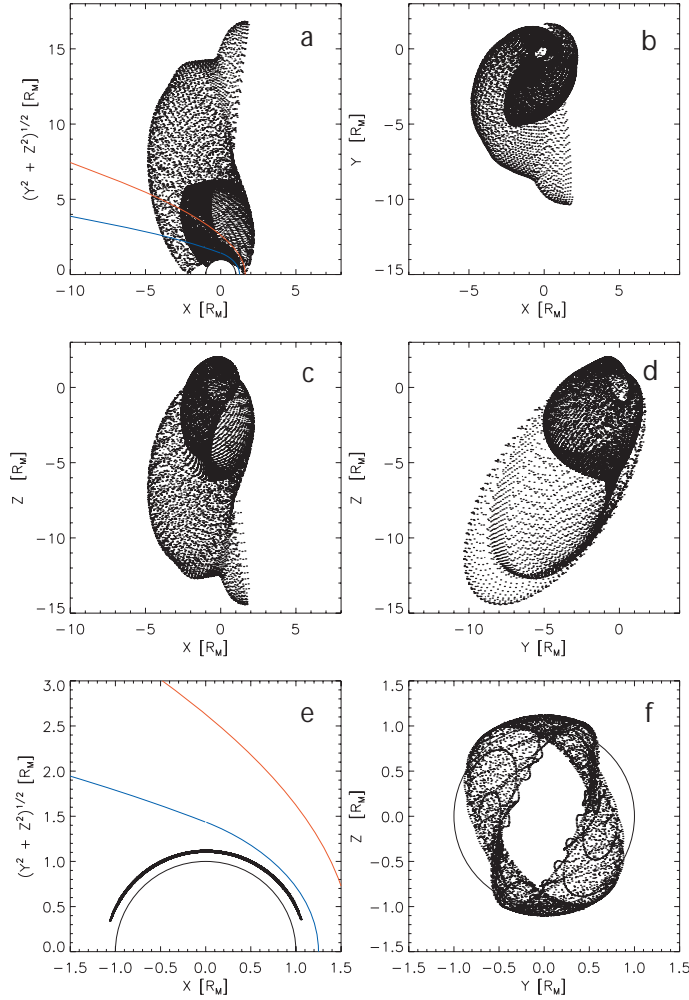


Figure 2.1: The position of MGS every 1 hour in MSO coordinates during the pre-mapping phase from September 1997 until January 1999 plotted in (a) cylindrical coordinates as well as in Cartesian coordinates projected onto the (b) $x - y$, (c) $x - z$ and (d) $y - z$ plane. The position every 4 hours during the mapping phase is plotted in (e) cylindrical coordinates and (f) projected onto the $y - z$ plane. The average BS (red line) and MPB (blue line) position from Trotignon et al. (2006) are shown in panels (a) and (e).

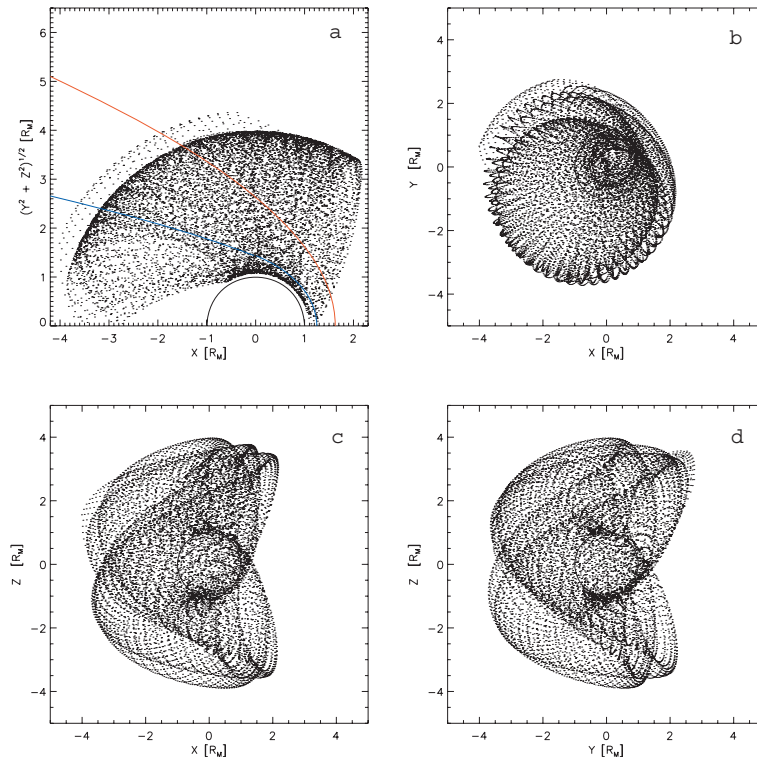


Figure 2.2: The position of MEX every 3 hours in MSO coordinates from 2004 until 2008. The position is shown in (a) cylindrical coordinates together with the average position of the BS (red line) and MPB (blue line) from Trotignon *et al.* (2006) and in Cartesian coordinates projected onto the (b) $x - y$, (c) $x - z$ and (d) $y - z$ planes.

et al., 2006) and the Mars Advanced Radar for Subsurface and Ionospheric Sounding (MARSIS) (*Gurnett et al.*, 2005). Related to space physics, MEX also performs radio occultation measurements of the ionosphere through the MaRS experiment and measures UV spectra with the SPICAM instrument, but data from these have not been included in this Thesis. ASPERA-3 includes four sensors out of which two have been used in this Thesis, the electron spectrometer (ELS) and the ion mass analyzer (IMA). ELS is similar to ER on MGS and measures the electron distribution in the energy range 10 eV – 20 keV, but with a higher energy resolution (8%) and a time resolution of 0.25 Hz. The field of view is $4^\circ \times 360^\circ$ divided into 16 sectors. IMA measures the local ion distribution function in the energy range 10 eV/q – 36 keV/q for the main ion species, H^+ , H_2^+ , He^+ and O^+ and for the molecular group of ions in the mass per charge range $20 < amu/q < 80$. It has a time resolution of 192 s and a field of view of $90^\circ \times 360^\circ$. Density, velocity and temperature moments can be calculated from both IMA and ELS, as described by *Fränzl et al.* (2006a).

MARSIS is a 40 m long dipolar antenna designed for subsurface as well as ionospheric sounding. However, it can occasionally also measure local plasma density and magnetic field magnitude, respectively, from observed harmonics of the electron plasma oscillations and electron cyclotron echoes seen in the radargrams (*Gurnett et al.*, 2005; *Duru et al.*, 2008). Since MEX does not carry a magnetometer and since ASPERA-3 cannot measure the cold plasma population very well, these extra properties of the sounder have become very valuable.

2.3 Rosetta: The Rosetta Plasma Consortium

Rosetta is not a dedicated Mars mission but merely flew past Mars on its way to a comet. The Rosetta Mars swingby took place in February 2007 with closest approach (CA) to Mars of ~ 260 km at 01:58 UT on 25 February 2007. The geometry of the swingby is shown in Figure 2.3. Rosetta approached Mars from upstream, passed by Mars on the dawn side and proceeded out through the magnetosheath in an antisunward direction. Rosetta performed measurements from about two days before CA to almost three days after, with a partial data gap between CA - 1.5 hours to CA + 1 hour because of spacecraft power reasons during the planetary eclipse. Only magnetic field measurements were made during the time of CA. All other measurements stopped before the BS was crossed inbound and started again only minutes before the outbound MPB crossing far downstream of Mars. However, measurements were conducted in the solar wind both upstream and downstream of Mars which could be used for monitoring the solar wind while MEX performed measurements of the plasma environment close to the planet.

Rosetta carries a suite of seven plasma instruments out of which four are used in this Thesis. The Langmuir probe (LAP) (*Eriksson et al., 2007*), the ion and electron sensor (IES) (*Burch et al., 2007*) and the magnetometer (MAG) (*Glassmeier et al., 2007*) are all part of the Rosetta Plasma Consortium (RPC), and are placed on the main spacecraft bus. The fourth instrument, the magnetometer (ROMAP) (*Auster et al., 2007*), is placed on the lander Philae which will ultimately touch down on the comet.

All RPC instruments increased their telemetry rates to what is known as burst mode (BM) data rate for the last four hours before the eclipse data gap as well as for the first four hours immediately following this gap, with

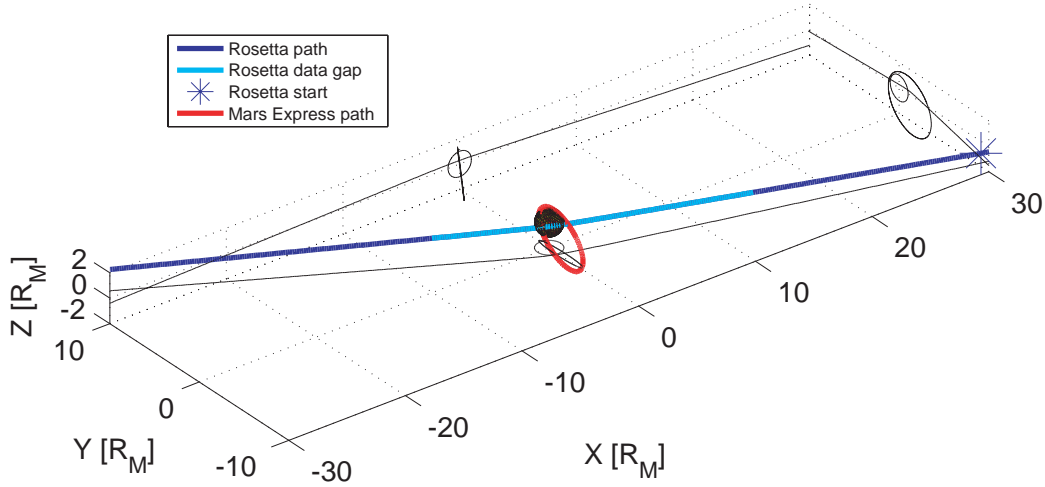


Figure 2.3: The trajectory of Rosetta and MEX from 22:38 UT on February 24, 2007, until 05:28 UT on February 25, 2007, plotted as blue and red lines in MSO coordinates. The projections of the trajectories and the planet on the $x-y$, $x-z$ and $y-z$ planes are shown as black lines. Rosetta approaches Mars from the dayside and proceeds out along the magnetic tail. The start is indicated by a blue star. The gap in the Rosetta RPC data is shown as a cyan line.

normal mode (NM) sampling at a lower rate outside this interval. The LAP instrument operated in bias current mode during the swingby, measuring the probe-to-spacecraft potential V_{ps} at 57.8 Hz in BM and 0.9 Hz in NM. LAP consists of two probes, of which only probe 1, mounted on the slightly longer boom, has been used in this Thesis, as probe 2 was mostly in eclipse and could therefore not be used for V_{ps} measurements. MAG sampled the three-axis magnetic field at 20 Hz in BM and 1 Hz in NM. RPC-MAG data are more reliable than ROMAP data when other instruments are in operation since the MAG sensor is placed on a boom and thus farther away from the spacecraft body. During CA all other instruments were switched off and the ROMAP data were not disturbed. Magnetic field data from ROMAP thus exist for the entire Mars flyby, at a sampling rate of 32 Hz around

CA and then at a sampling rate of 1 Hz a few hours before and after the CA interval time. IES recorded electron and ion energy spectra with a time resolution of 128 s in BM. The combined (ion and electron) IES telemetry rate is 253 bps in BM and 50 bps in NM. Due to field of view limitations (2π steradians around the instrument equator) combined with having the instrument behind the spacecraft as seen from the Sun, the full solar wind ion flow was not accessible to IES, meaning that a useful plasma density estimate cannot be readily produced from the IES ion data. However, the energy information in IES data can be directly interpreted, and can be used to show the presence and speed of the solar wind even though only a part of the flow can be detected.

2.4 Moments from ion and electron measurements

The spectra measured by electron and ion instruments give useful information about the plasma but of further interest are the values of the density, velocity and temperature of the plasma. These quantities can be derived from the spectrograms and in this Section we will briefly describe how.

The particle instruments used in this Thesis measure single electrons and ions at a certain energy E (and sometimes masses for the ions), over a certain solid angle Ω , at a certain position \mathbf{r} and at a time t , which is a quantity called differential flux $J(E, \Omega, \mathbf{r}, t)$. The relation between the differential flux and the local phase-space distribution function $f(\mathbf{r}, \mathbf{v}, t)$ is

$$J(E, \Omega, \mathbf{r}, t) = \frac{v^2}{m} f(\mathbf{r}, \mathbf{v}, t), \quad (2.1)$$

where m is the mass and v is the velocity. The density n , bulk velocity vector \mathbf{V} and pressure tensor \mathbf{P} moments can be calculated from the distribution function as

$$n(\mathbf{r}, t) = \int_{\mathbf{v}} f(\mathbf{r}, \mathbf{v}, t) d^3\mathbf{v}, \quad (2.2)$$

$$n(\mathbf{r}, t)\mathbf{V}(\mathbf{r}, t) = \int_{\mathbf{v}} \mathbf{v} f(\mathbf{r}, \mathbf{v}, t) d^3\mathbf{v}, \quad (2.3)$$

and

$$\mathbf{P}(\mathbf{r}, t) = \int_{\mathbf{v}} m\mathbf{v}\mathbf{v} f(\mathbf{r}, \mathbf{v}, t) d^3\mathbf{v}. \quad (2.4)$$

The temperature can then be calculated as $\mathbf{T} = \mathbf{P}/nk$, where k is Boltzmann's constant.

Another way of obtaining the plasma moments is to assume that the phase-space density of the particles has a Maxwellian distribution in velocity space. Then the density and thermal energy can in principle be obtained by fitting a Maxwellian curve to the measured spectra. A more thorough description of how the moments are calculated from the ELS and IMA can be found in *Fränzl et al.* (2006a). The spacecraft potential, which mostly affects low-energy electrons, and the geometric factor (sensitivity of the detector surface multiplied by solid angle) also needs to be taken into account to produce accurate moments.

2.5 Rosetta and Mars Express density cross-calibration

The Rosetta LAP instrument measured probe-to-spacecraft potential V_{ps} during the Mars flyby. This is assumed to be related to plasma density which is of further interest in Chapter 4 of this Thesis, and we have undertaken a first basic calibration of the Langmuir probe density estimates using density measurements from MEX ELS. The material presented in this Section is published in *Edberg et al. (2009c)*.

To calibrate the measurements of V_{ps} by Rosetta LAP to MEX ELS plasma density moments, we need reliable comparison data. Figure 2.4 shows MEX ELS electron density moment and Rosetta LAP V_{ps} data in the solar wind for the days following the Rosetta flyby. During this period, Rosetta was in the solar wind downstream of Mars and MEX, so that similar solar wind conditions can be reasonably assumed, at least on a statistical basis. To produce directly comparable datasets, the ELS data have been time shifted to the time line of Rosetta by adding a solar wind propagation time based on the difference in the MSO x -coordinate between the two spacecraft and the solar wind velocity derived from the energy at the peak in the IMA spectra. For most of this period, the attitude of Rosetta was stable, except for one change of about 40° of the solar aspect angle (SAA), i.e. the angle between the spacecraft z -axis and the direction to the Sun. This corresponds to a rotation about the y -axis which is parallel to the solar panels. The SAA was however never more than 50° from its value during the period of main scientific interest, i.e. around the time of CA, which is necessary for a reliable calibration. For this reason, we do not include data from the days preceding

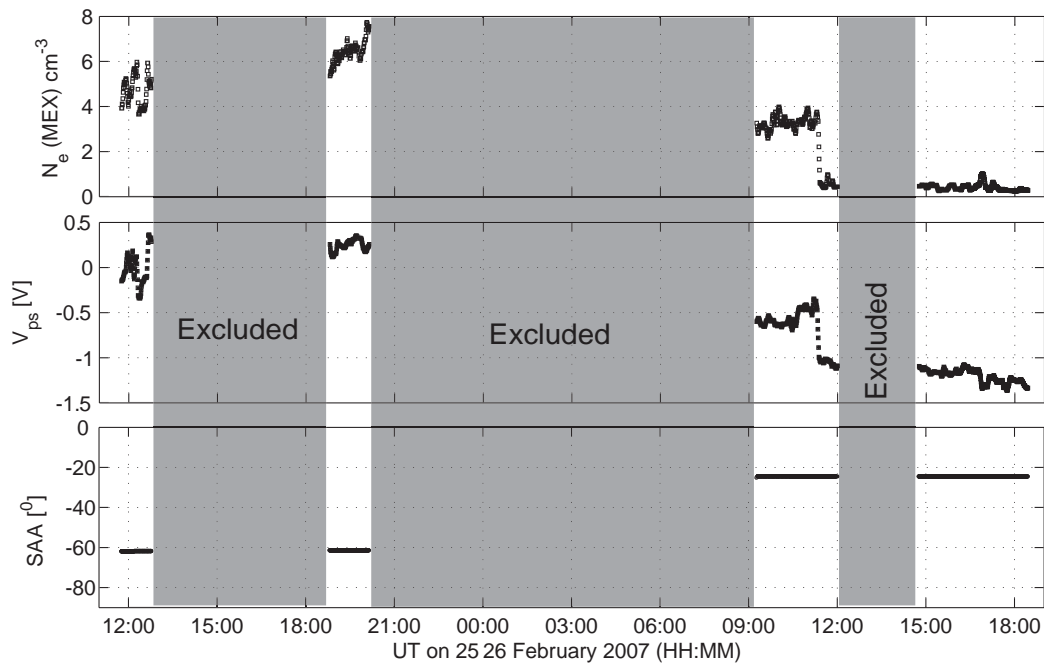


Figure 2.4: Time series of data used for the density inter-calibration between Rosetta and MEX in Figure 2.5. The top panel shows the electron density N_e measured by the ELS instrument on board MEX, time shifted to Rosetta's time line as explained in the text. The middle panel shows V_{ps} measured by the LAP instrument on board Rosetta and the lower panel shows the SAA of Rosetta. The grey areas indicate when data have been excluded from the inter-calibration as explained in the text.

the Rosetta flyby in the calibration since the SAA was very different then. The solar wind does not show any significant variability during the days before the flyby either, which is necessary for this type of calibration. Small structures in the solar wind are not easily observed at two very distant (up to $300 R_M$ in this case) positions in space and would only bias the calibration by adding a lot of data points around one specific value. We point out that this will be an approximate calibration but still reasonably good.

Periods during which the Rosetta attitude is changing rapidly, and where there are data gaps in the MEX data or when MEX is not in the solar wind, have also been excluded from the data sets, and are shaded in Figure 2.4. While some details differ, as expected in the dynamic solar wind, it is clear that the main features in the two data sets are the same, including a significant decrease in plasma density before noon on February 26 as well as the general trends in the data.

The measurements are combined in Figure 2.5, where the time-shifted electron density N_e from the ELS instrument is plotted versus V_{ps} as measured by Rosetta, down sampled (using linear interpolation) to the ELS time resolution of 4 s. The data points are separated into stars and plus-signs which correspond to different SAAs of Rosetta. We also show three lines resulting from linear fits to, first, the data points where the SAA had a constant value of -25° (dotted line) and secondly to the data points where the SAA had a constant value of -62° (dashed line). Since the two fits for different SAAs are reasonably close to each other, we feel confident about merging the data points and perform a calibration from the full data set in this time interval. This is shown as the solid line, given by the relation $N_e[cm^{-3}] = 3.98V_{ps}[V] + 5.22$. The coefficient of determination for this curve

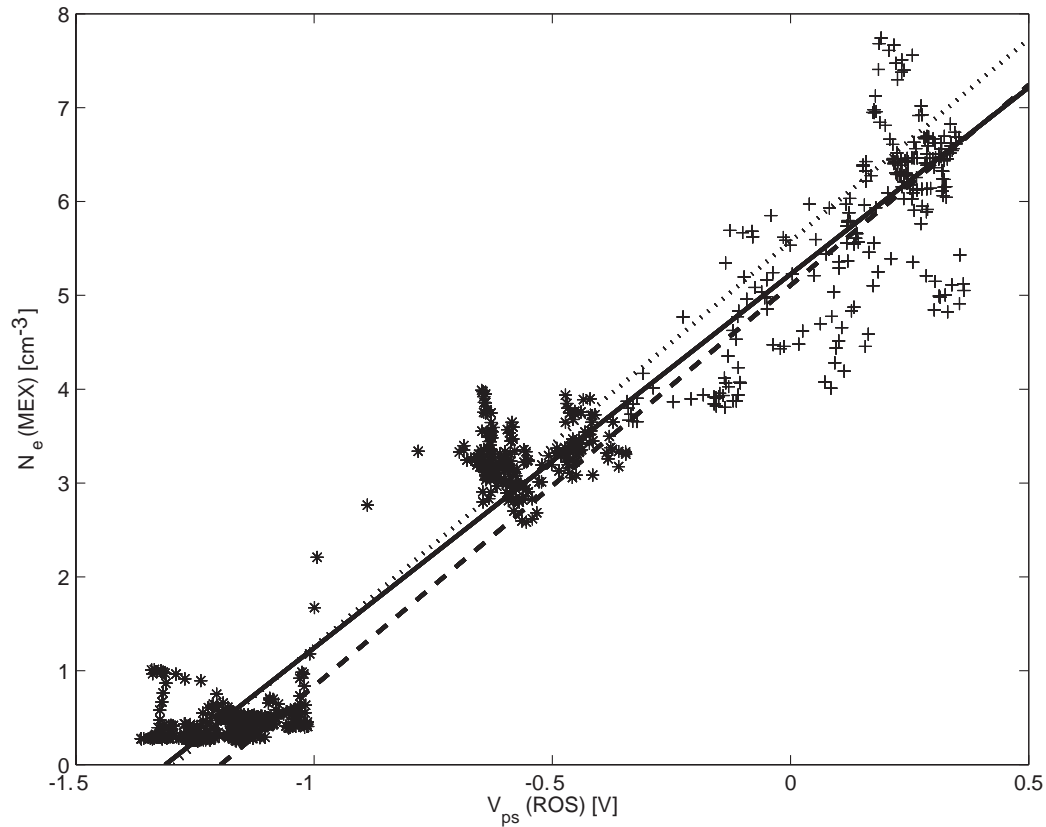


Figure 2.5: The electron density N_e measured by the ELS instrument on MEX plotted versus probe-to-spacecraft potential V_{ps} measured by the LAP instrument on Rosetta. Stars and plus-signs denote different SAAs of Rosetta (-25° and -62° , respectively). The data were taken from intervals as described in Figure 2.4. The solid line is a fitted curve to all of the data whereas the dotted and dashed lines are a fits to the data obtained when the SAA of Rosetta was -25° and -62° , respectively. The linear relation of the solid curve between V_{ps} and N_e ($N_e[cm^{-3}] = 3.98V_{ps}[V] + 5.22$) is used to estimate the density from LAP V_{ps} measurements.

is 0.95.

While the linear fit to the data points is quite good, with an inevitable spread caused by the dynamic and inhomogeneous nature of the solar wind, the spacecraft potential is usually expected to be a logarithmic function of the plasma density, as the photoelectrons emitted are usually assumed to have an exponential distribution with energy. This is indeed close to what is observed on Earth-orbiting satellites equipped with long wire booms extending far from the perturbations caused by the spacecraft body (*Thiebault et al.*, 2006; *Pedersen et al.*, 2008). However, for the short booms of Rosetta (2.24 m and 1.62 m), we can expect to see only a fraction of the spacecraft potential. To this fraction should be added important contributions from the potential fields generated by the solar panels and also the potential drop over the probe sheath: the latter is on the order of a volt, which clearly is of the same order as the measured V_{ps} . Hence, we cannot expect to find a logarithmic relation, valid for a large range of potentials. The observed good linear correlation in Figure 2.5 should therefore not be extrapolated far outside the given interval, and should be interpreted rather as a linear expansion of a full N_e - V_{ps} relation in the interval shown. As the details of this relation also depend on, for example, the UV intensity (*Pedersen et al.*, 2008; *Eriksson and Winkler*, 2008), the validity outside the flyby interval is further reduced. Nevertheless, the statistical correlation seen in Figure 2.5 as well as the obvious co-variation in Figure 2.4 shows that the linear calibration can be used for the data we are interested in, accurate to a factor of about 2 for V_{ps} in the range -0.7 V to +0.5 V, assuming that the density from MEX is correct. We do not say that this is the final calibration that will be used when Rosetta reaches the comet but simply that it gives a rough estimate of the density for now.

Chapter 3

Mars Global Surveyor measurements of the influence of the crustal magnetic fields

In this Chapter we examine the shape and location of the BS and MPB using the data set from the MGS spacecraft. We also study the influence of the crustal magnetic fields on these two boundaries as well as study the magnetic field strength inside the MPB. Some of the material presented in this chapter is published in *Edberg et al. (2008)*.

3.1 Introduction

Mars has been considered to be a mainly unmagnetized body in the past and the solar wind interaction with Mars have therefore been expected to be very similar to that of Venus and comets. However, the discovery of strong crustal magnetic fields on localized places on Mars, by the MGS spacecraft, have somewhat changed this view. As MGS orbited Mars during the first 1.5

years after arrival in late 1997 it repeatedly crossed the BS and the MPB in the Martian plasma environment. This large data set of crossings can be used to produce statistical best-fit models of the boundaries as well as to study the variation of the boundaries with the crustal magnetic fields. The boundary shapes have already been studied in the past but with smaller subsets of the data and the influence of the crustal magnetic fields have only been touched upon briefly. In this Chapter we will complement the previous studies by using the full data set and study the influence of the crustal magnetic fields in more detail. We start off by introducing one example of boundary crossings in the MGS MAG/ER data set. We then use all similarly observed boundary crossings in order to model the shape of the boundaries and to determine the influence of the crustal magnetic fields.

3.2 Data analysis

Figure 3.1 shows an example of a time series from MGS. The orbit at this time was highly elliptical, nearly polar and close to the terminator plane. The top two panels show the magnetic field measurements from the MAG instrument. The following panel shows differential energy flux from the ER instrument. The bottom two panels show SZA of the spacecraft and altitude above the surface of Mars. The inbound BS crossing is identified in the MAG/ER data as an increase in magnetic field fluctuations together with an increase in electron fluxes at around 02:10 UT. The spacecraft then entered the magnetosheath, characterized by heated plasma and more turbulent magnetic field. The crossing of the MPB is identified by three simultaneous features in the data at 03:22 UT. The most obvious signature is a fairly sudden increase in

the magnitude of the magnetic field. In addition, the strong fluctuations in the magnetic field which occur in the magnetosheath inside the BS stop at this boundary and thirdly, the electron flux decreases compared to values in the magnetosheath. A fourth signature can sometimes also be seen, which is the beginning of the draping (rotation of the field direction) of the field lines around the planet. After the inbound MPB crossing MGS is inside the MPR until 03:48 UT followed by a period close to crustal magnetic field sources. The MPR is entered again at 04:02 UT, the outbound MPB crossing occurs at around 04:09 UT and the outbound BS crossing at 04:35 UT. We have examined the entire MAG and ER data set from the pre-mapping phase of the mission in search of such crossings of the MPB and BS. We found a total of 993 and 619 crossings, respectively. The reason for the fewer BS crossings is that the MAG and ER instruments only operated around CA after the first 12 months, such that the MPB could be observed, but not the BS which was too far out. The number of crossings found in this study differs from that by *Trotignon et al.* (2006) (573 BS crossings and 860 MPB crossings) and *Bertucci et al.* (2005) (1149 MPB crossings), who also used the entire data set. This is explained by the fact that the boundaries can be difficult to determine in some cases, e.g. when the orbit is tangential to the boundary surface or when the crossings occur close to strong crustal anomalies. Some crossings might be included in some studies and ruled out as too uncertain in others. Unusual solar wind conditions can also disturb the appearance of the boundaries, thus making them hard to identify.

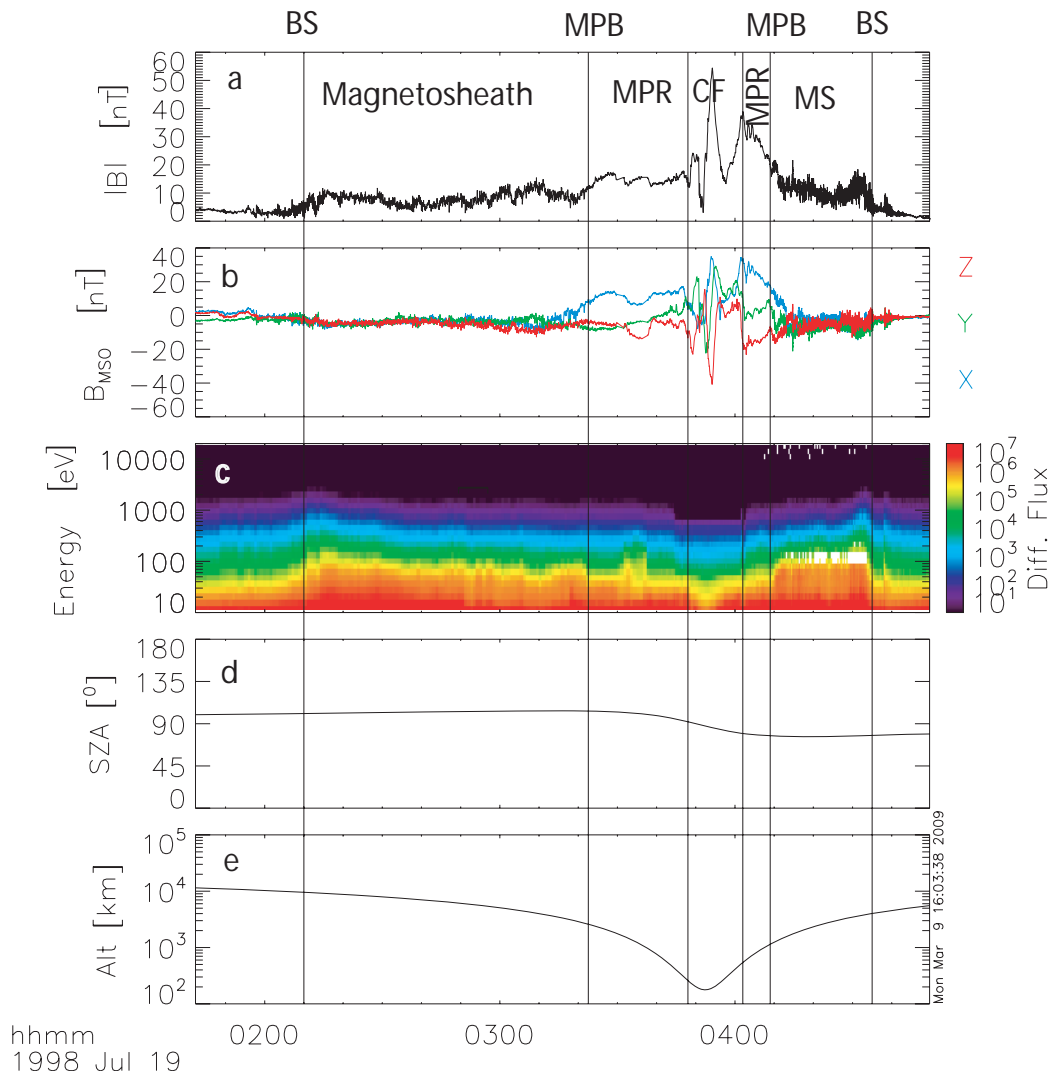


Figure 3.1: A time series of MGS MAG and ER data. The panels show (a) magnetic field strength, (b) magnetic field components in MSO, (c) differential energy flux in units of $cm^{-2}s^{-1}sr^{-1}eV^{-1}$, (d) SZA of MGS and (e) altitude above the surface of Mars. The location of the MPB, BS and the inner edge of the MPR are indicated by vertical black lines.

Table 3.1: Best fit conic section parameters of the MPB obtained in this study, with and without a fixed subsolar standoff distance, as well as for the studies by Vignes *et al.* (2000) and Trotignon *et al.* (2006). The uncertainties are calculated differently here (see text for explanation), which explains the large difference in uncertainty values compared with the studies by Vignes *et al.* (2000) and Trotignon *et al.* (2006). N is the number of data points. See Section 1.3.2 for explanations of X_0 , ϵ and L .

Study by	X_0 [R_M]	ϵ	L [R_M]	R_{SS} [R_M]	N
This study	0.86 ± 0.11	0.92 ± 0.03	0.90 ± 0.06	1.33 ± 0.15	993
This study, fixed R_{SS}	0.73 ± 0.11	0.90 ± 0.03	0.98 ± 0.06	1.25	993
Vignes <i>et al.</i> (2000)	0.78 ± 0.01	0.90 ± 0.01	0.96 ± 0.01	1.29 ± 0.04	488
Trotignon <i>et al.</i> (2006) ($x > 0$)	0.64 ± 0.01	0.77 ± 0.01	1.08 ± 0.03	1.25 ± 0.03	901
Trotignon <i>et al.</i> (2006) ($x < 0$)	1.60	1.009 ± 0.003	0.528 ± 0.012		901

3.2.1 Shape of bow shock and magnetic pileup boundary

In the upper two panels of Figure 3.2 all observed crossings of the BS and MPB are plotted in a cylindrical coordinate system. The horizontal axis is the aberrated MSO x -axis, while the vertical axis is the perpendicular distance from the x -axis = $\sqrt{y^2 + z^2}$. The variability of the crossing position is large, and larger on the night side than on the day side. In order to determine the best fit shape of the BS and MPB we use in principal the same method as Vignes *et al.* (2000) and fit a conic section to the data points, with the difference that we use the entire data set and not just the first year of data as used in Vignes *et al.* (2000). This is done for both the MPB and for the BS. In the lower panels (c and d) of Figure 3.2 are shown the best fit conic sections determined here (solid line) together with the fits obtained by Vignes *et al.* (2000) (dashed line) and Trotignon *et al.* (2006) (dashed-dotted line). The dotted line in panel (d) shows a constrained fit to be described in more detail later in this subsection. The parameters of the fits are shown in Table 3.1 for the MPB and in Table 3.2 for the BS.

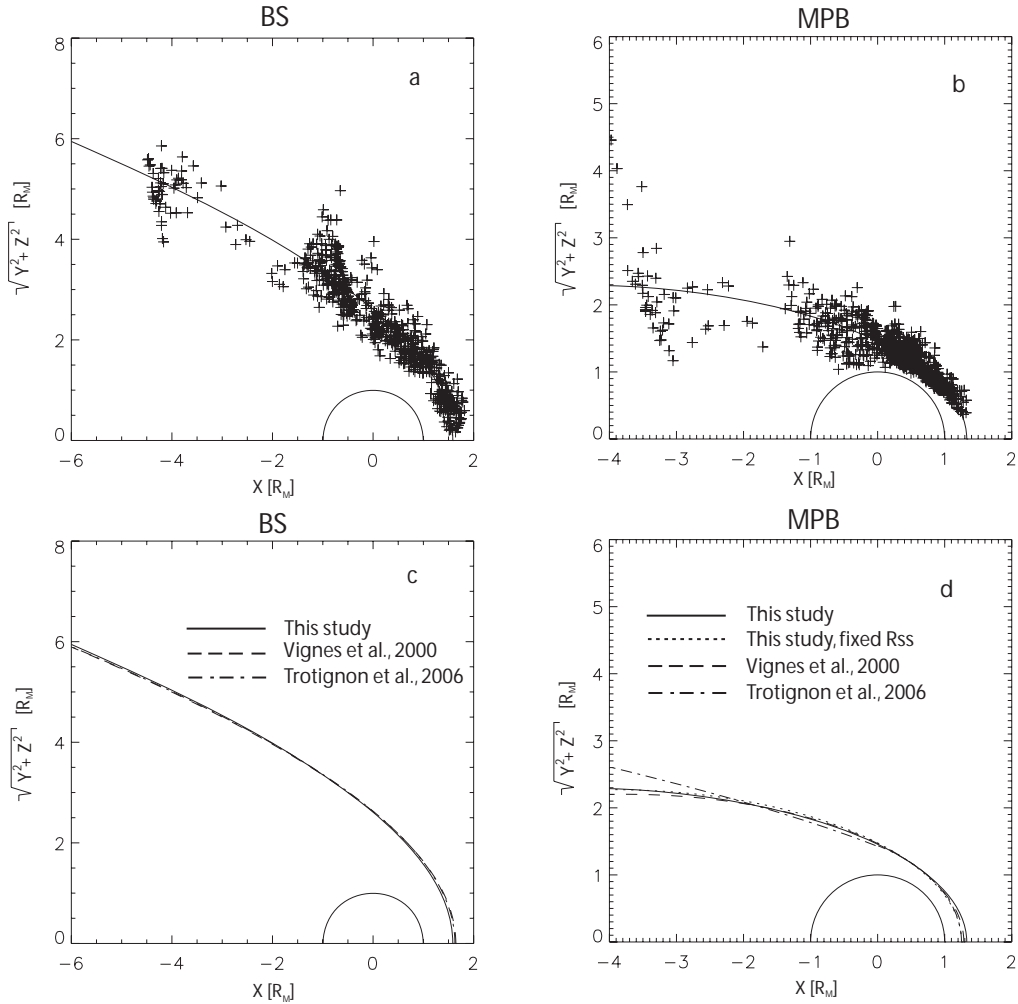


Figure 3.2: All (a) BS and (b) MPB crossings found from the pre-mapping phase of the MGS mission plotted in aberrated cylindrical MSO coordinates together with fits of conic sections from this study (solid line). The bottom panels show a comparison of fits between this study (solid line), the best fit from Vignes *et al.* (2000) (dashed line) and the best fit from Trotignon *et al.* (2006) (dashed-dotted) for the (c) BS and (d) MPB crossings. For the MPB is also shown the best fit from this study with a fixed sub-solar point value of $1.25 R_M$ (dotted line), see text for further explanations.

Table 3.2: Best fit conic section parameters for the BS obtained in this study, as well as in the studies by *Vignes et al. (2000)* and *Trotignon et al. (2006)*. N is the number of BS crossings.

Study by	X_0 [R_M]	ϵ	L [R_M]	R_{SS} [R_M]	N
This study	0.55 ± 0.12	1.05 ± 0.04	2.10 ± 0.09	1.58 ± 0.18	619
<i>Vignes et al. (2000)</i>	0.64 ± 0.02	1.03 ± 0.01	2.04 ± 0.02	1.64 ± 0.08	450
<i>Trotignon et al. (2006)</i>	0.6	1.026 ± 0.002	2.081 ± 0.006	1.63 ± 0.01	700

A difference that is introduced here compared to *Vignes et al. (2000)* is that we define the outer surface of the MPB and BS to be the actual position of the boundary crossing. This makes it necessary to calculate the uncertainty of the fit in a different way. *Vignes et al. (2000)* repeated the fitting method a great number of times, and because different random locations within the boundary were used for the position of each crossing each time, an uncertainty could be estimated. In this study, we calculate the uncertainty by varying the fit parameters individually from the best fit value, until the root mean square deviation of the data points changed by 5%. The uncertainty is then chosen as the difference between the best fit parameter value and the value that makes the RMS deviation change by 5%. The uncertainty estimates obtained in this way are larger than those obtained by *Vignes et al. (2000)*, but since they are calculated differently they cannot be easily compared with each other.

From Figure 3.2, panel (d), it can be seen that the best fit to the MPB data from this study agrees well with the previous study by *Vignes et al. (2000)*, who only used a subset of the data. However, there are some differences. The subsolar standoff distance, calculated as

$$R_{SS} = X_0 + \frac{L}{1 + \epsilon}, \quad (3.1)$$

is found to be $0.04 R_M$ larger than in the study by *Vignes et al.* (2000) ($1.33 R_M$ compared with $1.29 R_M$). The tail radius at $X = -4 R_M$ is found to be $0.10 R_M$ larger than in the study by *Vignes et al.* (2000) ($2.30 R_M$ compared with $2.20 R_M$). Here we use almost twice as many data points in our fit, so that the average boundary location should be determined with more accuracy. However, the larger standoff distance could also be explained by the fact that we have used the outer surface of the boundary as the position of the crossings. On the other hand, the tail radius should in that case also be larger rather than smaller. The smaller tail radius could be explained by the fact that MPB crossings far downstream are much harder to identify, and the uncertainty in their location then becomes larger.

It is worth noting that the fitted MPB curve has its closest point to the planet not directly upstream of the planet but at a SZA of about 45° from the x -axis. This is due to the fact that the data coverage is poor close to the planet below a SZA of $\sim 40^\circ$ (*Brain et al.*, 2003), and there are no crossings observed below a SZA of about 20° . Hence, the fit is not well represented at low SZAs, such that the subsolar standoff distance may not be realistic. This feature also occurred in the studies by *Vignes et al.* (2000) and *Trotignon et al.* (2006). In order to account for this we introduce a new criterion in the fitting routine, which fixes the subsolar distance of the conic section to $1.25 R_M$. This value is taken from the closest distance of the initial fit to the MPB surface (at a SZA of 45°), and it is also the subsolar standoff distance from the fit by *Trotignon et al.* (2006). We therefore assume that this is a reasonable value based on present evidence. The fitting is then done in the same way as before. The new fit is shown in panel (d) of Figure 3.2 by the dotted line. This fit is more realistic in the sense that the smallest

radial distance is at the subsolar point while the tail radius does not deviate significantly from the previous fit.

The best fit to the BS crossings, shown in Figure 3.2 panel (c), is in good agreement with the previous studies by *Vignes et al.* (2000) and *Trotignon et al.* (2006). However, the average standoff distance is found to be $0.06 R_M$ smaller compared with the standoff distance from *Vignes et al.* (2000) ($1.58 R_M$ compared with $1.64 R_M$), and the tail radius to be $0.05 R_M$ larger at $X = -6 R_M$ ($5.90 R_M$ compared with $5.85 R_M$). Again, we use more data points and should have better accuracy.

3.2.2 The influence of crustal magnetic fields

The observed scatter in the position of the MPB and BS in Figure 3.2 is extensive and there are a number of factors controlling it. Solar wind parameters and the IMF direction are included in these factors. However, here we investigate the influence of the crustal magnetic fields on the location of both the MPB and BS, as seen by the MGS measurements.

We use the extrapolated terminator distances to examine the dependence of the location of the crossings on the crustal magnetic fields of Mars. The extrapolated crossings of the MPB were first divided into three regions depending on the planetocentric longitude at which they were observed: $0^\circ - 120^\circ$, $120^\circ - 240^\circ$ or $240^\circ - 360^\circ$. The crossings within each longitude range are then divided into whether they were observed over strong crustal fields or weak crustal fields by comparing the location of the crossings with a map of the crustal magnetic fields, such as that of *Connerney et al.* (2005) in Figure 1.6. Roughly, in the longitude range $0^\circ - 120^\circ$ the crustal fields are strongest in the latitude range -45° to 45° , in the longitude range $120^\circ - 240^\circ$ they

Table 3.3: Average extrapolated MPB terminator distances and standard deviations in units of R_M divided into three longitude ranges and subdivided into whether they are observed over weak or strong crustal fields, as described in the text.

	Longitude range		
	0° – 120°	120° – 240°	240° – 360°
Strong crustal fields	1.48±0.18	1.55±0.24	1.48±0.18
Weak crustal fields	1.38±0.12	1.43±0.15	1.41±0.12

are strongest in the latitude range -90° to 0° and in the longitude range $240^\circ - 360^\circ$ they are again strongest in the latitude range -45° to 45° .

In Figure 3.3 the extrapolated terminator distance is plotted as a function of Martian longitude. The mean terminator distance is shown in each of the three longitude sections for crossings that occurred over strong crustal fields (solid lines) and for crossings that were observed over weak crustal fields (dashed lines), based on the latitude and longitude limits given above. The figure shows that the MPB is on average located farther out when there are strong crustal sources underneath. The scatter of the terminator distances is again extensive. However, the differences in the averages for crossings observed above strong and weak crustal fields are statistically significant in each of the three longitude sections, according to a Student's t-test at a 95% confidence level. The average altitudes and corresponding standard deviations for the MPB crossings are shown in Table 3.3. Our results are in agreement with the results obtained by *Crider et al.* (2002) who showed that the MPB was located farther out for high southern latitudes. The study reported here shows that it is not only in the southern hemisphere where the MPB altitude is raised by the crustal sources, but rather that the boundary is affected more locally and appears to be pushed outward to higher altitudes

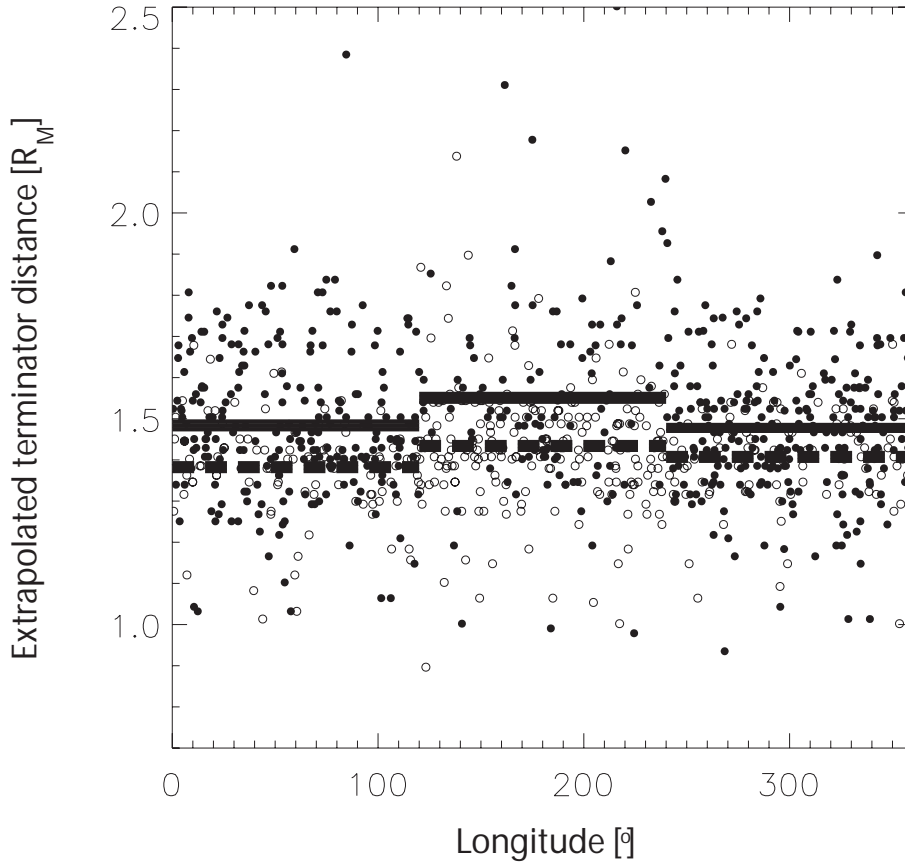


Figure 3.3: The extrapolated terminator distance of all MPB crossings plotted versus planetary longitude. Crossings over all SZAs are included. The filled circles indicate crossings over strong crustal fields while open circles indicate crossings over weak crustal fields. The solid and dashed lines indicate the average distances over regions with strong and weak crustal fields, respectively. The regions of strong crustal fields were chosen as: longitude $0^\circ - 120^\circ$, latitude $-45^\circ - 45^\circ$; longitude $120^\circ - 240^\circ$, latitude $-90^\circ - 0^\circ$; and longitude $240^\circ - 360^\circ$, latitude $-45^\circ - 45^\circ$.

over the specific regions where the crustal sources are locally stronger. *Brain et al.* (2005) also confirmed that the MPB is located at higher altitudes over crustal fields by using electron data from the 400 km altitude mapping orbit and identified time periods when MGS was in or below the sheath region. Since the altitude of the spacecraft was more or less constant, detection of sheath electrons implies that the MPB was pushed downward and this was observed more frequently over regions without strong crustal sources.

The crustal magnetic fields are rotating with the planet and thus introduce a time varying parameter that influences the MPB. If all other factors that influence the position of the MPB stay constant, the boundary would move up and down as the planet rotates. The additional magnetic pressure from the crustal sources pushes the boundary farther out. This cannot be distinguished from only one orbit, since there are many factors involved, but on average it can be detected since the other factors, such as solar wind conditions, average out in the statistics. The existence of mini-magnetospheres has been suggested by *Acuña et al.* (1998) and *Mitchell et al.* (2001), and appear to be likely features of the Martian plasma environment.

In Figure 3.4 we show evidence that the crustal fields also affect the Martian BS. The extrapolated BS terminator distance is again plotted as a function of longitude. Only BS crossings that are observed on the dayside of Mars are included now because there are essentially no nightside BS crossings in the northern hemisphere and we want an even spatial distribution of BS crossings in the northern and southern hemisphere. The average distance over the southern and northern hemisphere of Mars is shown in three longitude ranges. The average distances of the BS crossings observed over the southern hemisphere in the same three longitudinal sections (the solid

Table 3.4: Average extrapolated BS terminator distances and standard deviations in units of R_M divided into three longitude ranges and subdivided into southern and northern hemisphere.

	Longitude range		
	$0^\circ - 120^\circ$	$120^\circ - 240^\circ$	$240^\circ - 360^\circ$
Southern hemisphere	2.71 ± 0.27	2.76 ± 0.24	2.68 ± 0.27
Northern hemisphere	2.27 ± 0.18	2.28 ± 0.17	2.29 ± 0.17

lines in Figure 3.4) are clearly located farther out than the crossings that occur over the northern hemisphere (the dashed lines). We point out again that the strongest crustal fields are observed in the southern hemisphere. The values of the average altitudes and standard deviations are shown in Table 3.4. This result is more surprising since the strength of the crustal fields decreases rapidly with altitude and hence would be expected to have a smaller effect on the location of the BS. The influence of the crustal fields does, however, appear to be significant. This result does contradict the results of *Vignes et al.* (2002) who claimed that the crustal fields did not have any significant effect on the location of the BS. However, *Vignes et al.* (2002) did not separate crossings into whether they were observed over southern or northern latitudes but simply took the average altitude in longitude bins of 20° each, independent of latitude. *Mazelle et al.* (2004) did find a small, but not insignificant, asymmetry in BS distance between ecliptic north and south and claimed that it was larger downstream of the planet. In our study, where we look at dayside BS crossings only, the BS does not appear to have a significant maximum for the longitude range $120^\circ - 240^\circ$ where the crustal fields are strongest. Instead, the BS in the entire southern hemisphere appears to be affected globally and pushed outwards by the strongest crustal fields.

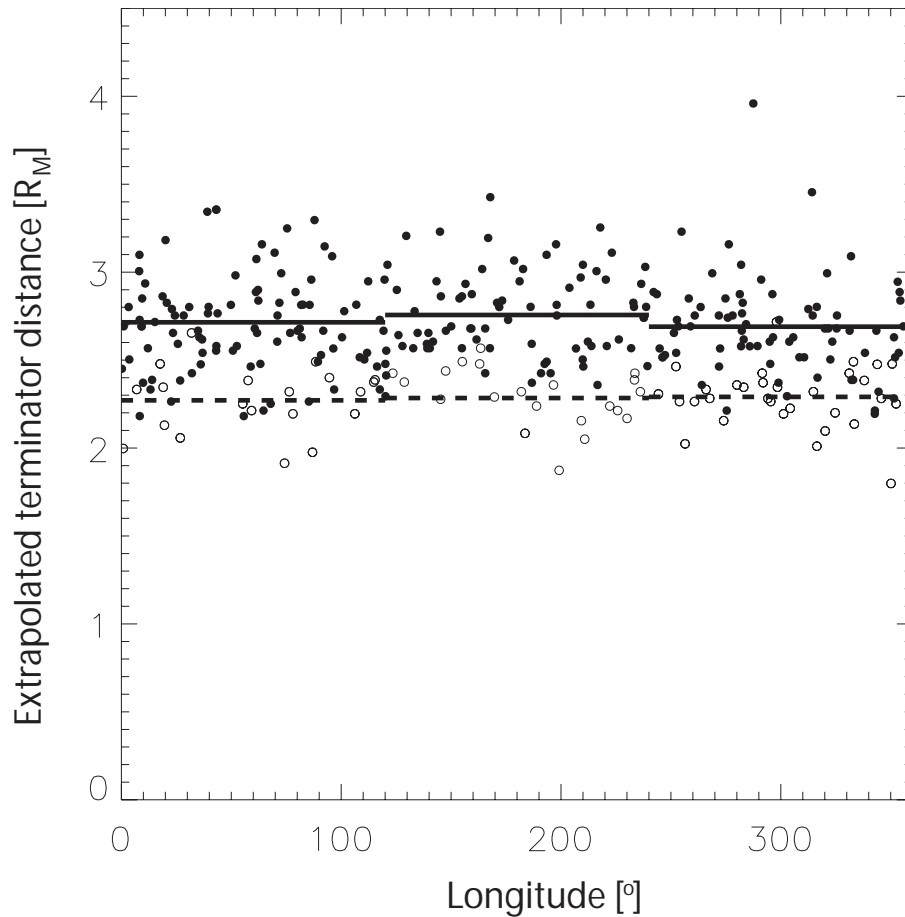


Figure 3.4: The extrapolated terminator distance of all dayside BS crossings plotted versus planetary longitude. The filled circles indicate crossings over the southern hemisphere while open circles indicate crossings over the northern hemisphere. The solid and dashed lines indicate the average distances over the southern and northern hemisphere, respectively. There is no separation to indicate strong or weak crustal fields as is done in Figure 3.3. The figure shows that the BS crossings observed over the southern hemisphere are on average farther out than BS crossings observed over the northern hemisphere.

Dividing the BS crossings into the same regions as the MPB crossings does not provide the same clear results. The BS crossings in the southern hemisphere in the longitude range $120^\circ - 240^\circ$ are farther out than in the northern hemisphere in the same longitude range, but the low ($< 120^\circ$) and high ($> 240^\circ$) longitude crossings over weak crustal sources are actually slightly higher in the mid-latitudes. Other factors such as dynamic pressure or IMF direction seem to be governing in these mid-latitude regions which could explain the relatively lower BS altitude. It appears as if the BS is not affected enough by the mid-latitude crustal fields but only by the strongest crustal fields in the southern hemisphere and there it is being affected over large scales across the southern hemisphere.

Also, dividing the MPB crossings simply into northern and southern hemisphere crossings gives an insignificant difference in the average distance of southern and northern crossings in the longitude range from 0° to 120° as well as in the longitude range $240^\circ - 360^\circ$. This is expected since the strong crustal sources are located in the mid-latitudes in these longitude ranges and thus affects the southern and northern hemispheres equally.

The north-south asymmetry of the BS found in this study using MGS MAG/ER data has been supported by MEX ASPERA-3 measurements (*Dubinin et al.*, 2008a). They found that in the longitude range $130^\circ - 240^\circ$ in the southern hemisphere the crustal sources provide essential additional pressure and lift the MPB upward by 400 – 500 km. The asymmetry in the obstacle shape (the MPB) to the solar wind in turn causes an asymmetry in the BS location (*Dubinin et al.*, 2008a). A hybrid model simulation of the solar wind interaction with Mars, which includes the crustal fields, do not show any global changes in altitude of the BS, whereas the MPB seems to be af-

ected more, and especially over strong crustal sources where it forms more of a magnetopause-like structure (*Harnett and Winglee, 2007*).

We have also studied the upstream IMF direction in the 10 min interval upstream of each crossing, and searched for any preferred orientation that could explain the north-south asymmetry. However, we do not find any such IMF orientation for the BS crossings in either of the two hemispheres that could add to the asymmetry in altitude. It should be said that determining the orientation of the IMF from the upstream field is difficult. The spacecraft field can cause errors in the measurements (*Crider et al., 2001*), and the 10 min averages also introduce an error since the orientation of the field can change rapidly. *Vignes et al. (2002)* did indeed find that the upstream IMF affected the position of the BS but they only used a small portion of the data points when there was a very steady field orientation. In this study we use all the data points and not just the ones with a steady upstream IMF and find that, independent of IMF orientation, the southern BS is almost always farther out than the northern BS. There does not appear to be any orbital effect that could account for this asymmetry, either. There are more BS crossings in the southern hemisphere than in the northern hemisphere due to orbit geometry but otherwise they do not have any preferred location relative to the planet that could account for the observed asymmetry in BS location.

3.2.3 Magnetic field strength at the magnetic pileup boundary

The MPB is the outer boundary of the MPR which develops as the IMF drapes around the planet (*Nagy et al., 2004*). The upper panel of Figure 3.5

shows the mean magnitude of the magnetic field $\langle |\mathbf{B}| \rangle$ in the inner part of the MPB (that is the outer part of the MPR) as a function of SZA and the error bars show the standard deviation of the data $\sigma_{|B|}$. The lower panel shows $\sigma_{|B|}$ normalized to $\langle |\mathbf{B}| \rangle$ as a function of SZA so that the relative values can be seen. The data are binned into 5° bins ranging from a SZA of 25° up to 130° . *Brain et al.* (2003) examined the relative magnitudes of the IMF and the planetary crustal field, whereas *Crider et al.* (2004) studied only the IMF contribution to the magnitude of the draped field. However, these studies binned data based on altitude, local time, SZA and geographic location. Since the plasma environment is highly dynamic and the boundaries move back and forth with time, that binning method results in data being taken from different regions of the plasma environment. This study focuses instead on the field magnitude in the MPB by binning the data after checking where the MPB is actually located during each orbit. This ensures that we bin data solely from the boundary region. We use the maximum magnetic field strength during each MPB crossing in our binning. Crossings that occur where the crustal field exceeds 5 nT are excluded. This is checked by using the crustal field model by *Cain et al.* (2003). As expected, the field magnitude in Figure 3.5 is higher compared with values obtained in the studies by *Brain et al.* (2003) and *Crider et al.* (2004), by about 25 – 50%, since we do not sample any sheath magnetic field which is on average lower than the maximum magnetic field in the MPB. The magnitude of the magnetic field in the MPB is found to be around 40 nT on the dayside of the planet, and to decrease almost linearly with SZA towards the nightside where it is on average around 15 nT. The draped flux tubes within the MPB are thus most strongly compressed in the subsolar region, as expected, but expand around

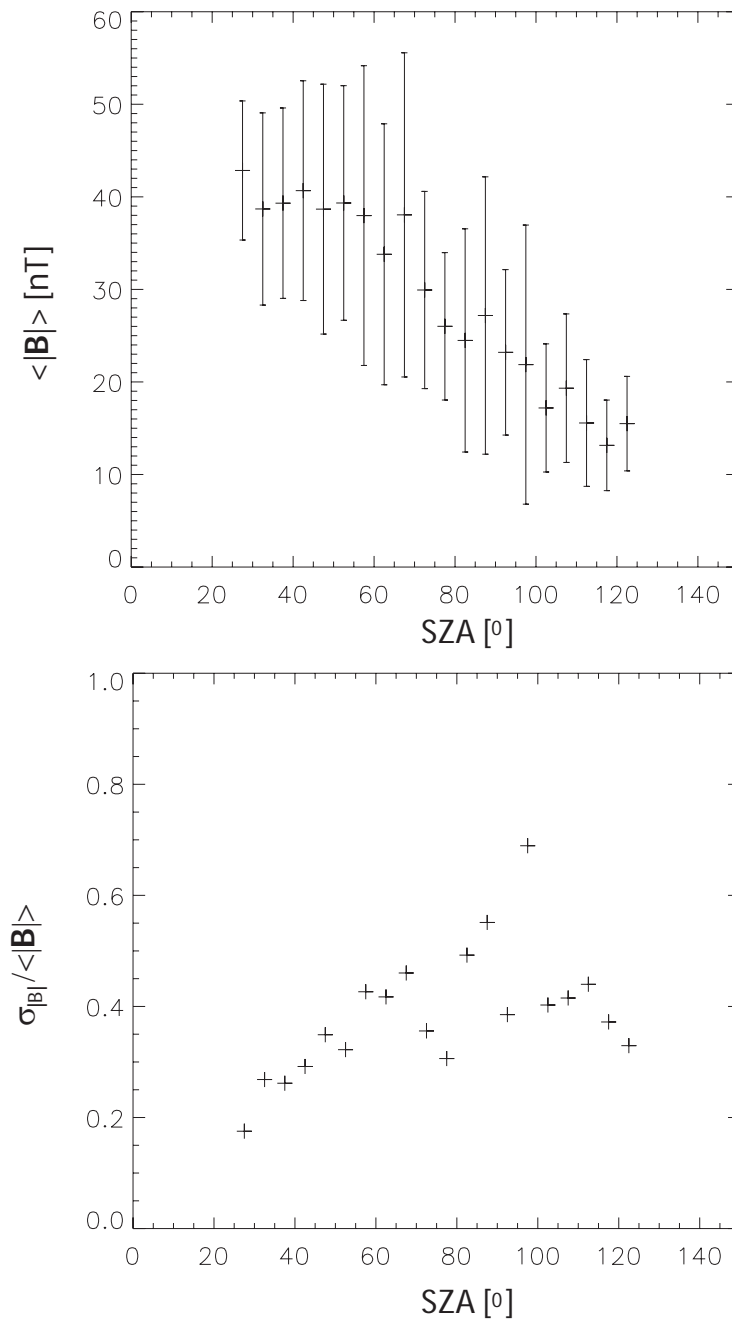


Figure 3.5: The upper panel shows the mean magnetic field strength at the inner surface of the MPB as a function of SZA, binned in 5° bins. The error bars show plus or minus one standard deviation $\sigma_{|\mathbf{B}|}$ about the average values. The lower panel similarly shows $\sigma_{|\mathbf{B}|}$ normalized to the mean $|\mathbf{B}|$ value in each 5° bin, versus SZA.

the planet into the nightside. While the magnitude of the mean magnetic field strength decreases towards the nightside, the relative variation of the field strength actually increases towards the nightside.

In Figure 3.6 the mean field strength variation with altitude within the dayside MPB is shown in four altitude sections and sub-divided into high ($> 60^\circ$) and low ($< 60^\circ$) SZA. The altitude sections are chosen as $0.0 - 0.1$ and $0.1 - 0.2 R_M$ above and below the average location of the MPB (the dashed lines in Figure 3.6 indicate the four regions) and the SZA division is at an angle of 60° . The field strength in the MPB is clearly seen to increase as the MPB moves toward the surface of the planet, implying that when the solar wind dynamic pressure pushes the boundary closer to the planet the magnetic flux piled up in front of the planet must be stored in a smaller volume and the magnetic field strength thus increases. The field strength in the outer region (higher altitude) is of order 70% of that in the inner region (lower altitude), for both high and low SZAs.

3.3 Summary and conclusions

We have analyzed the full pre-mapping data set from the MGS MAG and ER instruments. The study has focused on the shape and location of the two boundaries as well as on the effects of the crustal magnetic fields on the location of the MPB and BS. We also study the magnetic field strength inside the MPB.

The pre-mapping data set contains sixteen months of data with good coverage in SZA, local time, and altitude. We use this to search for crossings of the MPB and BS and find 993 and 619, respectively. The MPB appears

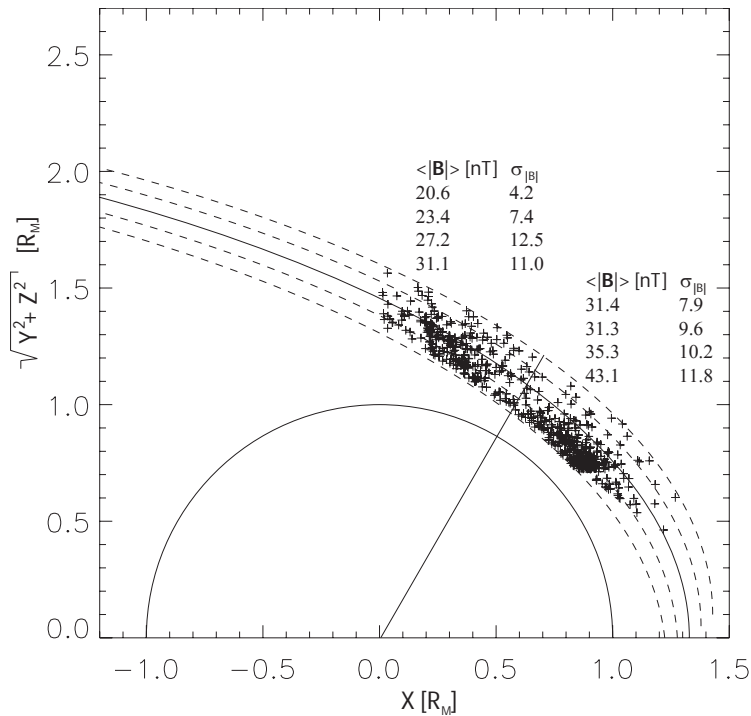


Figure 3.6: All dayside MPB crossings are shown in aberrated cylindrical MSO coordinates (crosses), together with the best fit (solid line). Two regions on either side of this best fit line are then indicated by dashed lines, each region being $0.1 R_M$ wide. The altitude sections are also subdivided into SZAs less than 60° and SZAs larger than 60° , indicated by the tilted solid line. The average magnetic field strength and their standard deviations of the MPB crossings observed in each of the eight regions are shown. The upper left value (20.6 nT) is the average magnetic field strength of the MPB crossings observed in the top region of the large SZA division, etc.

as a permanent boundary in the Martian plasma environment, and is the boundary where the IMF starts to pile up upstream of the obstacle. Its location is to a large extent governed by the pressure balance between magnetic pressure on the inside and solar wind dynamic pressure on the outside. In a time series from MGS MAG/ER it is identified by a sudden increase in magnetic field magnitude together with a drop in field fluctuations as well as a drop in electron flux. The increase in field magnitude is larger on the dayside than on the nightside and the scatter in position of the boundary is more extensive on the nightside.

The shape and location of the MPB and BS are found to be in agreement with previous studies but with some smaller differences in stand-off distance and tail radius. We introduce a new fitting technique which gives a more realistic MPB shape by making sure that the lowest altitude of the boundary is at the subsolar point.

The crustal fields are shown to play an important role in the location of the MPB as well as the BS. The additional magnetic pressure from the crustal sources forces the MPB to higher altitudes over the large scale regions where there are stronger crustal fields. By extrapolating each MPB crossing to the terminator line and dividing them into whether they are observed over regions of weak or strong crustal fields we find that the crossings that occur over regions with intense crustal magnetic fields are on average located farther out. We have repeated this division in three longitude ranges and obtained the same result in all three regions. For the MPB, the extrapolated terminator distances are on average farthest away in the longitude range $120^\circ - 240^\circ$ within the latitude range from -90° to 0° , which is coincident with where the strongest crustal fields sources are located. This clear distinction

between weak and strong crustal field regions is not seen for the BS crossings. This is at least partly expected since the magnitude of the crustal fields falls off with altitude and it gets more and more disturbed by the surrounding plasma environment. However, on a global scale the crustal field still appears to make a large difference since the BS crossings observed over the southern hemisphere are located significantly farther out than the northern hemisphere crossings. The BS does not seem to be affected by the intermediate crustal field strength in the mid-latitude regions and that indicates that there might be a threshold crustal field strength required to lift the BS. It has not been possible to relate this asymmetry to any particular upstream IMF orientation or orbit geometry effect. The observed asymmetry in both the MPB and BS altitude is supported by measurements from MEX.

The magnetic field strength at the inner edge of the MPB is found to be about 40 nT on the dayside (no crossings could be observed below a SZA of 20° due to orbit constraints), and decreases to about 15 nT on the nightside. The decrease toward the nightside agrees with what is expected from a gas-dynamic modelling: as the obstacle surface becomes more tangential to the solar wind flow, more and more magnetic flux slips by the obstacle and hence the flux decreases (*Spreiter and Stahara, 1980*). The flux tubes also expand downstream of the subsolar point and the field magnitude thus decreases. The variation in field strength is quite large and the uncertainty of the average values becomes large. The field strength is shown to increase rapidly with decreasing altitude. A MPB crossing observed closer to the planet implies, in general, a larger magnetic field strength in the MPB and a MPB crossings observed at higher altitude implies smaller field strength.

Chapter 4

Rosetta and Mars Express simultaneous measurements of the effects of low and high solar wind pressure

In this Chapter we analyze the measurements made by the Rosetta spacecraft during its swingby of Mars together with the simultaneous measurements made by MEX. The data analysis is divided into two parts. First, we perform a two-spacecraft near-simultaneous plasma boundary study at Mars by using both Rosetta and MEX measurements during quiet solar wind conditions. Secondly, we examine the effects of a high pressure solar wind region on the Martian plasma environment by using Rosetta as a solar wind monitor while MEX samples the plasma environment over several days. Some of the material presented in this Chapter is published in *Edberg et al. (2009c)* and included in *Edberg et al. (2009a)*.

4.1 Introduction

As the Rosetta spacecraft performed a flyby of Mars on February 25, 2007, the rare event of a two-spacecraft investigation of the Martian plasma environment, together with MEX, became possible. Out of all the past missions to Mars, with plasma instruments onboard, only two have been in operation at the same time: MGS and MEX. Results from a study using MGS and MEX are presented in Chapter 5.

Hence, the Rosetta Mars flyby is the first opportunity for coordinated plasma measurements near the Martian BS and MPB. The Rosetta and MEX trajectories during the Mars flyby are presented in Figure 2.3 as blue and red lines, respectively.

4.2 Simultaneous observations during low solar wind pressure

To enable us to find the locations of the BS, MPB and PEB, which are our prime targets in this study, Figure 4.1 shows the Rosetta ROMAP magnetic field data from the inbound leg of the Rosetta Mars flyby. Data are shown as total field strength and x , y and z -components in MSO coordinates. The expected crustal magnetic field strength from a model by *Cain et al.* (2003) is also shown as well as the altitude of Rosetta. For the outbound leg, a summary of RPC data are shown in Figure 4.3. The MEX measurements during this interval are presented in Figure 4.4. These plots form the basic material for the following Sections where we will first describe the Rosetta plasma boundary crossings and then the simultaneously occurring MEX boundary

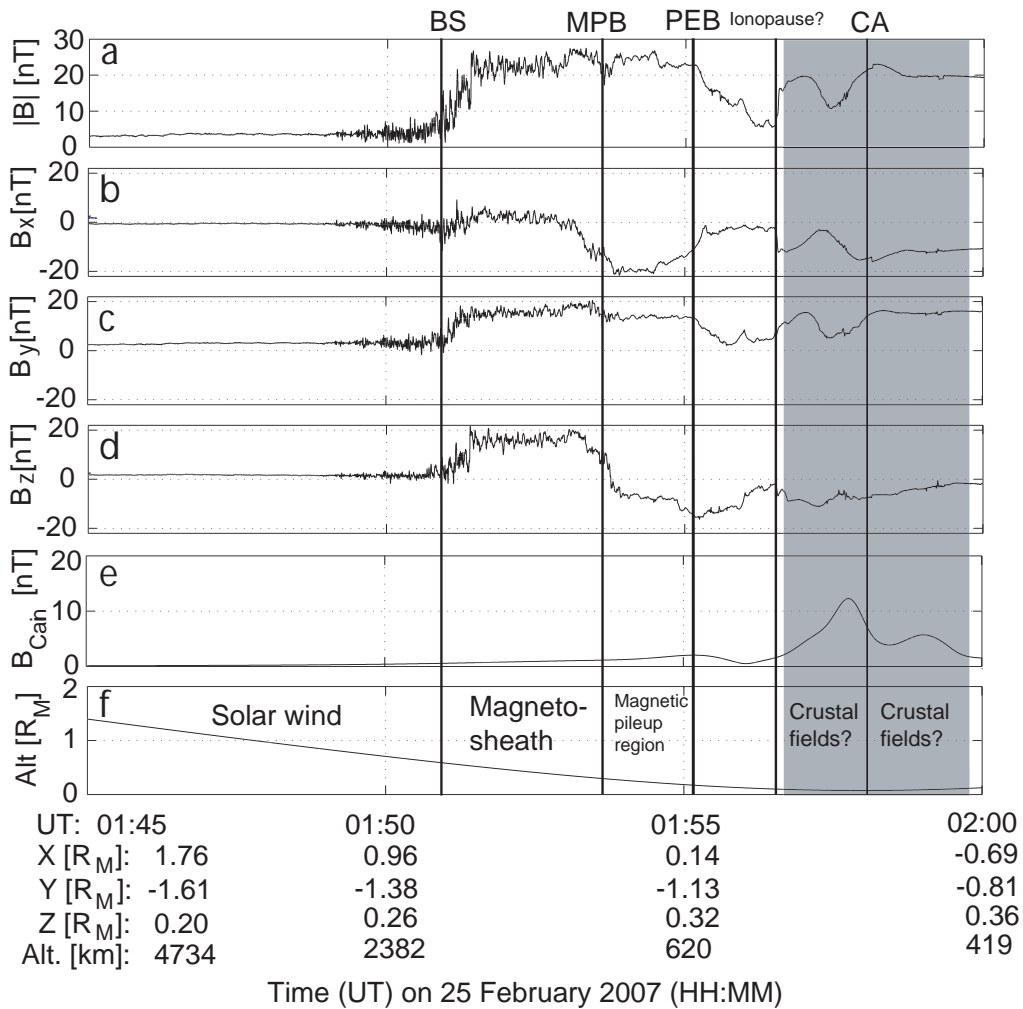


Figure 4.1: Time series of Rosetta data from around CA of Rosetta. The panels show (a) the magnetic field strength, (b, c and d) the MSO x , y and z -components of the magnetic field, (e) the expected crustal magnetic field from the Cain *et al.* (2003) model and (f) altitude of Rosetta. The BS is observed at 01:51 UT, the MPB at 01:54 UT, the PEB at 01:55 UT and a signature of a passage into the ionopause at 01:57 UT, all indicated by black vertical lines. The grey shaded area indicates where the crustal magnetic fields are observed.

crossings.

4.2.1 Dayside bow shock crossing

The increased magnetic field strength and level of turbulence occurring in a wide interval around 01:51 UT (Figure 4.1, panel a - d) is identified as the BS. The upstream IMF in Figure 4.1 has a field strength of ~ 2 nT and is directed slightly tailward and toward the positive y -hemisphere and toward ecliptic north, which is in agreement with the normal Parker spiral configuration. With some caution for possible magnetic field offsets, this magnetic field direction together with the flyby geometry (Figure 2.3) suggests that we should encounter a quasi-parallel BS, (the θ_{Bn} angle, i.e. the angle between the IMF and the normal to the BS, is close to 0). While the separation into quasi-parallel and quasi-perpendicular shocks is less relevant for Mars than for Earth for several reasons (e.g. small obstacle scale size with respect to the ion gyro radius and substantial exospheric ionization, see *Mazelle et al.* (2004) for a review), a quasi-parallel shock nature is indeed consistent with the gradual increase in magnetic field strength seen around 01:51 UT, which we will see contrasts drastically to what we observe on the outbound leg (Section 4.2.4). The fluctuations seen from around 01:49 UT cannot be taken as an indication of interaction of the solar wind with back streaming ions upstream of a quasi-parallel shock as such activity at Mars is found also upstream of the quasi-perpendicular BS, presumably because of the ionization of exospheric neutrals (*Mazelle et al.*, 2004).

4.2.2 Dayside MPB and PEB crossings

The major rotation of the magnetic field at 01:54 UT, in combination with a decrease in fluctuations of the magnetic field at the same time, is interpreted as the MPB crossing. The MPB can normally be identified by three specific signatures in magnetic field data: a sudden increase in field strength, a decrease in field fluctuations and an enhanced draping of the field lines around the planet (*Brain et al.*, 2005). Here we only see two of those signatures, a decrease in field fluctuations and a draping (or change in orientation, mainly of the B_x and B_z component) of the field lines. The increase in field magnitude is less clear in the data.

The lack of an actual piling-up of magnetic field during this event could be associated with a change of the boundary location. One minute before the MPB crossing, at 01:53 UT, there is another signature in the magnetic field data suggesting an additional plasma region or perhaps more likely, an effect of a temporal and spatial change in the plasma environment. The characteristic magnetosheath fluctuation of the magnetic field does not stop at 01:53 UT but rather at 01:54 UT and Rosetta should still be in the magnetosheath by 01:53 UT. However, there could have been a first MPB crossing occurring at 01:53 UT, followed by a moving in of the MPB which should then have passed by Rosetta inward. A slow decrease in field magnitude should then be observed, and there is also in fact a short interval between 01:53 UT and 01:54 UT where the field strength decreases. The MPB is then finally crossed again at 01:54 UT. However, since we do not have two-point measurements, we can only speculate upon this.

An analysis of how the x -component of the magnetic field (B_x) varies with the cylindrical radial component perpendicular to the x -axis (B_r), as used

by *Israelevich et al.* (1994) and *Bertucci et al.* (2003), displays the draping effect of the magnetic field around the planet. This helps in determining different spatial regions in the plasma environment and especially the difference between the MPR and magnetosheath. The results are shown in Figure 4.2. Panel (a) shows a shorter time series from the ROMAP measurement from when Rosetta is just inside the BS until Rosetta is well within the MPB. Panel (b) shows B_r as a function of B_x for the interval marked in red in panel (a) when Rosetta is in the magnetosheath and there is no strong correlation. However, between second 100 and 145 in panel (b) there is a tendency of a correlation, which would correspond to the interval when the MPB moves inward as discussed in the previous paragraph. A fit to this interval (blue line) using linear regression only yields a coefficient of determination of 0.54 and a fit to the interval from 0 to 100 seconds (red line) gives a coefficient of determination of only 0.02. Panel (c) shows B_r as a function of B_x for the green interval in panel (a) when Rosetta is clearly inside the MPR. The green line is a fit to this data. The coefficient of determination for this line is 0.78. This reveals how the draping of the IMF is enhanced after 01:54 UT and thus makes us confident that we are really inside the MPB at this time.

At 01:55 UT in Figure 4.1 the field strength starts to decrease slowly. Having no electron measurements at this point it cannot be said for sure but the location of Rosetta when this decrease starts suggests that it is in fact the crossing of the PEB. The position of the crossing is in good agreement with where MEX crosses this boundary (see Section 4.2.5 and Figure 4.5). A sharp change of the magnetic field occurs at 01:56:30 UT at an altitude of 360 km. This could possibly be a signal of a passage into the ionosphere. The two peaks in the field strength that then follow at 01:57 UT and 01:58 UT could

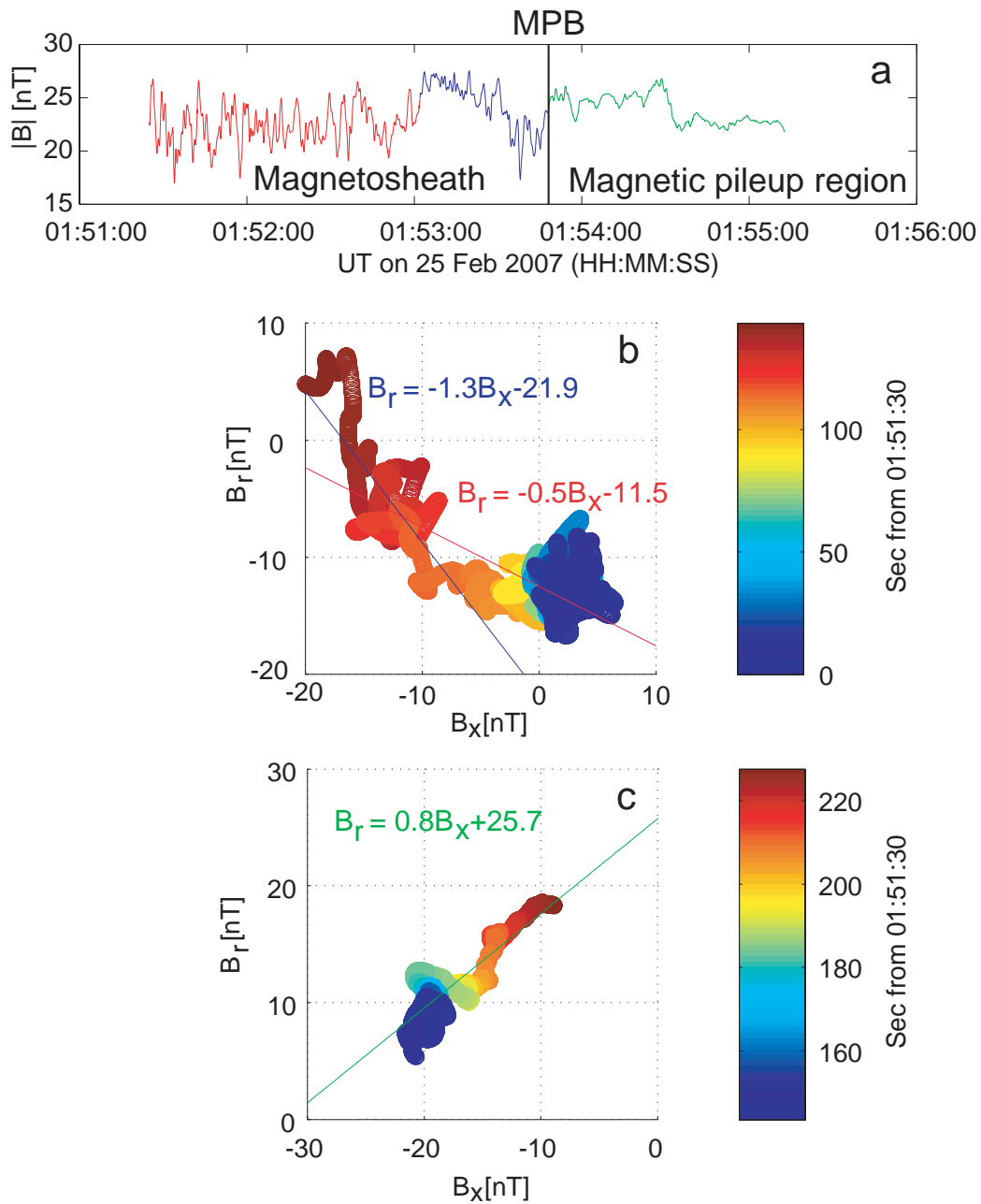


Figure 4.2: A shorter time series than that is shown in Figure 4.1 of the ROMAP data is displayed in panel (a). Panels (b) and (c) show the radial component of the magnetic field plotted as a function of the x -component for two time intervals indicated by the red and green colours in panel (a), which correspond to the magnetosheath and the MPR, respectively. The red, blue and green lines are fits to different intervals as explained in the text.

be signatures of crustal magnetic fields. Looking at the crustal field model by *Cain et al.* (2003), the two peaks observed in the ROMAP data are close to what is expected, except for a short time difference of about 1 minute, which may well be due to plasma effects which are specifically excluded from the Cain model. The Cain model was restricted to only use data from below 200 km altitude and only from the dayside. The measured magnetic field is a combination of draped IMF and crustal fields and hence the magnitude of the Cain model is expected to be less than the measured values. Even though the morphologies of these signatures are somewhat different from what was measured by MGS we believe that it is likely that these are indeed crustal magnetic fields. *Boesswetter et al.* (2009) used the second version of the crustal field model from (*Purucker et al.*, 2000) and also found a clear crustal magnetic field signature in the de-trended ROMAP data.

4.2.3 Flank MPB crossing

Figure 4.3 shows a time series of measurements by the Rosetta IES, MAG and LAP instruments on the outbound leg from 02:55 UT, just after the payload turn-on following the shut-down period around CA, until 04:30 UT. The altitude above Mars and the spacecraft SAA are also displayed in the Figure. The SAA is of interest as it determines the perturbation on the LAP V_{ps} measurement from the solar panels, and also determines if the solar wind enters the IES field of view. The density data in panel (f) in Figure 4.3 was produced by using the calibration function between Rosetta LAP and MEX ELS as described in *Edberg et al.* (2009c). The IES instrument was behind the spacecraft (with respect to the solar wind flow) during this interval and thus did not see the entire distribution of streaming solar wind

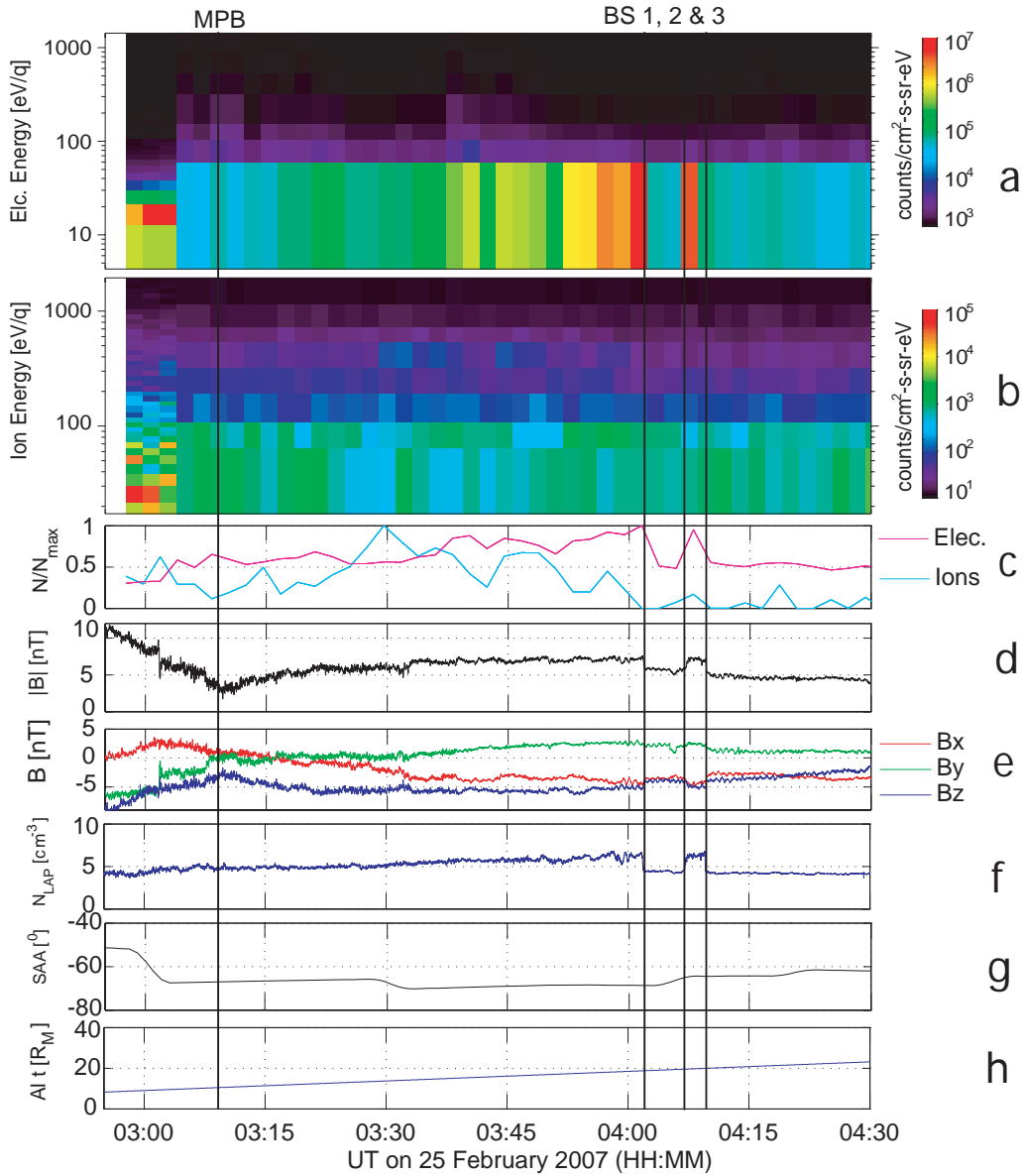


Figure 4.3: Time series of the measurements made by three of the RPC instruments during the outbound leg of the Rosetta flyby. The panels of the figure show (a) electron and (b) ion omni-directional energy spectrograms from the IES instrument, (c) the relative ion and electron densities calculated from the IES instrument, (d) the magnetic field strength as measured by MAG, (e) the x , y and z -components of the magnetic field in MSO, (f) the plasma density as measured by LAP (calibrated as described in Edberg *et al.* (2009c)), (g) the SAA and (h) altitude. The outbound MPB is observed at 03:10 UT and the three outbound BS crossings are observed at 04:04 UT, 04:07 UT and 04:09 UT, all indicated by black vertical lines.

and magnetosheath particles. For IES, we therefore only present the relative changes in the ion and electron number density, from density moments of the ion and electron distribution. While the flowing ions are hidden from the instrument, the electrons have higher thermal speed and can more easily reach the instrument, giving a more reliable density moment. The IES energy spectrograms changes energy resolution at about 03:03 UT which is clearly seen in the data. After this change, the electron and ion fluxes are seen to drop sharply at 60 eV since the first energy channels goes up to this energy level. Both spectrograms were generated by summing counts over all elevations and azimuth angles and hence the direction information is lost in the energy spectrogram. It should be noted that there is good covariation between the LAP and IES electron density variations, giving confidence in the measurements.

The Rosetta trajectory was close to tangential to the plasma boundaries during the outbound leg. This may explain the gradual magnetic field gradient at the start of the interval, which we interpret as a stretched MPB. We note that the significant change at 03:02 UT is likely to be an artefact introduced by the changing attitude. The MPB position is thus not fully clear, but on moving from inside the MPB to outside, the decrease in magnetic field magnitude is gradual but with a distinct minimum at 03:10 UT where there is again a rotation of the field direction, an effect of the IMF draping around the obstacle, and we therefore identify this as the MPB.

4.2.4 Flank magnetosheath and bow shock crossings

Throughout the first hour in Figure 4.3, there is a gradual increase in the V_{ps} which has been translated to number density N_{LAP} (Figure 4.3, panel (f))

Table 4.1: Results from the MVA on the three outbound leg BS crossings. The three components of the normal vector (eigenvector with smallest corresponding eigenvalue) are given for each BS crossing as well as the three eigenvalues of the covariance matrix. ϕ is the angle between the MVA normal vectors and the expected local boundary normal from Trotignon *et al.* (2006), given by (0.26,0.97,0.0).

	\hat{x}	\hat{y}	\hat{z}	λ_3	λ_2	λ_1	ϕ
BS 1	0.50	0.87	-0.07	0.004	0.027	0.54	15°
BS 2	-0.27	0.86	0.43	0.005	0.045	0.14	40°
BS 3	0.25	0.96	0.11	0.020	0.053	0.39	6°

according to the cross-calibration in *Edberg et al.* (2009c) (see also Section 2.5). As Rosetta continues out through the magnetosheath there is a continuous increase in probe-to-spacecraft potential and electron density. This could be interpreted as an increase in plasma flow through the Martian magnetosheath at this time, due to a hypothetical increase in the solar wind flow (see discussion in Section 4.3). The density increase is observed to continue until the BS is crossed outbound at 04:04 UT. The crossing of the BS is consistently observed in LAP, MAG and IES data. Possibly due to the changing plasma conditions, the BS moves outward again and passes by Rosetta at 04:07 UT. At 04:09 UT, after an additional 2 minutes in the magnetosheath, the BS is once again crossed.

A minimum variance analysis (MVA) (*Bertucci et al.*, 2005) is used to find the local normal to the three BS crossings, in order to get a sense of the shape of the boundary in comparison to models. The x , y and z -components of the normal vectors from the MVA for the three BS crossings are shown in Table 4.1, together with the eigenvalues λ_1 , λ_2 and λ_3 of the eigenvectors of the covariance matrix in the MVA.

The angle ϕ between the normal vector obtained from the MVA to the

expected boundary normal from *Trotignon et al.* (2006) is also shown. During the first and third crossings on the outbound leg, the normal direction is very close to parallel to the local normal to the conic section, assumed to represent the average surface boundary (*Trotignon et al.*, 2006), in the $x - y$ plane and with a small z -component, which is expected. However, for the second of the three outbound BS crossings, the normal obtained from the MVA analysis is tilted in the downstream direction and with a larger z -component, suggesting that the BS moved outwards in a wave motion propagating downstream. We note that the magnetic field direction in the solar wind (Figure 4.3) and the BS normal directions at the two outbound crossings are consistent with a quasi-perpendicular BS. This is also indicated by the discontinuous nature of the observed BS crossings, in distinct contrast to the dayside BS (Figure 4.1). However, as discussed in Section 4.2.1, the smeared-out nature of the inbound BS may be more due to its proximity to the planet, putting it inside the Martian exosphere, rather than to the effects of its normal direction with respect to the IMF (*Mazelle et al.*, 2004).

4.2.5 Mars Express observations

The MEX orbit on February 25, 2007, was close to the terminator plane with periapsis of ~ 310 km altitude in the $+y/-z$ -hemisphere and apoapsis of about ~ 10000 km altitude in the $-y/+z$ -hemisphere. A time series of the ion and electron measurements from IMA and ELS at this time is plotted in Figure 4.4 together with the velocity and density moments. The solar wind is slightly slower than average at this time, below 300 km s^{-1} , with a density of $\sim 1\text{-}2 \text{ cm}^{-3}$. Meanwhile, the ROMAP data from Rosetta indicates that the IMF strength is quite ordinary and aligned with the expected Parker spiral

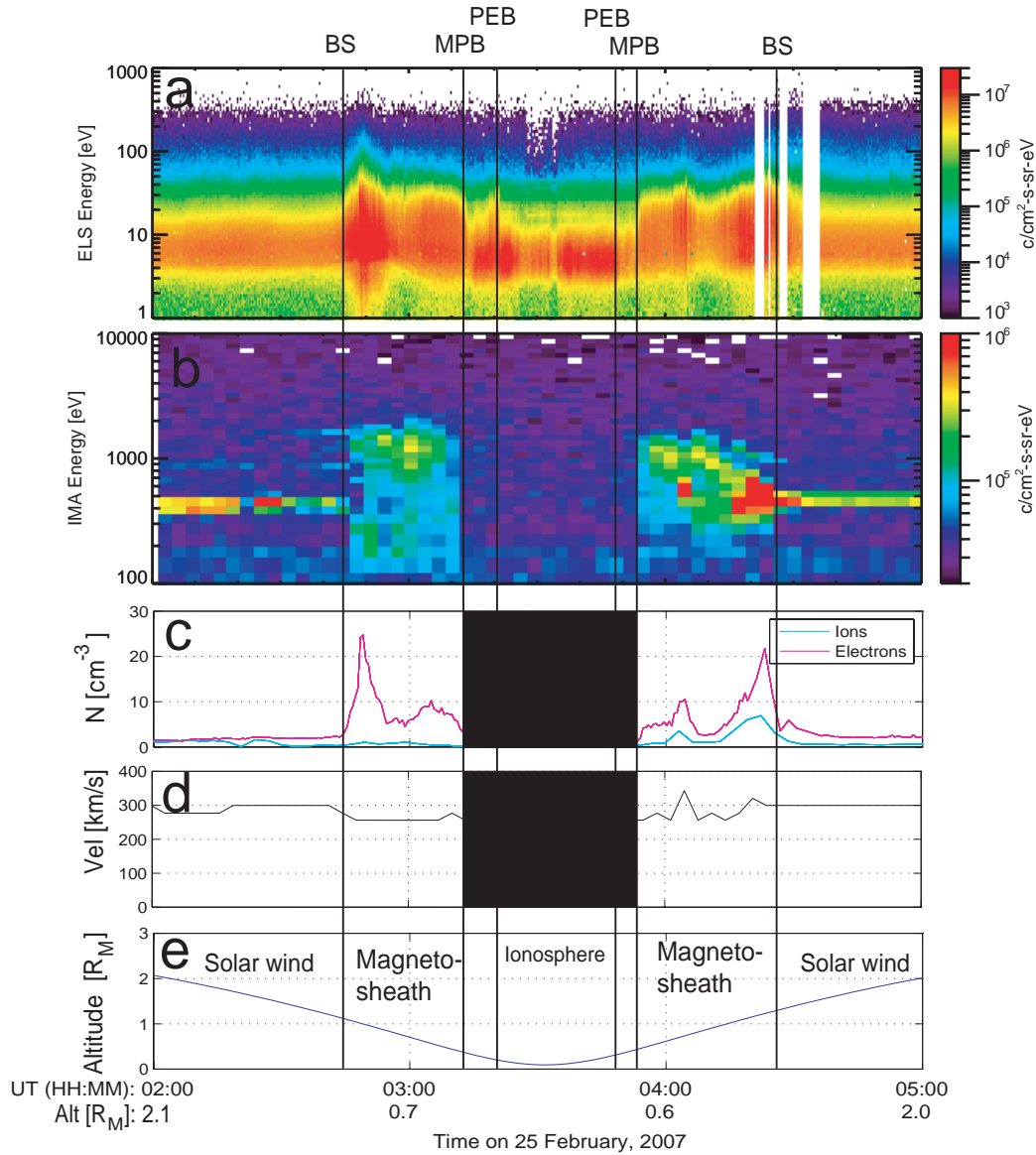


Figure 4.4: MEX ASPERA-3 measurements from 25 February, 2007. The panels show (a) electron and (b) ion omni-directional energy spectrograms, (c) ion and electron density moments, (d) plasma velocity and (e) altitude. The inbound BS, MPB and PEB crossings occur at 02:44 UT, 03:13 UT 03:22 UT, respectively, while the outbound PEB, MPB and BS occur at 03:50 UT, 03:55 UT and 04:30 UT, respectively (black vertical lines).

direction, see Section 4.2. During the inbound crossing of the BS and the MPB by Rosetta at 1:51 UT and 1:53 UT, respectively, MEX was in the solar wind. Figure 4.4 shows that the solar wind was quiet for a long period before the Rosetta CA at 01:58. Based on the MEX observations it is reasonable to assume that the upstream conditions during the Rosetta inbound leg were constant. Rosetta ROMAP data (Figure 4.1) and Rosetta MAG data (Figure 4.3) show that the IMF has changed sign of the z -component from before the flyby until after the flyby, while the field strength has not changed significantly.

During the full orbit of MEX, the spacecraft encountered several regions and boundaries in the Martian plasma environment, as can be seen in Figure 4.4. First, MEX was in the solar wind until 02:44 UT when the spacecraft crossed the BS, and was thereafter located in the Martian magnetosheath. The magnetosheath was clearly identified by the appearance of solar wind electrons heated at the BS crossing. A similar signature was observed in the ion spectrogram. At 03:13 UT a significant change in the ion and electron fluxes occurred. The sudden disappearance of magnetosheath electrons is interpreted as a crossing of the MPB. At 03:22 UT the PEB is crossed, detected in the ELS data by the appearance of a spectral line at energy of 20 - 30 eV. MEX stayed inside the Martian PEB for 28 minutes, until 03:50 UT when the spacecraft crossed the PEB outbound. The MPB was crossed outbound at 03:55 UT and again the magnetosheath was entered before finally the solar wind region was reached after having crossed the BS at 04:30 UT.

4.3 Shape and location of the plasma boundaries

The positions and times of all MPB, PEB and BS crossings observed by Rosetta and MEX, as reported in the previous sections, are indicated in Figure 4.5, on two different scales. Also shown are the orbits of MEX and Rosetta in cylindrical MSO coordinates and the average BS and MPB locations from *Trotignon et al. (2006)* plotted as solid green and red lines. We use the model of *Trotignon et al. (2006)* since it has been specifically developed to model the boundaries far downstream which is where we have some of our boundary crossings in this study. The dashed green line is a conic section fit to the three BS crossings closest to the planet that were observed by both Rosetta and MEX and the dashed blue line is a fit to the three PEB crossings. The inbound MPB crossing by MEX and the outbound MPB crossing by Rosetta are only separated by 3 minutes in time. The outbound BS crossing by Rosetta is observed approximately 20 minutes before the outbound BS crossing of MEX. This makes these measurements the first near-simultaneous two-spacecraft measurement of plasma boundaries at Mars. The observations of the PEB by Rosetta and MEX are separated 1.5 hours in time making them far from simultaneous. The time-scales on which these three boundaries move significantly can be anything between a couple of seconds up to perhaps hours depending on solar wind variability. During the time of the Rosetta flyby the solar wind conditions are steady and slow, when observed by either of the two spacecraft. What happens to the solar wind during the time when both spacecraft are inside the BS is unknown, but considering the stable situation before and after this interval, a reasonable assumption

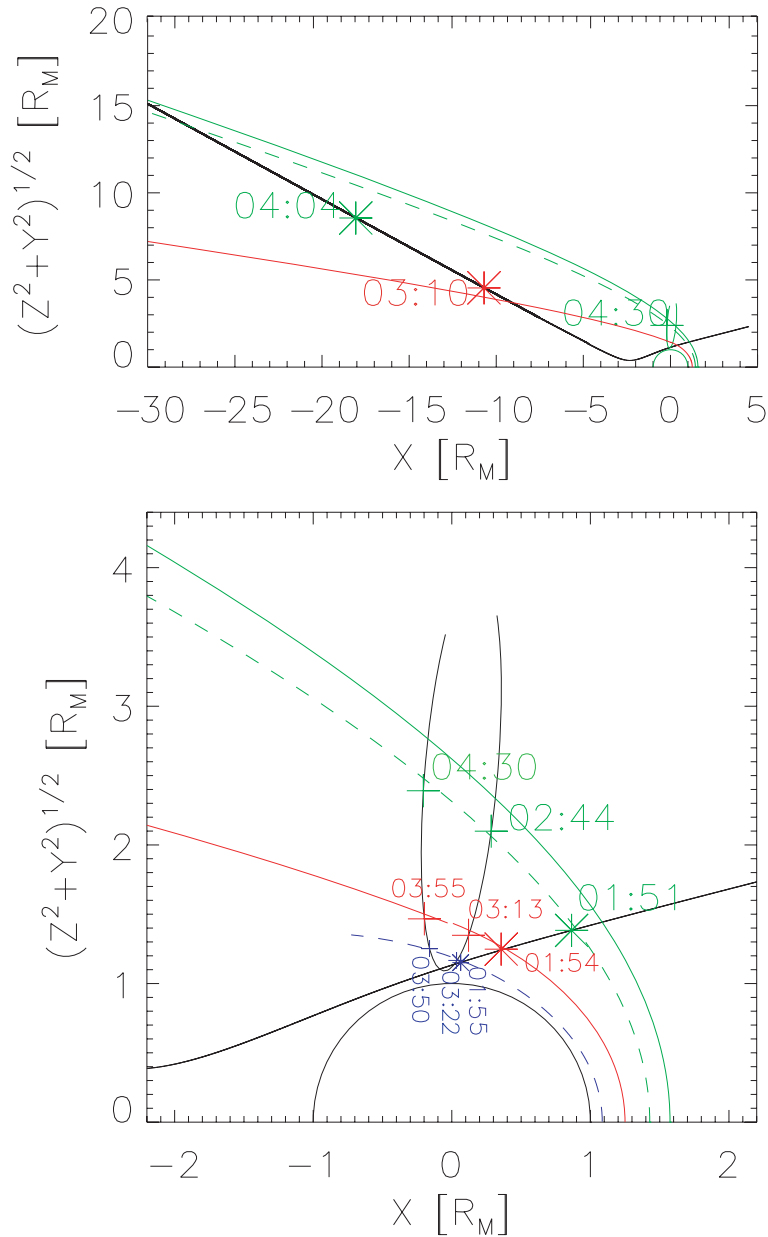


Figure 4.5: The trajectories of Rosetta and MEX on 25 February 2007 plotted in cylindrical MSO coordinates and shown in two scale sizes. The green and red solid curves are the average positions of the BS and MPB from Trotignon *et al.* (2006). The positions of the boundary crossings observed by Rosetta and MEX are displayed as green (BS), red (MPB) and blue (PEB) stars and plus signs. Stars refer to Rosetta observations and plus signs to MEX. The time, in UT, of each crossing is also indicated. The dashed green line is a fit to the three BS crossings closest to the planet (see text for further details on the fitting) and the blue dashed line is a fit to the PEB crossings.

is that the solar wind does not vary very much, except for a change in the sign of B_z . However, this leaves unexplained the observed continuous density increase (as indicated from the probe potential measurements and also to some extent from the IES electron moment) seen during the outward passage through the magnetosheath (Figure 4.3 and Section 4.2.4). There is of course the possibility of a short-time change in the solar wind in the time-interval between the last Rosetta MPB crossing and the last Rosetta BS crossing which could cause the density increase. The increase is less than a factor of two in N_{LAP} which is within the error margins of the density calibration so there is also the possibility of the increase being unphysical. However, even though the calibration has an error margin, the individual V_{ps} measurements should not have a time-dependent error that would cause a factor of two increase over about one hour, which suggests that the increase is indeed real. There is also a simultaneous increase in the magnetic field strength at this time which supports the interpretation of this being physical.

We compare our measurements of the MPB and BS with previous models of the shape of the two boundaries. For the BS, a conic section is fitted to the three farthest upstream BS crossings (dashed curve in Figure 4.5). The fitting is done by altering the semi-latus rectum of the conic section from the best fit value of *Trotignon et al.* (2006) until the root mean square of the distances from each BS crossing to the proposed fit reaches a minimum, as described in Section 3.2.2. However, this fit does not agree with the farthest downstream BS crossing. This suggests that the shape of the BS may well be represented by a conic section but the entire boundary does not seem to move like a rigid body but rather alters its shape somewhat. In this case, it becomes more compressed in the far downstream region. For the MPB on

the other hand, all crossings are reasonably close to the average position of the boundary, even far back in the tail. The PEB fit is done assuming that the boundary has the same shape as the MPB on the dayside.

The location of the BS at this time differs from the average location. The entire BS seems, based upon point measurements, to be compressed during these 2.5 hours even though the solar wind speed is slow and the density moderate. This may seem unexpected since an increase in dynamic pressure should cause the boundary to be pushed farther inward.

It has been shown by *Mazelle et al.* (2004) and *Edberg et al.* (2008) that the dayside BS is on average closer over the northern hemisphere of Mars than it is over the southern hemisphere by about $0.4 R_M$, presumably due to the influence of the crustal magnetic field. This is in agreement with the location of the inbound Rosetta BS crossing and the outbound MEX BS crossing, which are both observed in the northern hemisphere. The inbound MEX BS crossing, which is observed in the southern hemisphere, is still closer in than average but is the most distant crossing of these three. It is however only about $0.2 R_M$ farther out than the other two, if extrapolated to the terminator plane. The crossing by Rosetta far down tail is also located farther in than average but is observed close to the orbital plane of Mars and at a large distance in the y -direction.

The location of the MPB is found close to its average position at all times during the Rosetta flyby which indicates that it is not governed by the same factors (such as solar wind dynamic pressure and IMF orientation) as the BS, or at least does not move on the same timescales when a change of these factors occur, considering that the BS is compressed during the entire flyby interval.

4.4 Simultaneous observations during high pressure solar wind

Rosetta only stayed within the Martian plasma environment for a couple of hours when it could perform simultaneous in situ measurements together with MEX, which we have focused on in the previous Sections. However, the plasma instruments on Rosetta were switched on for 5 days around the time of the flyby, which enabled further possibilities in terms of two-spacecraft studies at Mars. In the following Sections we will present a study where we use Rosetta as a solar wind monitor while MEX samples the Martian plasma environment in order to study the influence of high solar wind dynamic pressure on the plasma boundaries around Mars.

The orbit geometry of MEX and Rosetta is shown in Figure 4.6 for a longer interval during the time of the Rosetta Mars swingby. Also shown are the positions of all the MPB and BS crossings as observed by MEX from 00 UT on 24 February 2007 until 24 UT on 27 February 2007 together with empirical models of the two boundaries from *Edberg et al.* (2008) and *Trotignon et al.* (2006). The position of each crossing, which are identified in the ELS data, is adjusted to account for the mean 4° aberration of the solar wind direction caused by the orbital motion of the planet while the MEX orbit (black solid line) is not adjusted. Note that the inbound and the outbound boundary crossings occurred on almost opposite sides of the planet. MEX was at this time, as stated previously, in an elliptical 6-hour orbit very close to the terminator plane of Mars. It hence crossed the MPB and the BS both inbound and outbound on every orbit and completed 14 orbits during these four days. The local time is ~ 17 h on the inbound passes

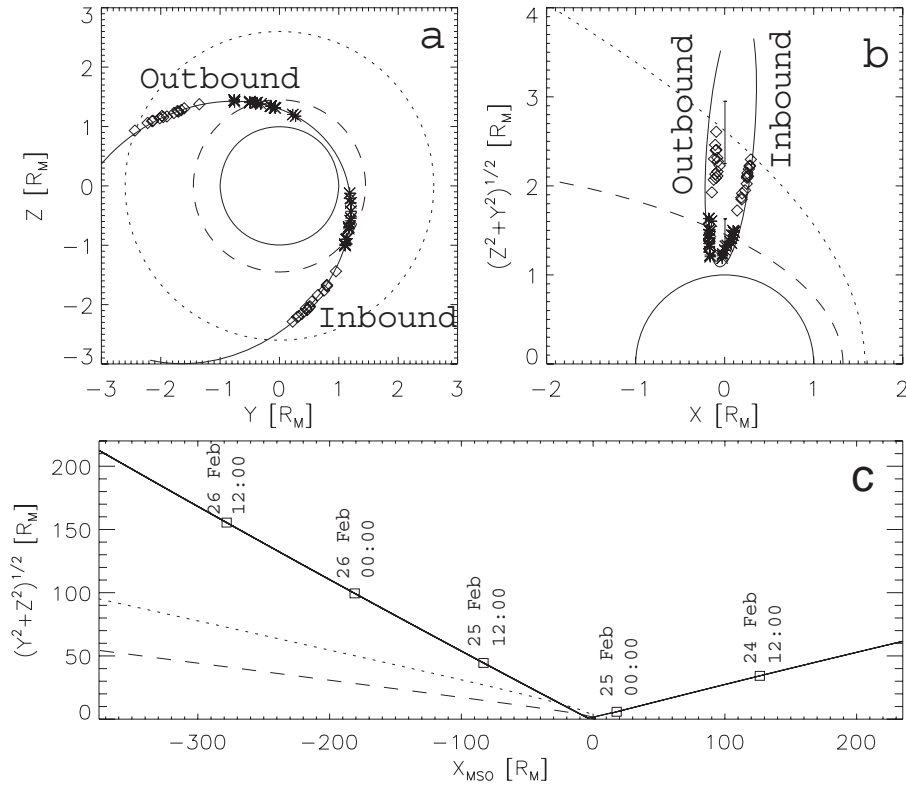


Figure 4.6: Boundary crossing locations and orbital geometry during the Rosetta Mars swingby. The top panels show all BS (diamonds) and MPB (stars) crossings observed by MEX during 24-27 February 2007, shown projected onto (a) the $y - z$ plane and (b) in cylindrical coordinates together with the average BS (dotted line) and MPB (dashed line). Panel (c) shows the trajectory of Rosetta in cylindrical coordinates (black solid line) together with best fits of the MPB (dashed line) and BS (dotted line) from Trotignon et al. (2006). A part of the MEX orbit is shown in panel (a) and (b) (black line). The vertical bars in panel (b) indicate the mean extrapolated terminator distance and standard deviation of the BS and MPB crossings from Edberg et al. (2008). The positions of the crossings are adjusted to account for the 4° aberrated solar wind flow caused by the orbital motion of the planet with respect to an average solar wind speed of 400 km s^{-1} .

and ~ 05 h on the outbound passes. In panel (c) we show the trajectory of Rosetta, which had its CA to Mars at 01:58 UT on 25 February 2007 and then proceeded out through the magnetosheath on the nightside, crossed the BS outbound at 04:04 UT and continued downstream in the solar wind.

4.4.1 Plasma boundary asymmetries

A plot of combined Rosetta and MEX measurements from the time around the Rosetta Mars swingby is shown in Figure 4.7. The data gap around CA as well as the BS crossing by Rosetta during its outbound leg are indicated in the Figure. Also indicated is a region of high solar wind pressure (yellow field), which will be detailed in the following Section and zoomed in on in Figure 4.8, as well as three intervals which we will be studied in more detail in Figure 4.11.

During the time after the CA of Rosetta, a high pressure solar wind region was observed by both MEX and Rosetta as indicated by the yellow field in Figure 4.7. This can be seen in more detail in Figure 4.8 where we show a time series of Rosetta IES/LAP/MAG and MEX ELS/IMA data for the two day interval around the time of CA of Rosetta, starting at 00 UT on 25 February and lasting to 24 UT on 26 February 2007. The Rosetta LAP probe-to-spacecraft potential V_{ps} can, as described earlier, be used as a proxy for the plasma density for time periods when the spacecraft attitude (i.e. the SAA angle) is constant. The SAA is important for determining the pointing of IES and also for the location of the LAP instrument in the potential field of Rosetta. An IES mode change at 05:00 UT on 25 February caused electrons below 500 eV not to be sampled afterward. An unfavorable spacecraft attitude also affected the IES measurements with lower fluxes as

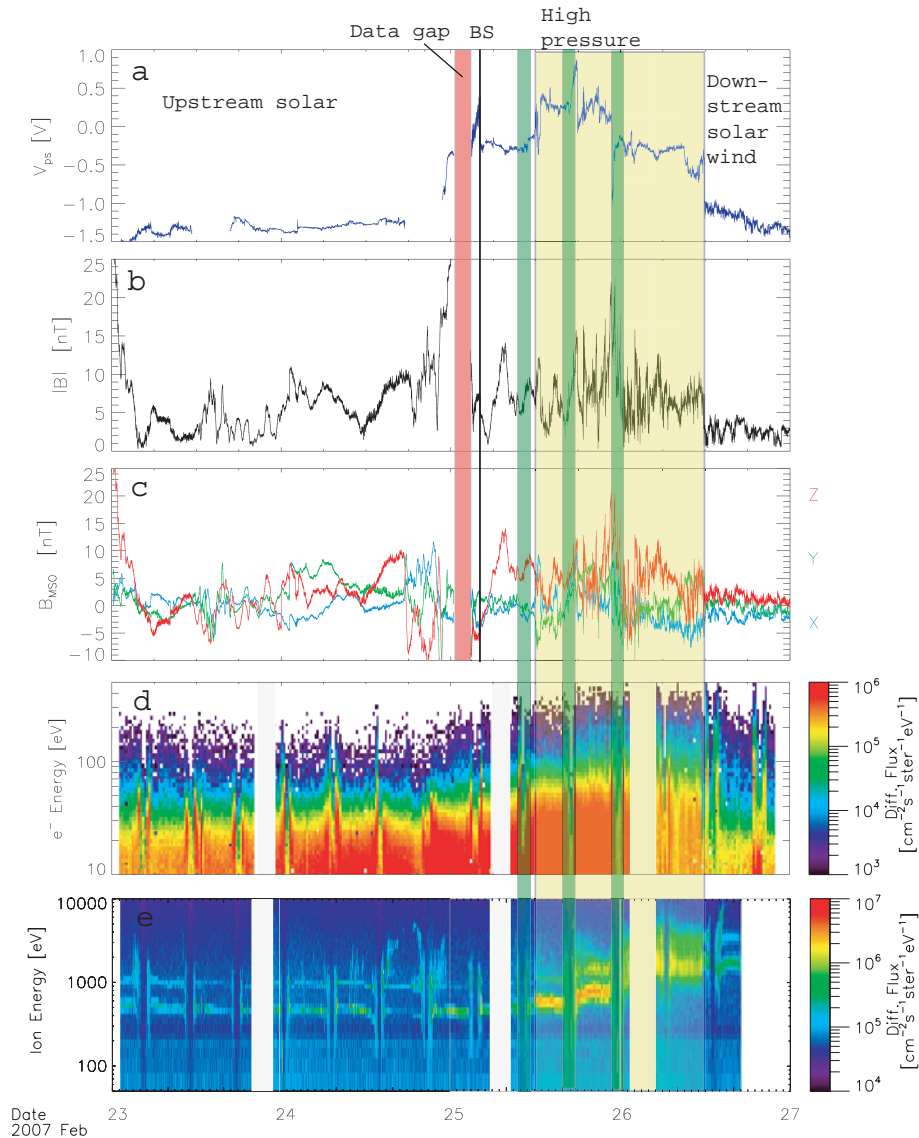


Figure 4.7: Overview of the data which will be analyzed in the next Sections of this Chapter. The plot shows a time series of (a) Rosetta LAP probe-to-spacecraft potential V_{ps} , Rosetta MAG (b) magnetic field magnitude and (c) components in MSO coordinates, (d) MEX ELS omni-directional electron energy spectra and (e) MEX IMA omni-directional ion energy spectra. The yellow interval marks a region of high solar wind pressure, which will be detailed in Figure 4.8, and the three green intervals will be studied in more detail in Figure 4.11. The data gap around CA of Rosetta is marked in red and the outbound BS crossing is marked by a black line.

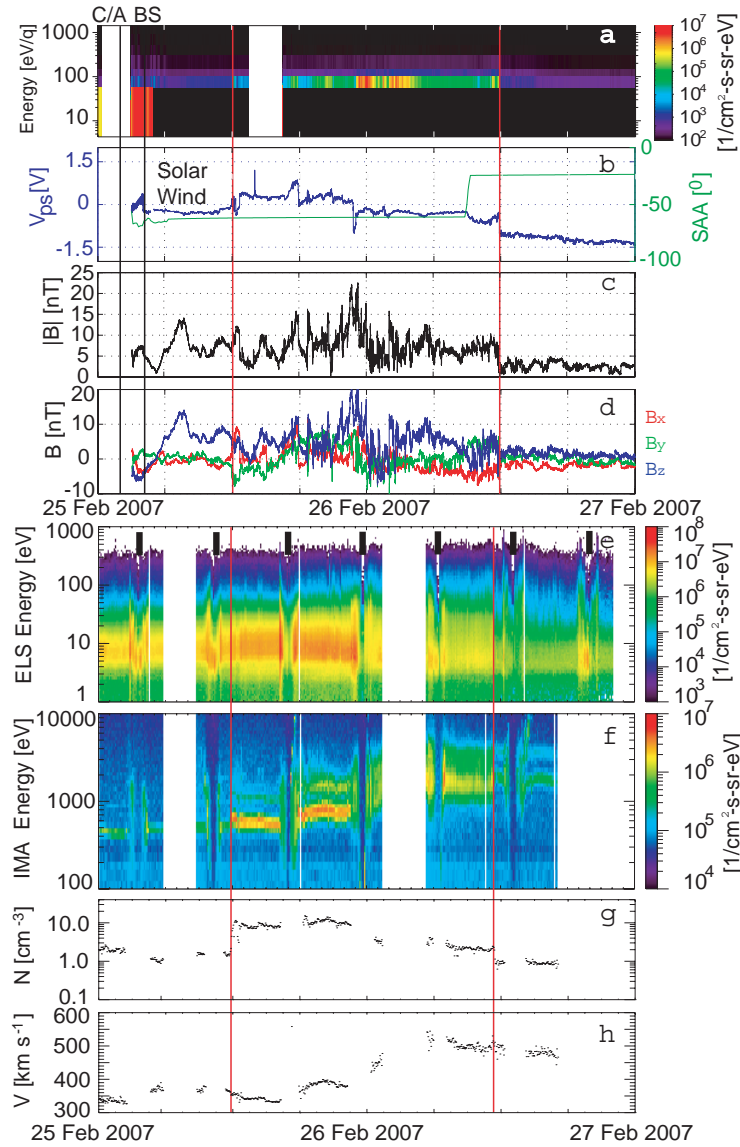


Figure 4.8: Time series of (a) Rosetta IES omni-directional electron spectra, (b) Rosetta LAP probe-to-spacecraft potential V_{ps} measured at a rate of 0.9 Hz (blue) and Rosetta SAA (green), Rosetta MAG (c) magnetic field magnitude and (d) components in MSO coordinates, (e) MEX ELS omni-directional electron energy spectra, (f) MEX IMA omni-directional ion energy spectra as well as (g) MEX IMA ion density and (h) total velocity. The interval of high pressure is marked by red lines, while the CA of Rosetta and the outbound BS crossing are marked by black lines. The thick bars in panel (e) mark the CA of MEX during each orbit.

a result.

In Figure 4.8, at 11:49 UT on 25 February 2007 as indicated by the left red vertical line, IMA onboard MEX observed a sudden solar wind density increase from $\sim 1 \text{ cm}^{-3}$ to a maximum of $\sim 10 \text{ cm}^{-3}$. The MEX ELS instrument also observed an increase in electron fluxes at the same time. This was followed by a gradual increase in velocity from $\sim 350 \text{ km s}^{-1}$ to a maximum of $\sim 500 \text{ km s}^{-1}$. For details regarding the moment calculation from IMA, see Section 2.4 and *Fränz et al.* (2006a). At 12:02 UT on 25 February 2007 the IES, LAP and MAG on Rosetta observed an increase in electron flux in the energy range 60–100 eV, a sharp increase in V_{ps} , and an increase in magnetic field variability, respectively. Rosetta was downstream of Mars at a distance of $83 R_M$ at this time. The spatial difference between where Rosetta starts to observe the high pressure solar wind and where MEX observes it divided by the difference in arrival times at the two spacecraft gives a velocity in the MSO $-x$ -direction of $\sim 360 \text{ km s}^{-1}$ ($83 R_M$ divided by 13 min).

The density increase observed by MEX lasted until 11:22 UT on 26 February 2007, indicated by the right red vertical line, while the higher velocity lasted longer, at least until a data gap started on 28 February 2007. At Rosetta, V_{ps} dropped suddenly (corresponding to a decrease in plasma density) at the same time as the magnetic field variability signatures stopped and the electron fluxes decreased at 11:53 UT on 26 February 2007 at a distance of $277 R_M$ downstream of Mars. The difference in time between these signatures in the data of the two spacecraft give a velocity in the MSO $-x$ -direction of $\sim 510 \text{ km s}^{-1}$. The solar wind velocity measured by MEX IMA agrees very well with the velocities derived from arrival times of similar features at the two spacecraft ($\sim 350 \text{ km s}^{-1}$ compared to $\sim 360 \text{ km s}^{-1}$ and

$\sim 510 \text{ km s}^{-1}$ compared to $\sim 500 \text{ km s}^{-1}$). The velocity does not change across the boundaries between regions of high and low pressure regions, as would be expected from interplanetary shocks or corotating interaction regions, and they rather resemble convected structures propagating outward in the solar system. This observed high pressure solar wind region and its effect on the Martian plasma environment is the topic for the rest of this Chapter.

To illustrate how the BS and MPB respond to the high pressure solar wind region, we plot their altitudes as a time series together with the MEX and Rosetta measurements in Figure 4.9. The time series shows four days of combined Rosetta and MEX measurements starting at 00 UT on 24 February 2007. In panel (a) we show solar wind dynamic pressure derived from MEX IMA and in panel (b) the Alfvénic Mach number M_A based on a combination of the magnetic field strength from Rosetta MAG, time-shifted to the time frame of MEX assuming a constant solar wind velocity of 350 km s^{-1} , and the solar wind plasma density from MEX IMA. Panel (c) shows the angle θ_{Bn} between the IMF, as measured by Rosetta and time-shifted to the time frame of MEX, and the local normal to the BS, for each inbound (squares) and outbound (triangles) BS crossing by MEX. The local normal to the BS was calculated from the statistical best fit shape of the BS from *Edberg et al.* (2008) at the point closest to the observed BS crossing. Inbound and outbound crossing data are displayed as squares and triangles, respectively, throughout the Chapter. Panel (d) shows the distance of each BS crossing from the center of the planet, for inbound and outbound crossings separately and panel (e) shows the distance of the MPB crossings.

The inbound crossings occur at lower solar SZA than the outbound ones and should therefore be at lower distances but this is evidently not always

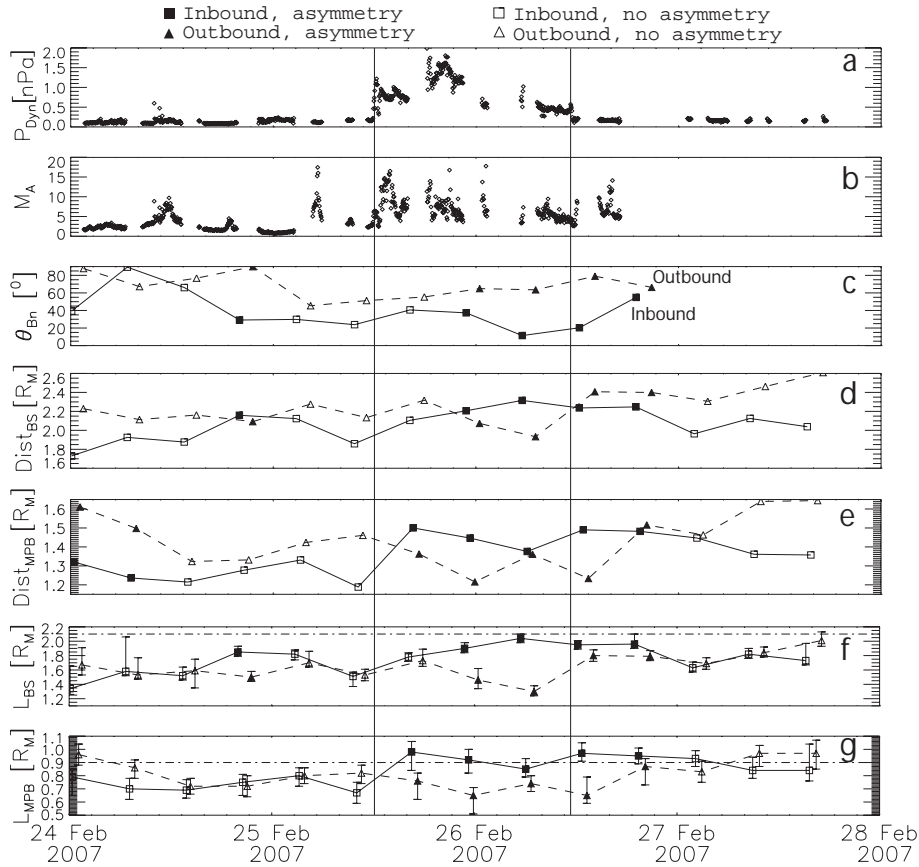


Figure 4.9: Time series of (a) the MEX IMA dynamic pressure, (b) Rosetta MAG/MEX IMA Alfvénic Mach number, (c) θ_{Bn} , distance of each (d) BS and (e) MPB from the center of the planet as well as L-value of each (f) BS and (g) MPB together with error bars. Inbound θ_{Bn} , distances and L-values are displayed as squares and connected by solid lines while the outbound ones are displayed as triangles and connected by dashed lines. Filled symbols indicate that there is an asymmetry present between the inbound and outbound boundaries. The values of L from Edberg *et al.* (2008) are indicated by dash-dotted lines in panels (f) and (g). The black vertical lines mark the interval of the high pressure solar wind.

the case. The inbound crossings are sometimes at larger distances than the outbound crossing during the same orbit. Hence the boundaries are asymmetric in their shapes. In order to properly compare the distances of inbound crossings with the distance of the outbound crossings, which occur at different SZAs, we need a measure of their distances which is independent of the SZA at which they occur. Panel (f) therefore shows the value of the semi-latus rectum L from fits of conic sections to each single BS crossing. The fits are done in the same way as described in *Crider et al.* (2002), where the values of ϵ and X_0 (from (*Edberg et al.*, 2008)) are fixed, and only L is varied. L is hence a linear measure of the distance of a crossing for which the SZA dependence has been removed. Panel (g) shows the same as panel (f) but for the MPB instead of the BS. Due to the orbit configuration, upstream waves and also the movement of the boundaries, the two boundaries do not always appear as sharp boundaries but are at times more or less smeared out in a time series. This gives an uncertainty to where the boundary crossings actually occur. The uncertainty bars in panel (f) and (g) represent where the spacecraft is well within/without the BS and the MPB, as seen in a time series of data, and hence are estimates of the thicknesses of the boundaries, or their variability in position during each crossing.

The position of each crossing is adjusted to account for the 4° aberration caused by the planets orbital velocity. The average values of L for the BS and MPB from *Edberg et al.* (2008) are shown for reference purposes by the horizontal dash-dotted lines in panel (d) and (e). The inbound and outbound crossings of both the BS and the MPB are at approximately similar altitudes (L-values) up until the high pressure solar wind appears. They are also closer than average to the planet in the time interval preceding the high pressure

solar wind. During and after the high pressure solar wind the altitude of the inbound and outbound crossings deviate significantly from each other, by up to $0.7 R_M$ for the BS and $0.4 R_M$ for the MPB and hence properly indicate that both boundaries have become asymmetric. The inbound boundaries move outward first and the outbound boundaries follow later on.

The asymmetry of the MPB starts during the same orbit as the high pressure solar wind feature is observed and the BS asymmetry starts during the following orbit. The shape asymmetry lasts until about two orbits after the solar wind feature has passed. As reported by *Pérez-de-Tejada et al. (2009)*, the exosphere of Mars, as seen in X-ray images from the XMM/Newton satellite, is also very asymmetric during this interval. The X-ray emissions from the exosphere are more intense over the poles and also indicate that the exosphere over the poles is tilted in an anti-sunward direction. Note also that there is a short-lived BS asymmetry during the last orbit on 24 February 2007. Throughout this Chapter, filled symbols indicate that there is an asymmetry present between the inbound and outbound crossings.

4.4.2 Cause of the asymmetries

Factors that could be responsible for the asymmetry include whether the boundaries are quasi-perpendicular or quasi-parallel, the direction of the solar wind convective electric field $\mathbf{E} = -\mathbf{v} \times \mathbf{B}$ and the crustal magnetic fields.

1. The quasi-parallel (quasi-perpendicular) effect could cause increased (decreased) upstream wave activity which increases (decreases) the apparent thickness of the boundaries. This has already been accounted for to some extent by including the error bars in Figure 4.9 but it is possible that the boundaries also move outward or inward as a whole

due to this.

2. The convective electric fields determines in which way the ions move. On one side of the planet they will move into the planet and on the opposite side they will move out into the solar wind and cause increased massloading which could cause the boundaries to move outward due to the increased plasma pressure.
3. The crustal magnetic fields provide additional magnetic pressure which disturbs the pressure balance across the boundaries and would cause the boundaries to move outward. Since the crustal magnetic fields are strongest and most frequently observed at southern latitudes the boundaries should be at higher altitudes over the southern hemisphere.

In Figure 4.10 we show the results of tests of the above factors that could possibly cause the asymmetry. In panel (a) and (b) we show the value of the semi-latus rectum L from fits to each observed BS and MPB crossing, respectively, as a function of θ_{Bn} together with linear least-square fits to the inbound (solid line) and outbound (dashed line) crossings. The difference in mean value of the semi-latus rectum of all quasi-parallel ($\theta_{Bn} < 45^\circ$) and all quasi-perpendicular ($\theta_{Bn} > 45^\circ$) BS crossings (1.77 and 1.62, respectively) is statistically significant according to a Student's t-test at a 90% confidence level. However, if a Student's t-test is done separately for inbound and outbound BS crossings, then only the inbound crossings show a significant difference in mean values of L at a confidence level of 90%. An equally significant difference between mean values of the semi-latus rectum is not found for the MPB. There is a trend of a closer in boundary for higher θ_{Bn} in panel (a) and panel (b), but only for the crossings that occur when the

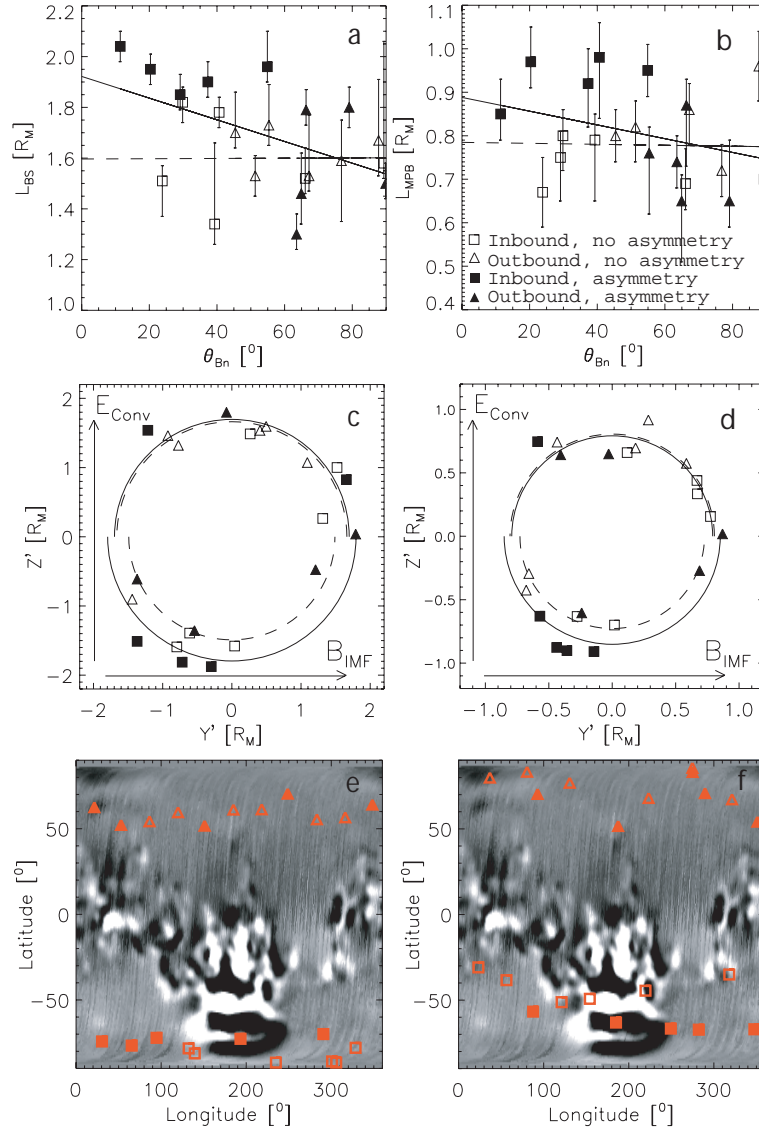


Figure 4.10: The distance displayed in terms of L -value (see text for explanation) of (a) the BS and (b) the MPB crossings as a function of θ_{Bn} with linear fits to the inbound (solid) and the outbound (open) crossings. The position (c) of all BS and (d) MPB crossings rotated into a frame where Y' is aligned with the IMF and Z' with the convection electric field. Average distances are shown for inbound (solid line) and outbound (dashed line) crossings in the $+E$ and $-E$ hemispheres in panels (c) and (d). The position (e) of all BS and (f) MPB crossings projected onto a map of the crustal magnetic field strength (the position data being coloured red in order to make them more visible).

boundary is asymmetric and not for the other crossings. This rather tells us that the crossings that occur during the asymmetric boundary interval and are on the inbound side also happen to be quasi-parallel and vice versa but not that it is the θ_{Bn} angle that determines the altitude of the boundaries.

In panel (c) and (d) of Figure 4.10 we show all BS and MPB crossings rotated into a reference frame where Y' is aligned with the instantaneous IMF direction, as measured by Rosetta MAG, and Z' with the convection electric field direction, in order to determine the effect of the convection electric field. Average distances are displayed for inbound (dashed line) and outbound (solid line) crossings in both the $+E$ -hemisphere, where the electric field is directed locally upward, and in the $-E$ hemisphere, where the electric field is directed locally downward. If asymmetric massloading occurred and was the main factor which controlled the location of the boundaries, then the boundaries in the $+E$ -hemisphere, where the ions move out into the solar wind, would be at higher altitudes than the ones in the $-E$ -hemisphere, where the ions move toward the planet. However, no such trend is observed for either the BS or the MPB, neither during high nor low pressure periods.

We do, however, observe that in the $-E$ -hemisphere the inbound crossings, in the southern/dusk hemisphere, are farther out than the outbound crossings. The difference is statistically significant according to Student's t-test at a 95% confidence level for the BS and at a 90% confidence level for the MPB. This asymmetry is not visible for the $+E$ -hemisphere. Since the evolution of the IMF orientation with distance is unknown, there could be a difference in IMF orientation between the location where Rosetta measures the magnetic field and the location where MEX measures the plasma boundaries.

In panels (e) and (f) of Figure 4.10 we show, respectively, the BS and MPB crossings projected on a map of the crustal magnetic field strength to see if the observed asymmetry is caused by the fact that some crossings occur over strong crustal fields and others not. However, the asymmetric boundary crossings occur over a wide range of longitudes and the inbound crossings, at southern latitudes, do not occur directly over the strong crustal fields, which could have caused them to move to higher altitudes by providing additional magnetic pressure. The crustal magnetic fields do not therefore seem to be responsible for causing an asymmetry in this case. In fact, neither of the factors tested in Figure 4.10 give a clear result as to whether they affect the location of the boundaries to become asymmetric or not.

4.4.3 Ion outflow and exosphere asymmetry

Figure 4.11 shows MEX measurements from three consecutive orbits beginning on 25 February 2007 which occur during equally long intervals centered at the time of the MEX CA to Mars on each pass (the intervals are marked by green fields in Figure 4.7). In panel (a), (d) and (g) of Figure 4.11 we show IMA omni-directional ion energy spectrograms of heavy planetary ions together with MEX altitude (red line), in panel (b), (e) and (h) we show ELS omni-directional electron energy spectrograms together with MARSIS measured local electron density (short black line between 30 cm^{-3} and 70 cm^{-3}) and in panel (c), (f) and (i) we show Rosetta MAG magnetic field measurements time-shifted to the time frame of MEX. The time-shifts are ~ 11 min, ~ 20 min and ~ 29 min for each orbit, respectively, if using the measured solar wind velocity of 350 km s^{-1} from Figure 4.8, panel h. If assuming a $\sim 10\%$ error on the measured velocity the error on the time-shifts

are $\pm 1 - 2$ min. There are only MARSIS density measurements during ~ 5 min on the outbound part of the first orbit, ~ 5 min during both the inbound and the outbound part of the second orbit and only ~ 5 min during the inbound part of the third orbit, but these are still important since they provide a measure of the local plasma density. IMA and ELS can also provide values of the density but do not always measure the full density, especially not the colder population, which MARSIS does.

Panels (d) and (e) of Figure 4.11 show the same data as presented by *Pérez-de-Tejada et al.* (2009) (their Figure 2). From 17:10 until 17:40 UT in panel (d) a distinct population of heavy ions (mainly CO_2^+ , O_2^+ and O^+) are seen in the energy range 100 eV - 10 keV, around the time of the outbound MPB crossing, which are interpreted as being heavy planetary ions escaping from the planet. These ions show a clear trend of increasing in energy as MEX measures them at higher and higher altitudes and they reach velocities far higher than the required escape velocity (*Pérez-de-Tejada et al.*, 2009).

Not reported by *Pérez-de-Tejada et al.* (2009) is that such escaping planetary ions are also visible on the following orbit, in almost exactly the same location but with an order of magnitude less intensity. These are seen in panel (g) from 23:55 UT on 25 February until 00:15 UT on 26 February, again as a distinct population which gain in energy, from 100 eV up to 1 keV, while MEX measures them at higher altitude. The population of escaping ions during this orbit is now harder to distinguish from the background measurements but still visible.

It is during these two orbits, when escaping planetary ions are observed, that the solar wind pressure increases to high values of $\sim 1.0-1.5$ nPa as can be seen in panel (a) of Figure 4.9. The magnetic field measurements

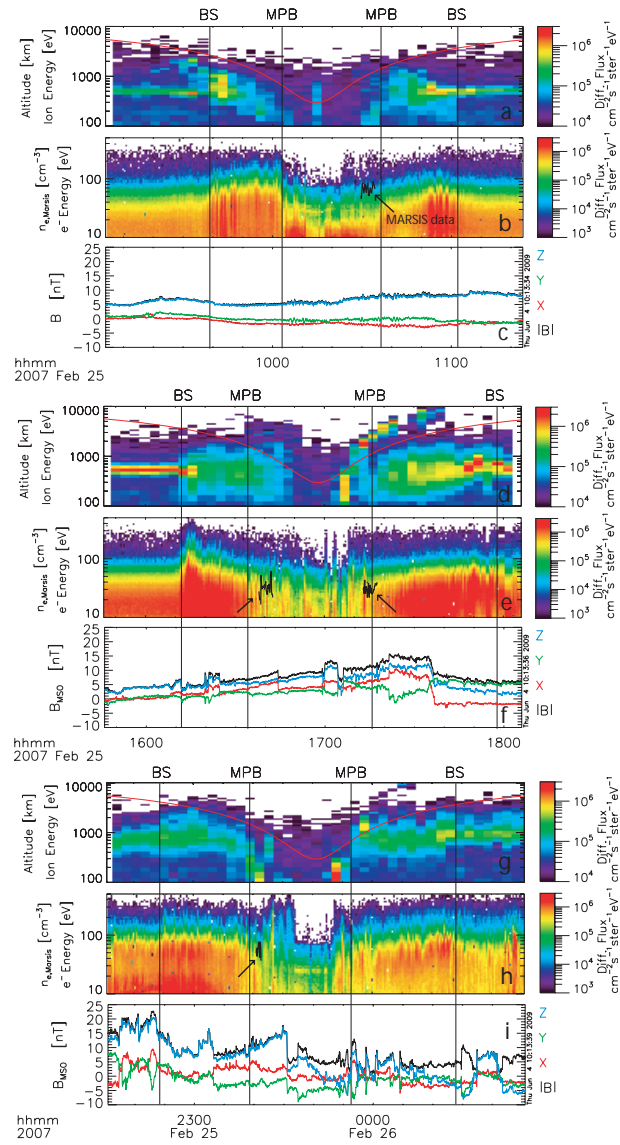


Figure 4.11: Time series of MEX and Rosetta measurements. The panels show (a, d and g) MEX heavy planetary ion omni-directional spectrograms, (b, e and h) MEX electron omni-directional spectrograms and (c, f and i) Rosetta magnetic field measurements during three consecutive MEX orbits. The downstream Rosetta measurements are time-shifted to the time frame of MEX. The altitude of MEX is superposed on the ion spectrograms (red line, same scale as for the ion energy) and the local electron density from MARSIS is superposed on the electron spectrograms (short black line, same scale as for the electron density). The MARSIS data is only available during ~ 5 min on each orbit and pointed out by black arrows. The time of the BS and MPB crossings by MEX are shown as vertical black lines.

show that the IMF was mainly northward during these orbits which gives a convective electric field direction mainly in the MSO $-y$ -direction. The convective electric field is in the same direction, roughly, as MEX moves in when the escaping planetary ions are observed (see MEX trajectory in Figure 4.6, panel (a)). As the ions are observed to gain in energy we can conclude that they are accelerated by the convective electric field. At the same time as the magnetic field changes its orientation at 17:40 UT (Fig. 4.11, panel (d)) the escaping ions cease being observed in the ion spectrogram. *Pérez-de-Tejada et al.* (2009) also noted this sharp drop but suggested that it was caused by momentum transport between the planetary ions and the solar wind ions. But with the magnetic field measurements from Rosetta we now suggest that the sharp drop is caused by a change of direction of the convection electric field, rotating from $-y$ to $+z$, such that the outflowing ions start to move northward while MEX moves farther westward and ceases to observe the outflowing ions. During the second orbit when these ions are observed, the IMF direction is still mainly northward but more variable which could explain why the measured flux rates are lower than during the previous orbit.

The local electron densities measured by MARSIS just inside the MPB on the first orbit in Figure 4.11, panel (b), are $\sim 70 \text{ cm}^{-3}$. During the following orbit, in panel (e), at the same altitudes on the outbound pass as in the previous orbit, the density had dropped to values of $\sim 30 \text{ cm}^{-3}$. Also during the inbound pass of the second orbit the densities, at approximately the same altitudes, vary around 30 cm^{-3} . During the third orbit, on the inbound leg in panel (h), the average density had increased to around 70 cm^{-3} again. These limited measurements from MARSIS indicate, in the same way as shown by

Dubinin et al. (2009) but for a different interval, that the ionospheric densities inside the MPB decreased when the high pressure solar wind impacted Mars and therefore the ionosphere was being scavenged as a result.

As shown in Figure 4.9, the boundaries start to become asymmetric during this interval. This can be clearly seen in Figure 4.11 as well. The inbound BS moves to increasingly higher altitudes during the three orbits shown, from an L-value of $1.51 R_M$ to $1.78 R_M$ to $1.90 R_M$, even though the dynamic pressure increases and should push the boundary closer in. The inbound MPB follows the same trend roughly, or at least within the error bars, and moves from an L-value of $0.70 R_M$ to $0.98 R_M$ to $0.92 R_M$. The outbound MPB does, however, move inward during these three orbits, from $0.82 R_M$ to $0.76 R_M$ to $0.65 R_M$. The outbound BS first moves outward, from $1.53 R_M$ to $1.73 R_M$ like the inbound BS, but only to move inward again during the third orbit to $1.46 R_M$, when the solar wind dynamic pressure decreases. These data clearly show that the dynamic pressure is not always the only important factor in determining the location of the plasma boundaries.

4.5 Boundary asymmetry linked to the ionospheric outflow

Below, we try to explain the observations of the asymmetric boundaries by discussing the various factors involved. According to Figure 4.10, panel (a) and (b), the BS and MPB asymmetries are generally only present when the inbound crossings are quasi-parallel and the outbound crossings are quasi-perpendicular. We cannot, however, conclude that the effect of the difference between quasi-parallel and quasi-perpendicular crossings is the only reason

for the asymmetry. We can only conclude that when there is an asymmetry present, the inbound and outbound crossings have significantly different values of θ_{Bn} . Other factors could still be important.

In Figure 4.10, panel (c) and (d), we have shown that asymmetric mass-loading is not the single responsible factor for causing the boundary asymmetries. The boundary crossings that occur in the $+E$ -hemisphere are not at higher altitudes than the crossings observed in the $-E$ -hemisphere, on average. We do, however, note that the boundaries in the southern and northern hemispheres of Mars react differently to different directions of the convection electric field, possibly due to the presence of the southern crustal fields or, alternatively, due to whether the boundaries are quasi-perpendicular or quasi-parallel.

In Figure 4.10, panels (e) and (f), we do not find a direct correlation between the crustal field strength at the exact position of the BS/MPB crossings and the boundary distances. However, it is in the southern hemisphere that the boundaries are at higher altitudes but since the MEX crossings occur at a range of longitudes it would imply a global influence of the crustal fields, if they are indeed responsible.

The Alfvénic Mach number and dynamic pressure variation do not directly explain the asymmetry, either. These quantities could possibly vary in resonance with the boundary sampling rate, which is unlikely and indeed not the case here since the solar wind parameters do not vary with the same frequency as the boundaries move up and down. A comparison between the altitudes of all crossings and the solar wind dynamic pressure and Alfvénic Mach number reveals no obvious trend for the set of crossings in this interval.

Since none of the above factors have been clearly shown to be the single

main factor that causes the asymmetry we suggest that the high pressure solar wind and the ion outflow are also connected to the observed asymmetries. The ion outflow can disturb the normal balance between factors that would be expected to control the location of the boundaries, i.e. the solar wind dynamic pressure, the IMF direction, the plasma pressure, magnetic pressure and the crustal fields and we can therefore only provide a suggestion for a possible explanation to the observations. The MPB and BS in the southern hemisphere, quite counter-intuitively, move outward when the high pressure solar wind reaches Mars as can be seen in Figure 4.11 and which we try to illustrate by the sketch in Figure 4.12. We interpret the outward moving of the boundaries as the plasma pressure and/or magnetic pressure inside the MPB and BS are significantly increasing during the high pressure solar wind and more so than the solar wind dynamic pressure, resulting in an outward motion of the boundaries. The pressure on the inside could increase due to an increased massloading over a longer time period on that side of the planet in combination with increased massloading over the crustal fields on the other side, and possibly as an effect of plasma heating through reconnection events when the varying IMF direction reaches the crustal fields.

The convective electric field is directed toward the planet in the southern/dusk hemisphere and the ions consequently move in that direction. In the opposite northern/dawn hemisphere the convective electric field is directed away from the planet and the ions can escape the planet and the plasma pressure on the inside of the MPB and BS decreases, which leads to an eventual inward motion of the plasma boundaries. The BS during the outbound part of the orbit immediately after the high pressure region has reached Mars does, however, initially move outward, which could be an effect

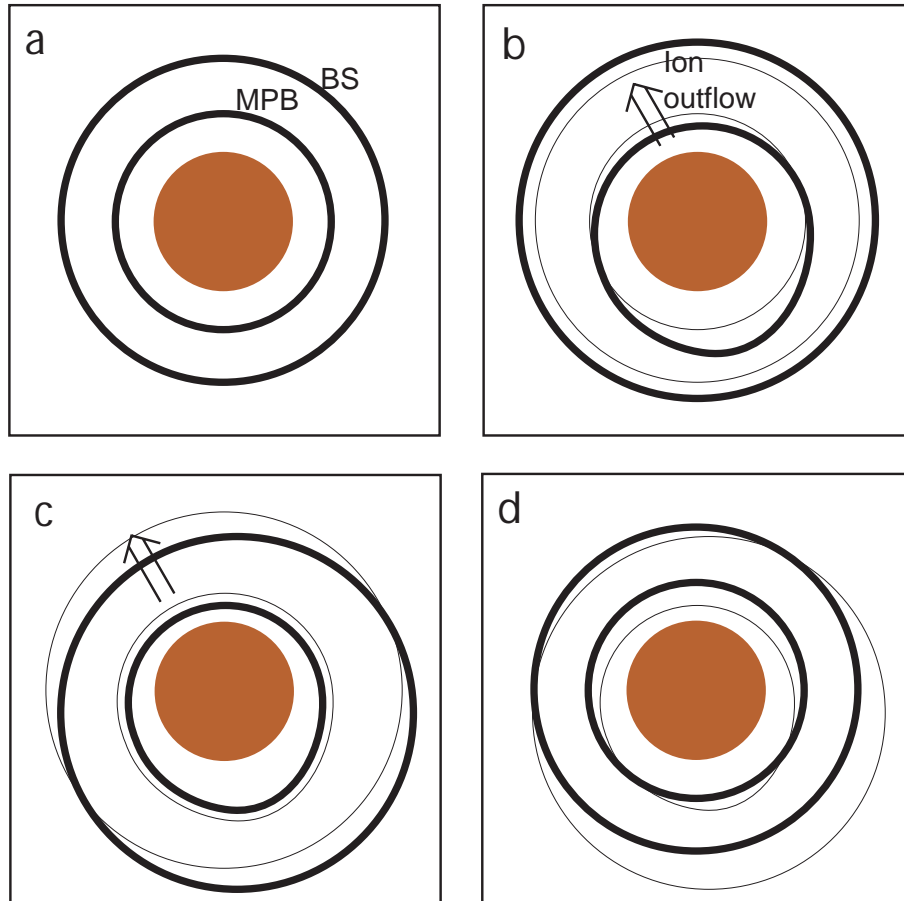


Figure 4.12: Sketch of the position of the plasma boundaries in the terminator plane as seen from the Sun. In each panel are the boundaries at one specific time in the time history of the boundary positions illustrated. The movement resulting from the encounter of the high pressure solar wind as observed during the last three orbits on 25 February 2007 and when the high pressure solar wind region had passed. The thick black solid lines represent the BS and MPB, while the thin black lines in each panel represent the BS and MPB as they were in the previous panel. The boundaries go from being symmetric in panel (a) to asymmetric in panels (b) and (c) when ion outflow is observed, to finally become symmetric again in panel (d) when the high pressure solar wind has passed.

of massloading of the solar wind by the outflowing planetary ions. The BS therefore first moves outward but after the ionosphere has eroded during the time of at least one orbit the pressure on the inside of the BS has decreased so much that the boundaries then can move inward on that side of the planet and the boundary become asymmetric. When the high pressure region has passed the boundaries become symmetric again.

4.6 Summary and conclusions

The Rosetta flyby adds to the growing number of spacecraft that have sampled the Martian plasma environment. We have performed a rigorous analysis of the simultaneous measurements performed by the Rosetta instruments and the MEX measurements during the time of the Rosetta Mars flyby in February 2007. First, we have analyzed the measurements around the time of CA of Rosetta when both Rosetta and MEX sampled the plasma boundaries. Secondly, we have analyzed the measurements when Rosetta acted as a solar wind monitor and MEX sampled the plasma boundaries alone.

When both spacecraft sampled the plasma environment simultaneously we could perform the first near-simultaneous two-spacecraft study of the shape and location of the BS, MPB and PEB. At this time, the solar wind appeared to be quiet and slow and so the global plasma environment could be assumed to be more or less steady. The shape of the plasma boundaries were, for the first time, experimentally compared to previous models (Figure 4.5). The far downstream triple BS crossings observed by Rosetta at approximately 04:04 UT are also the most distant BS crossings ever observed at Mars: at $\sim 18 R_M$ behind the planet.

The BS is generally found to be located closer to the planet than average compared to what models would suggest for all crossings in this time interval, even though the upstream solar wind speed is low and the density and IMF are moderate. For two of the BS crossings (the inbound Rosetta crossing and the outbound MEX crossing), this can be explained by the fact that they are observed over the northern hemisphere of Mars where the BS has been observed to be closer to the planet. The inbound MEX BS crossing is observed over the southern hemisphere and is the crossing observed the farthest out. Another explanation could be that the thermal plasma pressure in the magnetosheath is lower than average at this time, and the effective solar wind obstacle thereby smaller, which puts the BS closer in than average. The shape of the BS is still reasonably well represented by a conic section. The MPB is observed very close to its average position and also seems to be well represented by a conic section in its shape.

The PEB crossings observed seems to form the same shape as the MPB on the dayside. However, the crossings of this boundary takes place very distant in time and close in space which makes it hard to determine the shape accurately and we have not put any focus on the shape of the PEB in this Chapter.

When Rosetta acted as a solar wind monitor, both Rosetta and MEX show measurements of a high pressure (dynamic, magnetic and thermal, as can be inferred from Figure 4.8) solar wind region that passed by Mars during a 24 hour interval. At the same time as the high pressure solar wind passed by, the Martian plasma boundaries as well as the exosphere are found to become asymmetric in shape. Also, an outflow of planetary ions was observed over the northern polar region of Mars in the same interval. During 4-5

orbits following the impact of the high pressure solar wind region, the BS and MPB as observed inbound by MEX, in the southern/dusk hemisphere, were much farther out than the BS and MPB observed outbound, in the northern/dawn hemisphere. As reported by *Dubinin et al. (2009)* and *Nilsson et al. (2009)* the ion outflow from Mars increases during high pressure solar wind and this has also been confirmed by models, see e.g. (*Kaneda et al., 2009*). Planetary ion outflow was, in fact, also remotely observed to occur during the time of the Rosetta swingby (*Pérez-de-Tejada et al., 2009*). In this Chapter, we have combined these results and further strengthened the evidence that high pressure solar wind causes an increase of planetary ion outflow from Mars. The high pressure solar wind, observed by MAG and LAP on Rosetta and IMA and ELS on MEX, penetrated down to the ionosphere and eroded it, as observed by MARSIS on MEX, and planetary plasma was observed to escape from the planet, as observed by IMA on MEX. The solar wind plasma could also penetrate down to the ionosphere more easily during this interval since both the BS and MPB were generally located closer in than average on the orbits preceding the high pressure solar wind. The escaping ions, as observed by MEX, gained in energy in the direction, as indicated by Rosetta MAG measurements, of the convective electric field. The exosphere was extended over both poles and the ion outflow was observed over the northern hemisphere (*Pérez-de-Tejada et al., 2009*). There have been a number studies modelling the outflow of planetary ions from Mars, see e.g. *Böswetter et al. (2004)*; *Modolo et al. (2006)*; *Kallio et al. (2008)*, which also show that an increased solar wind dynamic pressure compresses the plasma environment to some degree. However, little modelling has been done in terms of asymmetric outflow and how that would cause the plasma

boundaries to become asymmetric. *Kallio and Janhunen* (2002) did however show that both the MPB and the outflow is asymmetric and takes place mainly in one hemisphere, which was determined by the direction of the convective electric field.

In summary, the boundaries are well represented by conic sections, as determined by near-simultaneous measurements. We conclude that the high pressure solar wind enables the increased erosion of the ionosphere of Mars at this time. At the same time as the high pressure solar wind impacts on Mars are the boundaries observed to become asymmetric in their shapes. We suggest that since no clear factor has emerged that causes the asymmetry, it is possible that the observed outflow also disturbs the equilibrium pressure balance and significantly influences the location and shape of the plasma boundaries.

Chapter 5

Mars Express and Mars Global Surveyor measurements

In this Chapter we use MEX and MGS simultaneous and non-simultaneous measurements to study the Martian plasma environment. In particular, we derive quantitative expressions for the altitude of the terminator BS and MPB as functions of solar wind dynamic pressure, crustal magnetic fields and solar EUV flux. We also study the influence of the IMF direction. Some of the material presented in this Chapter is included in *Edberg et al. (2009b)*.

5.1 Introduction

MGS and MEX form a unique pair of spacecraft that have made simultaneous and continuous measurements of the Martian plasma environment. MGS arrived at Mars in 1997 and performed measurements until late 2006, while MEX arrived in late 2003 and is still gathering data as of 2009. Hence the two spacecraft obtained almost three years of simultaneous measurements. There have been many missions to Mars in the past equipped with plasma instru-

ments which have individually studied Mars, but these spacecraft are the only two that have been in orbit at the same time, thus enabling two-spacecraft studies. In this Chapter we will present results from case studies as well as statistical studies of simultaneous and non-simultaneous two-spacecraft measurements of the solar wind interaction with Mars. The aims of this study are to determine what effect the solar wind dynamic pressure, the IMF direction, the solar EUV flux and the crustal magnetic fields have on the location of the BS and MPB and to determine their relative importance.

5.2 Measurements of and proxies for the dynamic pressure, IMF direction and solar EUV flux

In order to statistically determine the effects of the above factors (dynamic pressure, IMF direction and EUV flux) we will use direct measurements as well as proxies for them. *Crider et al.* (2003) and *Brain et al.* (2005) have developed proxies for both the solar wind dynamic pressure and the IMF direction from MGS/MAG measurements. The proxies have been formulated in terms of measurements of the average magnetic field strength and draping azimuth (direction of the field) at 400 km altitude at latitudes between $50^{\circ}N$ and $60^{\circ}N$ where the crustal magnetic fields are weak. The magnetic field strength in the MPR is assumed to balance, and therefore be a proxy for, the solar wind dynamic pressure. The magnetic field draping azimuth is assumed to be roughly the same as the clock angle of the IMF and is defined to be 0° when the field is directed locally eastward and 90° when locally

northward. The pressure proxy is given by the magnetic field strength B_{proxy} which can be converted to magnetic pressure $P_B = \frac{B_{proxy}^2}{2\mu_0}$.

A solar EUV flux proxy has also been developed and is determined from the F10.7 radio flux at 2-200 nm measurements at Earth extrapolated to Mars. The technique has been used by *Mitchell et al.* (2001) and here we use the proxy developed in that study.

The solar wind (proton) velocity v and density n moments can be calculated from MEX/IMA measurements outside of the BS which is a more direct measurement of the solar wind dynamic pressure $P_{dyn} = m_p n v^2$, where m_p is the proton mass. Proton velocity and density moments are calculated from the nominal proton line in the IMA spectrogram for energies above 1 keV, and below that energy from a signal caused by protons scattered inside the IMA sensor. For details regarding the moment calculations, see Section 2.4 and *Fränz et al.* (2006a). The pressure determined from MEX that we will use in this Chapter is calculated as a mean over 10 min of measurements exterior to a BS crossing.

The time resolution of both the MGS proxies are normally 2 hours (one value per orbit) whereas the time resolution of the dynamic pressure measured by MEX is normally 2 samples per 6 hours (one value inbound and one value outbound) and the time resolution of the EUV flux proxy is 1 to 2 hour.

In Figure 5.1 we show a comparison between the MGS proxy for the solar wind dynamic pressure and the measured solar wind dynamic pressure from MEX. In panel (a) the MGS pressure proxy values are interpolated to the time of the MEX measured values and only data points during the overlapping mission time are included. There is a visible linear trend in the

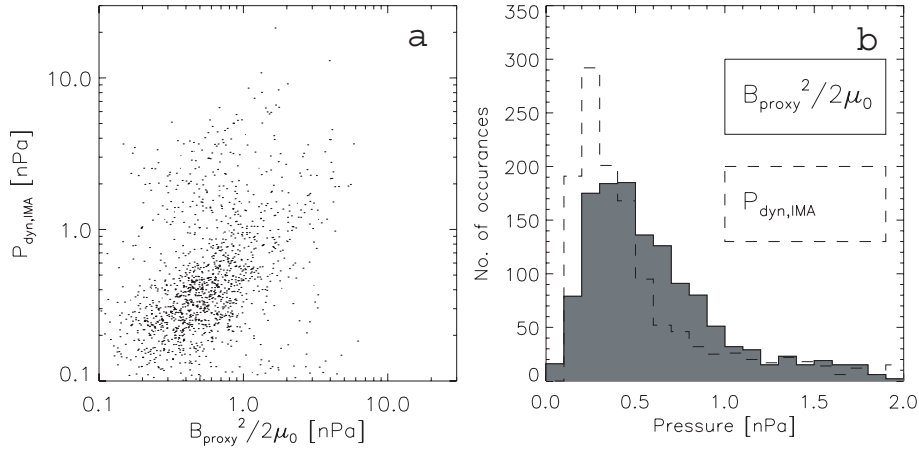


Figure 5.1: (a) Measured solar wind dynamic pressure from MEX/IMA plotted vs. the MGS proxy for solar wind dynamic pressure and (b) distributions of the MGS proxy and the measured dynamic pressure from MEX/IMA.

plot which indicates that the proxy is in reasonably good agreement with the measured values. However, there also seems to be a smaller population with high measured values from MEX while the MGS proxy shows low values, which could be explained by the fact that not every high dynamic pressure event reaches down to MGS. The distributions of the measured values and the proxy values in panel (b) are similar but with slightly different mean values. The mean of all pressure proxy values is 0.74 nPa while the mean of the measured MEX/IMA pressure values over all 10 min intervals exterior to BS crossings during the entire overlapping mission is 0.80 nPa. The difference is not unexpected since we compare measurements with a proxy and they both have inherent uncertainties.

5.3 Mars Express and Mars Global Surveyor observations

Since MEX is in a highly elliptical orbit with a low altitude periapsis it usually crosses both the MPB and the BS both inbound and outbound once every orbit. The BS is, however, not always observed since the orbit of MEX is precessing and therefore MEX stays inside the BS during the entire orbit in some seasons. The BS is observed inbound as a sudden increase in fluxes of both electrons and ions in the ELS and IMA data sets. The MPB is observed inbound as a sudden decrease of magnetosheath electron and ion fluxes (examples of which will be presented in Figures 5.3-5.5 below). The higher time resolution of ELS makes it easier to identify the exact location of the boundaries from that data set. The variability of the boundaries in combination with unfavorable orbit geometry makes it hard to identify the exact boundary location for many of the orbits and many crossings are therefore excluded. However, we have analyzed the entire set of MEX/ELS and MEX/IMA data from 2004 until 2009 and have identified 5014 MPB crossings and 3277 BS crossings. The number of crossings during the overlapping mission time between MGS and MEX (Feb 2004 - Nov 2006) decreases to 2500 and 1840, respectively, which is still twice as many as MGS observed from 1997 until 1999 when MGS was in an elliptic orbit similar to the orbit of MEX (*Vignes et al.*, 2002; *Trotignon et al.*, 2006; *Edberg et al.*, 2008). It should be noted that we can only get values of the measured solar wind dynamic pressure when the BS is crossed, meaning that we do not know the upstream pressure for all the 5014 MPB crossings.

During the overlapping mission time, MGS orbited Mars at 400 km, well

within the average MPB location and does not normally cross it. However, the variability of the magnetosheath is large and *Brain et al.* (2005) showed that for 5 – 20% of the time, magnetosheath electrons are in fact observed at the altitude of MGS, such that the MPB had moved to altitudes below 400 km.

5.4 Case studies with simultaneous measurements

Using two-spacecraft simultaneous measurements we will show three case studies of how the solar wind dynamic pressure affects the position and shape of the Mars BS and MPB. Later, in Section 5.5, we will present results from statistical studies of how various factors influence the boundaries.

For the case studies, we have chosen an interval when the solar wind dynamic pressure starts at low values of ~ 0.3 nPa before increasing to higher values of $\sim 1-2$ nPa for approximately two days before decreasing again to low values. This interval is suitable for case studies of the influence of the dynamic pressure for several reasons. There are simultaneous measurements from MEX and MGS with all instruments running while crossings of the MPB and the BS by MEX occur at different SZA which give an indication of the shape of the boundaries. There are also times when MGS is at low SZAs and has a chance of seeing the MPB being pushed inward at the same time as MEX crosses the boundaries at other SZAs, which gives further indications of the shape of the boundaries. Furthermore, the varying solar wind conditions during this interval enables observations of the response of the boundaries respond to the different solar wind conditions while the EUV flux is steady.

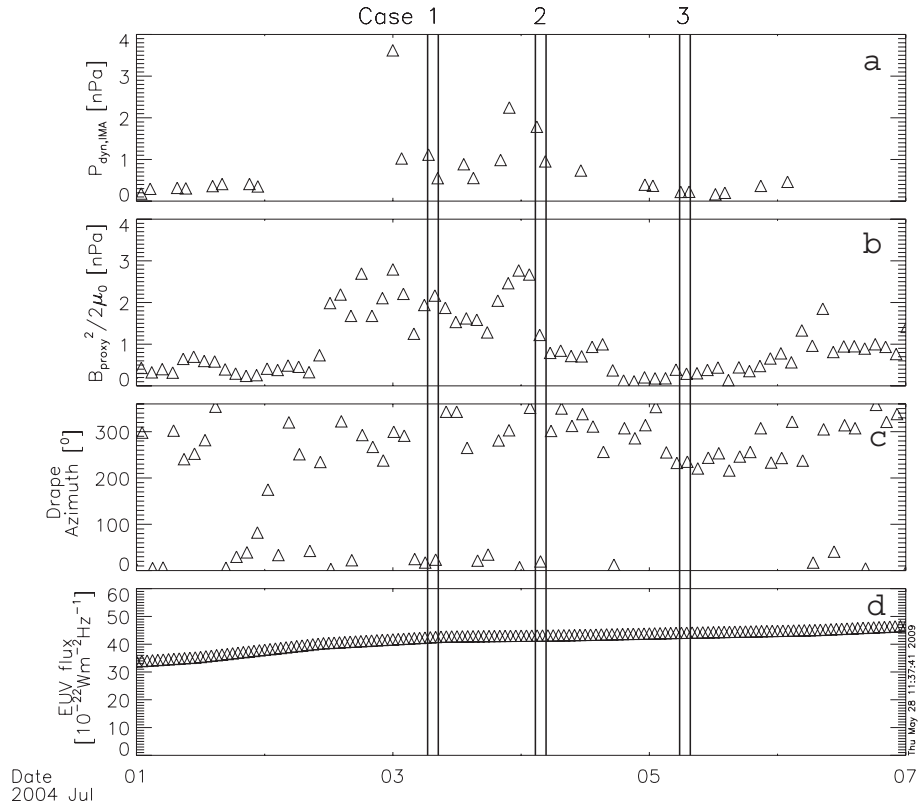


Figure 5.2: Time series of (a) MEX measurements of solar wind dynamic pressure, (b) the MGS pressure proxy, (c) the MGS magnetic field draping direction and (d) solar EUV flux proxy. Three case studies of the variability of the MPB and BS are performed in Figures 5.3-5.5 during the intervals indicated by the black vertical lines.

No boundary crossings occur over the strongest crustal fields where they can be significantly pushed upward. The BS and MPB crossings by MEX occur close to the plane which contains the IMF so that the convection electric field $\mathbf{E}_{\text{conv}} = -\mathbf{v} \times \mathbf{B}$ should have a small effect on the boundary location.

Figure 5.2 shows a seven day time series of data from MEX measurements of the solar wind dynamic pressure, MGS proxies for the dynamic pressure and IMF direction as well as a proxy for solar EUV flux. The general agreement between the pressure measured by MEX/IMA, in panel (a), and the pressure proxy, converted to magnetic pressure from MGS, in panel (b), is

quite good, with a correlation coefficient of 0.8 if the MGS values are interpolated to the time of the MEX values. We note that the MGS pressure proxy values during the interval in Figure 5.2 are generally higher than the measured values from MEX/IMA. The three intervals on 3 July, 4 July and 5 July 2004 indicated by vertical black lines in Figure 5.2 have been studied in more detail in Figure 5.3 - 5.5, respectively.

Figure 5.3 shows a time series of MGS and MEX measurements and orbit geometry from the interval indicated as Case 1 on 3 July 2004 in Figure 5.2. During this interval the solar wind dynamic pressure is higher than normal as indicated by both MEX and MGS measurements in Figure 5.2. MEX crosses the BS and MPB inbound at 06:39 UT and 07:18 UT, respectively, and outbound at 08:22 UT and 08:01 UT, respectively. The position of both boundaries are farther in than average. In between the inbound MPB crossing and the outbound BS crossing by MEX MGS observes magnetosheath electrons, from 07:45 UT until 08:10 UT, indicating that the MPB has moved to altitudes below 400 km. The two dashed lines in panel (e) show possible shapes of the boundaries based on the two BS crossings by MEX and the three MPB crossings by MGS and MEX that happen closest together in time. We have not taken into account the position of the MEX inbound MPB crossing since we assume that the boundaries move on a time scale less than 20 min and the inbound MPB crossing by MEX occurs 27 min earlier than the next crossing. Since we only have two BS crossings, we are left with including both of them. Obviously, we cannot produce statistical fits based on three or four crossings. The dashed lines have therefore been produced simply by manually adjusting conic sections so that they fit with the crossings of the MPB and BS and have similar shapes to the statistical

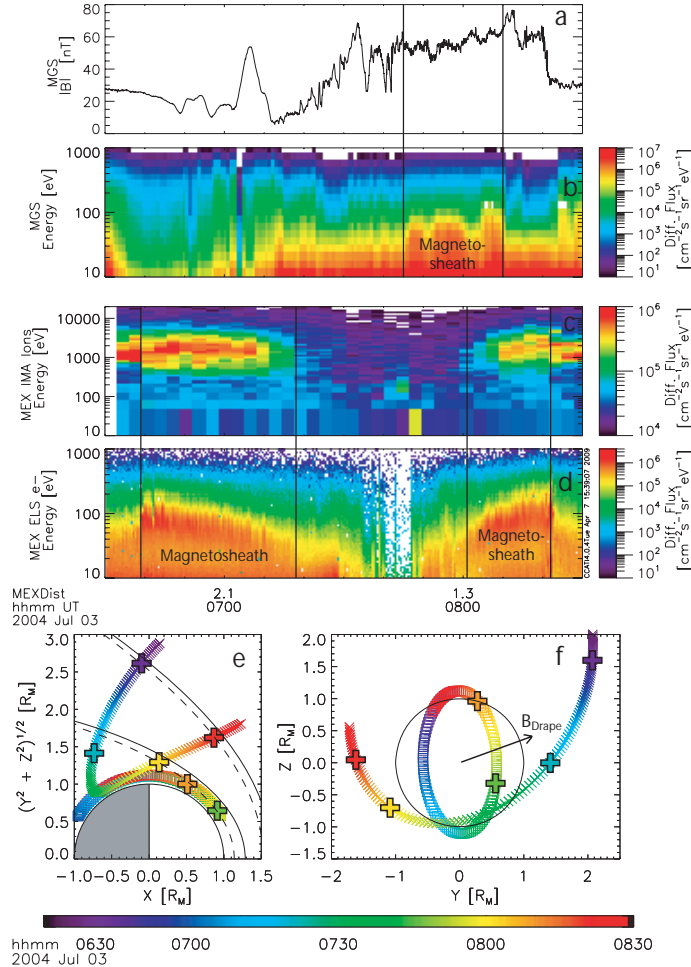


Figure 5.3: MGS and MEX data for Case 1: time series of (a) MGS/MAG magnetic field strength, (b) MGS/ER omni-directional electron spectrogram, (c) MEX/IMA omni-directional ion spectrogram, (d) MEX/ELS omni-directional electron spectrogram and the orbits of MGS (squares) and MEX (crosses) in (e) cylindrical MSO coordinates and in (f) the MSO $y - z$ plane, colour coded by time. The black vertical lines in panels (a-d) indicate when MGS or MEX crosses the BS and MPB. The position of those crossings are shown as large plus signs in panel (e) and (f). The black solid lines in panel (e) show the average location of BS and MPB (Vignes *et al.*, 2000) and the black arrow indicate the direction of the magnetic field draping from MGS measurements. The black dashed lines indicate possible shapes of the BS and MPB based on the observed crossings in this case.

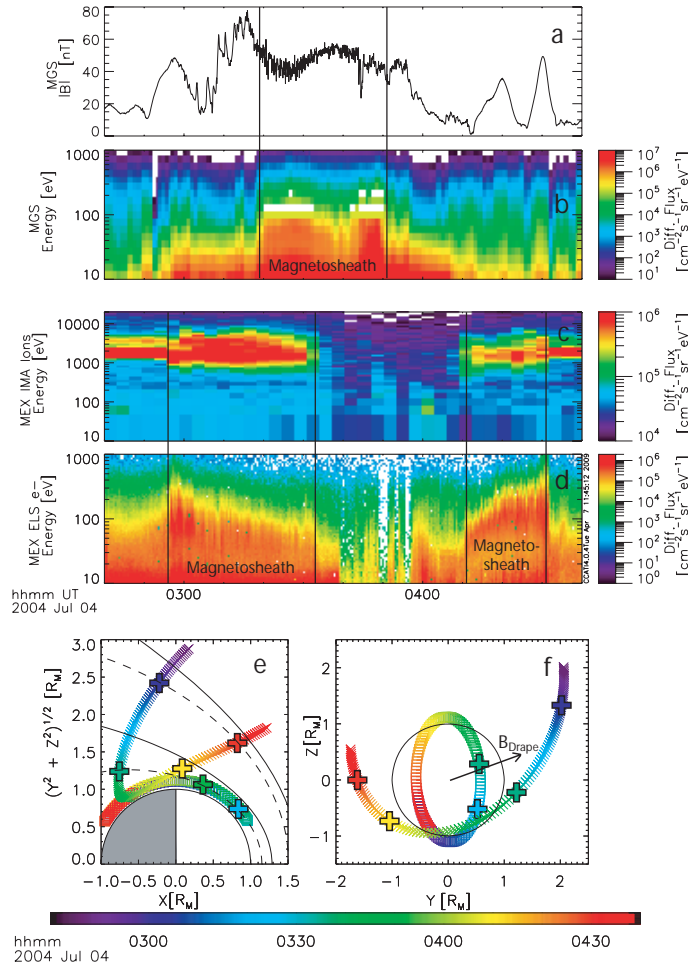


Figure 5.4: As for Figure 5.3 except for Case 2.

best fits. They are hence only to be taken as indications of what the shape of the boundaries might look like at this time.

Figure 5.4 shows data from the Case 2 interval on 4 July 2004 in Figure 5.2 in the same format as Figure 5.3. During this interval the pressure drops drastically from high (~ 2 nPa) to low (~ 1 nPa) values as shown in Figure 5.2. The dynamic pressure during the inbound leg of MEX is higher than in Case 1, such that the BS crossing observed by MEX at 02:56 UT and the subsequent MPB crossing at 03:33 UT consequently also occurs closer in than in Case 1. The outbound MPB crossing at 04:11 UT and BS crossing at 04:31

UT are, however, located only slightly closer in compared to the outbound crossings in Case 1. The pressure during the outbound leg as observed by MEX had in fact also dropped to only slightly higher values compared to the values from the outbound leg in Case 1. MGS also observed magnetosheath electrons during this interval, starting at 03:19 UT and ending at 03:51 UT. These magnetosheath observations started at roughly the same position in the $y - z$ plane as in Case 1 (compare panel (g) in Figures 5.4 and 5.3) but stops much earlier in this case, at a lower SZA, probably due to the fact that the upstream pressure decreased and the magnetosheath moves outward again.

Figure 5.5 shows data from the Case 3 interval on 5 July 2004 in Figure 5.2 in the same format as Figure 5.3 and 5.4. At this time the pressure of the solar wind had decreased to lower values of ~ 0.2 nPa as shown both by the MGS pressure proxy and the MEX measurements in Figure 5.2. The inbound BS crossing and MPB crossing observed by MEX at 05:45 UT and 06:15 UT, respectively, are still located farther in than average but have moved out compared to Case 2. The inbound BS crossing actually still occurs slightly farther in compared to the inbound BS crossings in Case 1, which indicates that factors other than solar wind dynamic pressure are involved in determining the position of the boundary such as magnetosheath plasma pressure, crustal fields (possibly on a more global scale since neither of the crossings occurs directly over strong crustal fields) or EUV flux. The outbound MPB crossing at 07:13 UT and BS crossing at 07:32 UT have moved outward significantly and are now located at larger radius than their average positions. The outbound MPB and BS crossings by MEX also occur in the $-\mathbf{E}_{conv}$ -hemisphere and are still farther out than average, indicating that the

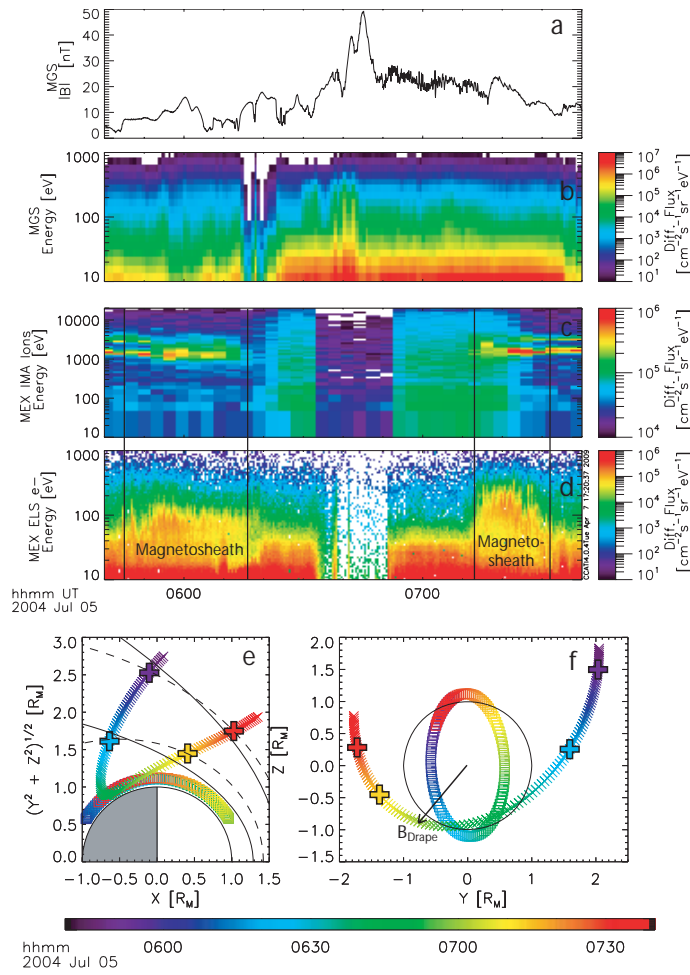


Figure 5.5: As for Figure 5.4 except for Case 3.

convective electric field has a weak influence on the boundary locations in this case. MGS observes no magnetosheath plasma at all during this interval. Evidently, the pressure was simply not high enough to push the MPB and the magnetosheath down to the altitude of MGS.

To summarize, both the MGS pressure proxy and MEX measurements indicate that the solar wind undergoes changes in dynamic pressure during the interval. The boundaries are observed to respond in such a way that they are pushed inward when the dynamic pressure is high, as shown in Figure 5.3. When the dynamic pressure is even higher, as during the inbound part in Figure 5.4, the boundaries are even farther in. The magnetosheath is in fact pushed inward to below the 400 km altitude of MGS. But when the pressure drops, which happens sometimes between 03:51 UT and 04:11 UT in Figure 5.4, the boundaries respond and move outward quickly and we can conclude that the response time of the plasma environment of Mars to new solar wind conditions is at least less than 20 min. From Figure 5.5, we conclude that the boundaries can either take asymmetric forms since the boundaries, during steady solar wind conditions, are farther out over one hemisphere than the other, or, that the shape of the boundaries do not follow the average best fit conic section shape in this case since the inbound and outbound crossings also occur at different SZAs. The 'asymmetry' does not seem to depend on the direction of the convective electric field, which could be a factor which causes asymmetry. Neither do the boundary crossings take place over strong crustal fields over which they could be significantly pushed upward. This leads us to believe that the latter of the two explanations is correct.

5.5 Statistical studies with simultaneous measurements

5.5.1 Influence of the solar wind dynamic pressure

In Figure 5.6 we show the result of a statistical study of how the radial distances of the BS and the MPB vary with solar wind dynamic pressure. We have used all the crossings observed by MEX during the overlapping mission time with MGS and extrapolated them to the terminator plane in order to remove the SZA angle dependence. The boundaries tend to be at higher altitudes at higher SZAs and in order to compare crossing with each other we need to remove this dependence and we therefore extrapolate the positions of all the crossings to the terminator plane. The extrapolation is done using the same method as described in *Vignes et al. (2002)* and *Cridder et al. (2002)*. First, the crossings are rotated by 4° about the MSO z axis to account for the perpendicular movement of Mars relative to the solar wind flow direction. A conic section is then fitted to each crossing of the BS and MPB in the MSO $(x, \sqrt{y^2 + z^2})$ plane by using the best fit values of the eccentricity ϵ and X_0 from *Edberg et al. (2008)*, varying only the semi-latus rectum L . For each conic section the terminator distance is then calculated. This method is not perfect, since the eccentricity of the boundaries can possibly also change when the governing factors change, but it remains the best we can do for now in order to remove the SZA dependence. Fitting curves by varying only ϵ or only X_0 does not give reasonable curves. Crossings that occur either much closer in than average or far downtail tend to produce fitted curves that pass through the planet. Varying L and keeping the other parameters fixed gives more reasonable curves in this sense. We therefore assume ϵ and X_0 to be

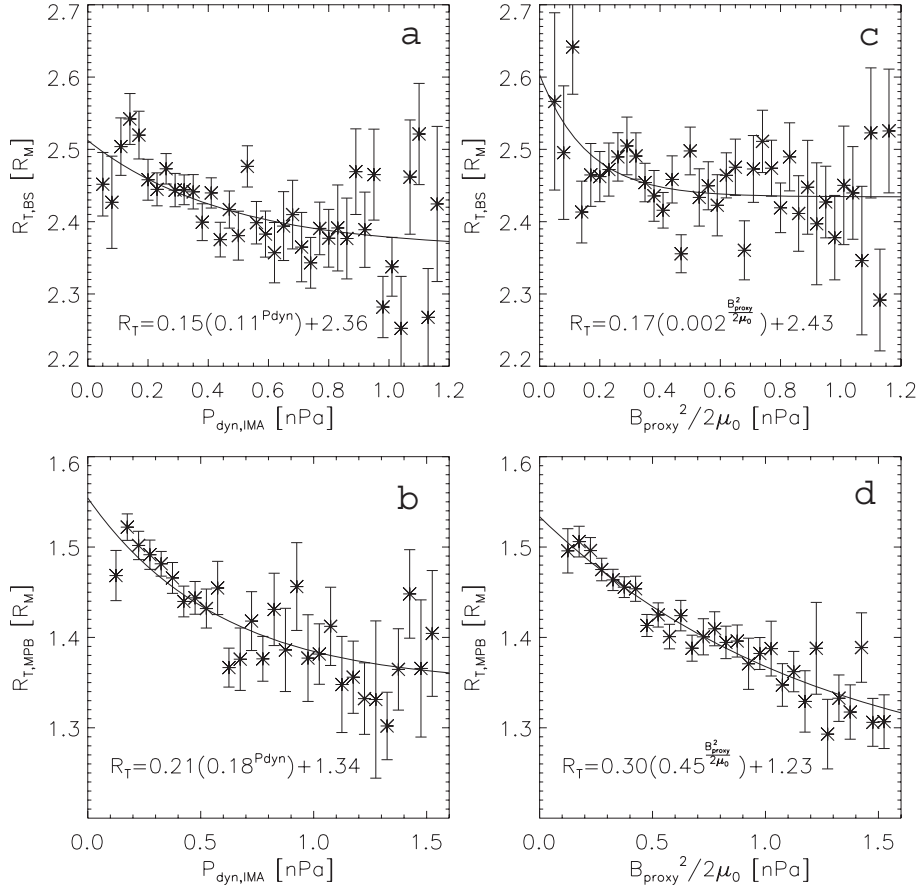


Figure 5.6: The extrapolated terminator distance of all (a) BS and (b) MPB crossings observed by MEX from Feb 2004 until Nov 2006 plotted as a function of solar wind dynamic pressure measured outside of the BS by MEX/IMA and the extrapolated terminator distance of all (c) BS and (d) MPB crossings as a function of the MGS pressure proxy linearly interpolated to the time of the crossings. The curve in panel (a) is a least square linear fit to the data and the curves in panels (b) and (d) are least square exponential fits to the data. The error bars show standard error on the mean.

constant.

Figure 5.6, panel (a), shows the extrapolated terminator distances R_T of the BS crossings as a function of upstream solar wind dynamic pressure $P_{dyn,IMA}$ as measured by MEX/IMA. The crossings are binned into $0.05 R_M$ bins and the mean values of the dynamic pressure upstream of all crossings in each bin is calculated. The error bars show standard error on the mean (standard deviation divided by number of samples in each bin). There is a trend to smaller radial distance for higher dynamic pressure, with a correlation coefficient of -0.51, and we fit an exponential curve (solid line) of the form $R_T = ab^{P_{dyn}} + c$, where a , b and c are free parameters, to the data points. In panel (b) we show the terminator radius of the MPB as a function of $P_{dyn,IMA}$. Again, there is a clear trend to smaller radial distances for higher $P_{dyn,IMA}$, with a correlation coefficient of -0.74, and we fit the same type of exponential curve to the data points. The error bars at low radial distance increase which could be an effect of the stronger influence of the crustal fields at lower altitudes. However, it could also be an effect of fewer data points in these bins. These two results clearly show that the solar wind dynamic pressure has an influence on the location of the boundaries, as would be expected.

We also compare these results to those obtained when we use the MGS pressure proxy rather than $P_{dyn,IMA}$. Panel (c) and (d) show the terminator radius of the BS and MPB, respectively, as a function of the MGS pressure proxy $\frac{B_{proxy}^2}{2\mu_0}$. The pressure proxy values are linearly interpolated to the time of the boundary crossings. Surprisingly, there is no obvious trend for the variation of the BS radius (correlation coefficient of -0.41) whereas the trend for the MPB is very similar to that in panel (b) (correlation coefficient of

-0.93). The lack of a trend for the BS crossings could be explained by the time difference between the time of the pressure proxy measurement and the BS crossings, which can be as long as 1 hour. The BS is expected to move on time scales much shorter than that. The error bars are quite large, however, and including them, then the results are not so discrepant. For the MPB we should have the same problem with the time difference but the results in panel (b) and (d) are still very similar, which rather disproves the argument above, if we assume that the BS and MPB move on the same timescales. It is also likely that the MPB and the BS can simply respond differently to changes in the solar wind dynamic pressure. The pressure proxy and the measured pressure values do not match up perfectly and this could be an indication of an unknown compression factor between the solar wind dynamic pressure outside the BS/MPB and the magnetic pressure inside the MPB.

It is also possible that when the BS is at very low radial distances the crustal magnetic fields become more important while at the same time the dynamic pressure becomes less important. The dynamic pressure can only push the boundary down to a certain altitude before the magnetic pressure from the crustal fields together with the plasma pressure inside of the BS become too high and the trend of a lower radial distance for a higher dynamic pressure vanishes. Similarly, when the BS is at very high radial distances the IMF direction could become more important while at the same time the dynamic pressure becomes less important. Inclusion of crossings that occur when other parameters, such as IMF direction, solar EUV flux and crustal magnetic fields, are kept approximately constant would be a way to decrease the error bars and get clearer trends. Unfortunately, the number of data points in each bin drops drastically by doing those selections. How-

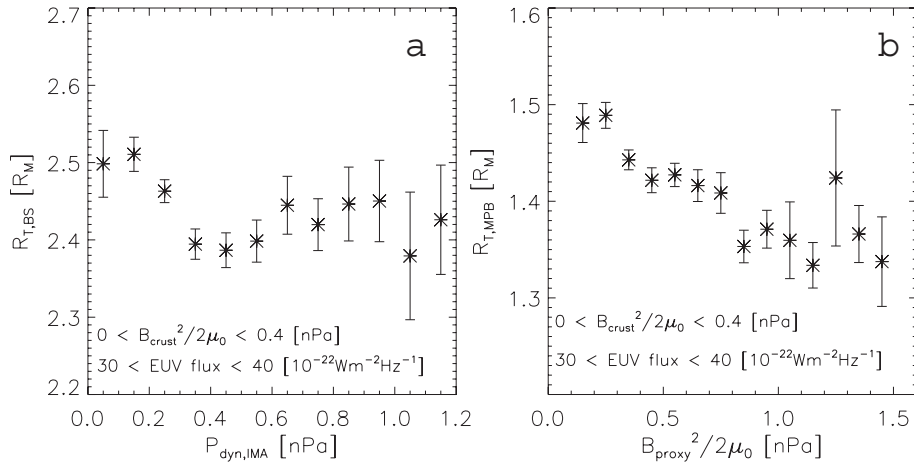


Figure 5.7: Same as Figure 5.6, panel (a) and panel (d), but now only including a subset of crossings such that the contribution from the solar EUV flux and the crustal magnetic field can be assumed approximately constant. The selected crossings fulfill the conditions of solar EUV flux and crustal magnetic pressure as shown in the Figure.

ever, the trends are still similar as can be seen in Figure 5.7 where we have only included crossings which occur when the solar EUV flux is between $30 \cdot 10^{-22} \text{Wm}^{-2} \text{Hz}^{-1}$ and $40 \cdot 10^{-22} \text{Wm}^{-2} \text{Hz}^{-1}$ and at the same time the magnetic pressure from the crustal magnetic fields is in between 0 nPa and 0.4 nPa. The two panels should be compared to panel (a) and panel (d) of Figure 5.6. The fewer number of crossings makes it necessary to bin the data in wider bins. The same drastic decrease in number of data points happens if we try to match MEX crossings with MGS proxy values that occur closer together in time. We therefore choose to include all crossings when examining the influence of each factor throughout this Section.

5.5.2 Influence of the IMF direction

In Figure 5.8 we show the result of a statistical study of the effect of the IMF direction on the boundary locations. The convective electric field $\mathbf{E} = -\mathbf{v} \times \mathbf{B}$

should cause the ions to go out into the solar wind and cause massloading of solar wind on one side of the planet thereby lifting the boundaries upward, whereas the ions on the other side go back into the planet. In panels (a) and (b) the distribution of the radial distances of BS crossings at northern and southern latitudes of Mars, respectively, are shown, divided into whether the crossing occur during locally upward ($+E$) or locally downward ($-E$) convective electric field. The direction of the magnetic field is obtained from the MGS draping proxy. In panel (c) and (d) the distribution is shown for the MPB. The radial distances of the crossings are extrapolated to the terminator plane. In panel (a), the mean value of R_T for the BS crossings that occur in the $+E$ -hemisphere and at northern latitudes is $2.48 \pm 0.01 R_M$ (plus or minus standard error of the mean) and is ~ 135 km higher compared to that in the $-E$ -hemisphere at northern latitudes, $2.44 \pm 0.01 R_M$. The mean values are significantly different according to a Student's t-test at a 95% confidence level. This difference is also observed for the crossings that occur at southern latitudes, in panel (b), and the difference is also significant according to a Student's t-test at a 95% confidence level. The southern latitude mean distances are $2.45 \pm 0.01 R_M$ in the $+E$ -hemisphere compared to $2.41 \pm 0.01 R_M$ in the $-E$ -hemisphere, a difference of ~ 135 km.

For the MPB, Figure 5.8, panel (c), there is also a significant (according to a Student's t-test at a 95% confidence level) difference of ~ 135 km between the mean values of the $+E$ and $-E$ hemisphere crossings at northern latitudes, $1.41 \pm 0.01 R_M$ compared to $1.37 \pm 0.01 R_M$. But for the crossings that occur at southern latitudes, in panel (d), the situation is reversed. The $+E$ hemisphere crossings have a ~ 200 km lower mean value than the $-E$ hemisphere crossings, $1.40 \pm 0.01 R_M$ compared to $1.46 \pm 0.01 R_M$. The south-

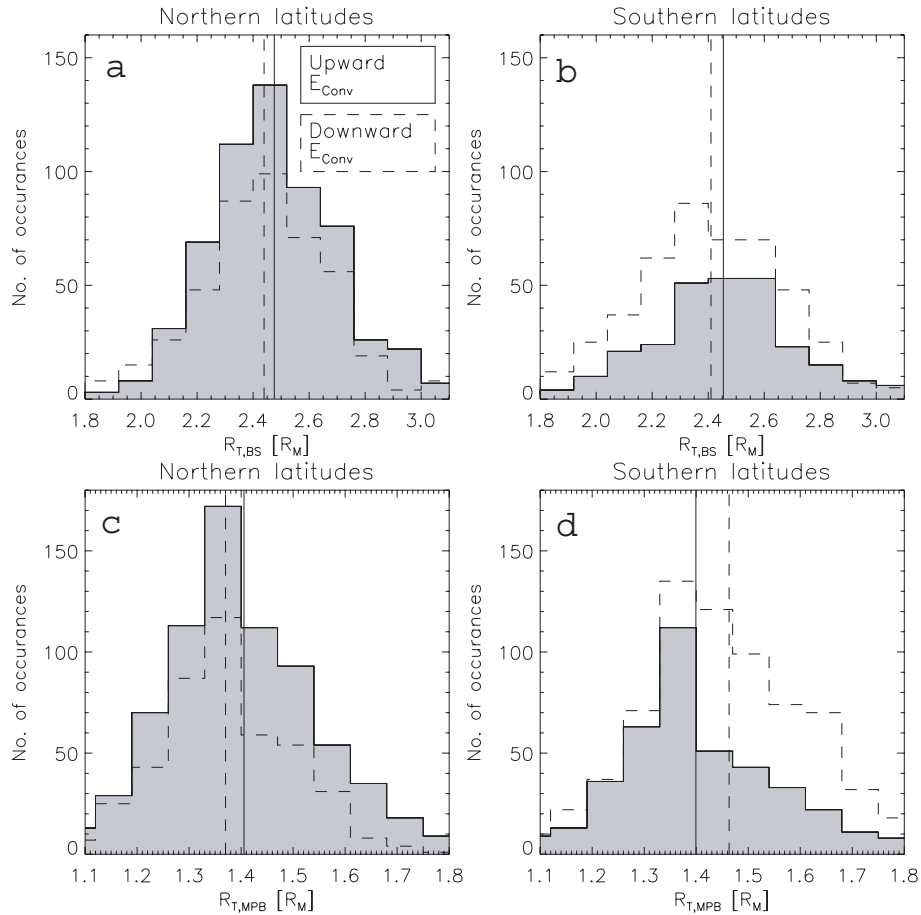


Figure 5.8: Distribution of the extrapolated terminator distance of BS crossings in the (a) northern and in the (b) southern hemisphere and MPB crossings in the (c) northern and in the (d) southern hemisphere observed by MEX from Feb 2004 until Nov 2006. In each panel, the distributions are subdivided into whether they occur when the convective electric field is directed locally upward (solid, filled) or locally downward (dashed). The mean extrapolated terminator distances are shown for crossings that occur in the locally upward convective electric field hemisphere (solid vertical line) and in the locally downward convective electric field hemisphere (dashed vertical line).

ern hemisphere MPB apparently reacts differently to an upward/downward convective electric field compared to the northern hemisphere, on average. It should be noted that the scatter in the extrapolated terminator distances is large and there are uncertainties involved in this study, e.g. the IMF direction is not determined perfectly, but only through a proxy and the time difference between the proxy value and the crossing has not been taken into account.

5.6 Influence of the crustal magnetic fields

In order to investigate the influence of the crustal magnetic fields we only use MEX measurements. The crustal fields have previously been shown to influence the boundaries by using MGS measurements and also MEX measurements on their own (*Cridder et al.*, 2002; *Brain et al.*, 2005; *Fränz et al.*, 2006b; *Edberg et al.*, 2008). However, no previous study has used such a large data set of crossings as we have in this study and we can now for the first time produce global maps of the radial distances of the boundaries. Panel (a) and (b) in Figure 5.9 show two global $10^\circ \times 10^\circ$ longitude-latitude maps colour coded by the radial distances of the BS and MPB, respectively. All crossings from Feb 2004 until Jan 2009 from the dayside of Mars are used and the mean of the radial distances of all crossings within each bin are shown. Bins with less than two crossings are coloured black. Note that the strongest crustal fields are located in the southern hemisphere at longitudes between 90° and 270° (*Connerney et al.*, 2005). The map of the BS crossings, panel (a), shows no distinct influence of the crustal magnetic fields on the altitude of the boundary, i.e. there is no specific region where the boundary is at

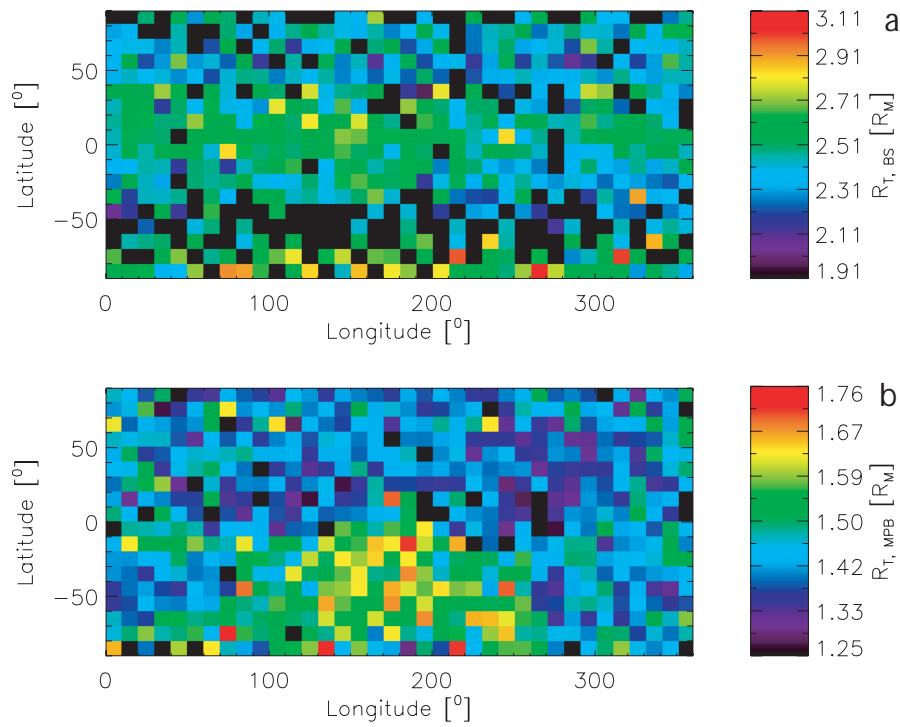


Figure 5.9: Longitude-latitude maps colour coded by the extrapolated terminator distance R_T of the (a) BS and (b) MPB. Only dayside crossings were used. Black bins means that there were less than two crossings in that region.

larger radial distance than elsewhere and which also corresponds to a region of strong crustal fields. There are, unfortunately, many empty bins at southern latitudes where the crustal fields are strongest. However, the mean value of R_T of all the dayside BS crossings in the northern hemisphere is $2.45 R_M$ compared to $2.49 R_M$ in the southern hemisphere and in the bottom rows of panel (a), at southern latitudes, there is a weak tendency that the crossings are at higher distances. The difference is statistically significant according to a Student's t-test at 95% confidence level. This difference is smaller than the difference presented in *Edberg et al.* (2008) where MGS crossings were used. The accuracy in this study should, however, be better due to the much larger data set.

The influence of the crustal magnetic fields on the MPB is much clearer. In panel (b) of Figure 5.9 there is a large area at southern latitudes between longitudes from $\sim 90^\circ$ to $\sim 270^\circ$, where the MPB occurs at larger radial distances than elsewhere. This region corresponds very closely to the region where the strongest crustal fields are located. Also, at latitudes above -30° and at longitudes between 0° and 90° there is a less prominent but still visible area of higher MPB which corresponds to a region of intermediately strong crustal fields.

In Figure 5.10 we show the extrapolated terminator distances of all the dayside crossings of the BS and MPB plotted as functions of magnetic pressure contributed from the crustal anomalies. The magnetic field strength is estimated by using the model from *Cain et al.* (2003) and calculate the field strength at 100 positions evenly spaced on a $10^\circ \times 10^\circ$ longitude-latitude grid centered radially below each crossings at 400 km. The mean over these 100 values are then taken as the field strength for each individual crossing. We

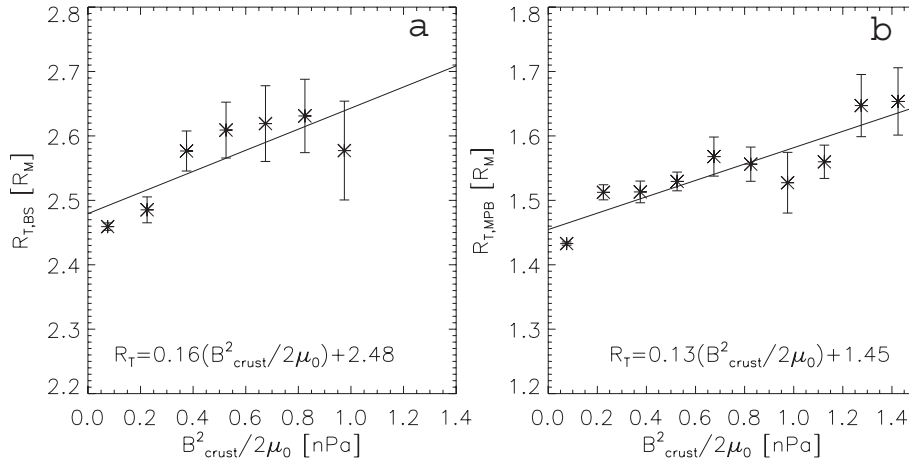


Figure 5.10: Extrapolated terminator distance of all the (a) BS and (b) MPB crossings observed by MEX from Feb 2004 until Jan 2009 plotted as a function of the magnetic pressure from the crustal magnetic field as calculated from the model by Cain et al. (2003). The solid lines are fitted curves to the data points and the error bars show standard error on the mean values.

choose this method since the crustal field has a high spatial variability and just calculating the crustal field value at the exact location of the crossing will not necessarily give a correct estimate. The crossings are then binned in 0.15 nPa bins and the mean value of the distance for all crossing within each bin is calculated. For the BS, we fit a linear least-square curve to the data points, as given by the equation in the figure. There is, as indicated before, a trend of a larger distance for higher crustal magnetic pressure for values of the crustal magnetic field pressure up to 1.0 nPa but for higher values of the crustal fields strength there are not enough data points. For the MPB, the linear increase of the distance with increasing crustal magnetic pressure is equally clear such that the crustal magnetic pressure has a strong influence on the MPB location. It should be mentioned that the scatter in position of crossings is extensive and the data presented are only mean values.

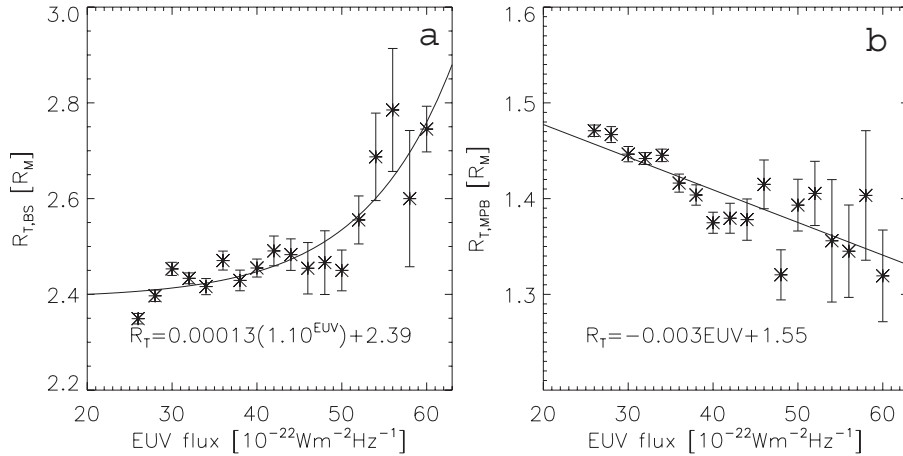


Figure 5.11: Extrapolated terminator distance of the (a) BS and (b) MPB crossings observed by MEX from Feb 2004 until Nov Jan 2009 plotted as a function of solar EUV flux proxy. The solid lines are fitted curves to the data points and the error bars show standard error on the mean values.

5.7 Influence of the solar EUV flux

In Figure 5.11 we show how the solar EUV flux affects the location of the BS and MPB. The crossings are divided into $2.0 \cdot 10^{-22}Wm^{-2}Hz^{-1}$ bins and the mean of the radial distances for all crossings within each bin is calculated. There is a clear trend of a larger BS radius for a higher EUV flux and it seems to increase exponentially. For the BS we therefore fit an exponential curve of the form $R_T = ab^{P_{dyn}} + c$, where a , b and c are free parameters as shown in panel (a). The MPB on the other hand clearly decreases in radius when the solar EUV flux increases and it seems to decrease linearly as the fit in panel (b) shows. *Modolo et al.* (2006) used hybrid simulations to study the influence of the EUV on the plasma boundary and found that the BS was pushed outward at the subsolar point but moved in at the terminator plane when going from solar minimum to maximum conditions, while the MPB only moved inward at the terminator, in agreement with this study.

The data used in this study are all taken during the declining phase of the solar cycle and during solar minimum (years 2004 - 2009) and we cannot yet determine how the EUV flux at solar maximum will affect the boundaries.

5.8 Summary and conclusions

We have shown case studies and statistical studies using single as well as two-spacecraft simultaneous and non-simultaneous measurements of how the solar wind dynamic pressure, the IMF direction, the crustal magnetic fields and the solar EUV flux affects the BS and MPB. We have produced expressions for how these factors influence the boundaries which enables us to determine their relative importance. We have not been able to study the influence of the solar wind magnetosonic Mach number since we do not have upstream magnetic field measurements. At Venus for instance, the magnetosonic Mach number has been shown to be of importance in determining the position of the BS (*Russell et al.*, 1988) and it is reasonable to assume that it should play a role at Mars too.

The case studies (Figures 5.3 - 5.5) employ simultaneous MEX and MGS measurements during an interval when the solar wind dynamic pressure changes from high to low and the dynamic pressure is assumed to have the main influence on the boundary locations. The effect of the high pressure solar wind on the boundaries is indeed observed to be an inward movement of both boundaries. The MPB is in fact pushed closer to the planet than the altitude of MGS (~ 400 km). Both BS and the MPB remains compressed until the solar wind dynamic pressure has decreased back to lower values. We can provide an upper limit of ~ 20 min for how long it takes for the Martian

plasma environment to adapt to new upstream solar wind conditions (Figure 5.4). The shapes of the boundaries seem to alter during this time as well as indicated by near-simultaneous measurements of the MPB by MEX and MGS (Figure 5.4, panel (f)). The BS, which is only observed by MEX and separated in time from the inbound to the outbound by ~ 1.5 hours, making it far from simultaneous, might also change its shape (Figure 5.3 and Figure 5.6, panel (f)). However, the BS is expected to move on time scales much shorter than this and this shape estimate is therefore very uncertain.

A statistical study of how the position of all MEX boundary crossings during the time of the mission overlap with MGS (Feb 2004 - Nov 2006) varies with solar wind dynamic pressure has also been performed (Figure 5.6). The boundaries are, on average, found to decrease exponentially in altitude with increasing pressure. Very similar results are produced when using the solar wind dynamic pressure as determined from a proxy from MGS data and by direct measurements from MEX. The statistical studies in Figure 5.6 also provide confidence in the accuracy of the MGS and MEX measurement, which independently give very similar result. However, for the BS the method of using the MEX measurements give a seemingly clearer result to how the radial distance decrease with increasing dynamic pressure. If the MGS pressure is used, the trend is less clear but still visible. The BS could possibly move on shorter time scales than the MPB and the MGS pressure proxy has a too poor time resolution which would mean that the MGS proxy is not suitable for studying the variation of MEX BS crossings with dynamic pressure. Also, the trend for the MPB appears clearer if the MGS pressure proxy is used rather than if the MEX/IMA measurements are used. These results indicate that the BS and MPB do not respond in exactly

the same way when facing changes in the upstream solar wind conditions.

A statistical study of how the boundaries react to different directions of convective electric field has also been performed (Figure 5.8) by using two-spacecraft measurements. We show that the BS has a 135 km larger average radial distance in the hemisphere of locally upward convective electric field compared to that in the hemisphere of locally downward convective electric field. The same difference is valid for the MPB but only in the northern hemisphere where the boundary during locally upward convective electric field has a 135 km larger average radial distance compared to when locally downward. In the southern latitudes, the situation seems to be reversed and the MPB is closer to the planet in the hemisphere of locally upward electric field, by 200 km on average. The difference is possibly due to the influence of the crustal magnetic fields, which are strongest in the southern hemisphere and disturb the (weak) effect of asymmetric massloading. Overall, the IMF direction has a weak influence on the boundaries if compared to other factors.

We also confirm observations, by using MEX measurements only, that the crustal fields affect both the MPB and the BS strongly by providing additional magnetic pressure. The radial distances of the BS and the MPB increase linearly with the crustal magnetic pressure.

The EUV flux, which ionises neutrals in the extended exosphere of Mars and increases the plasma pressure, is also shown to have a strong influence on both boundaries. The BS radius increases exponentially with increasing EUV flux while the MPB radius is observed to decrease linearly with increasing EUV flux. An explanation for this could be that the plasma pressure in the magnetosheath, in between the BS and the MPB, could be significantly increased with increasing EUV flux which could cause the BS to move out-

ward and the MPB to move inward. We have not found a correlation between solar EUV flux and high dynamic pressure which could have explained the result for the MPB.

There are several sources of error involved in this study, which causes scatter in the location of the boundaries. These errors include the time delay between MGS proxy values/upstream MEX measurements and the boundary crossings, the unknown x -component of the magnetic field and the unknown upstream magnetosonic Mach number. A sheared solar wind flow would also distort the results. The solar EUV proxy could also introduce an error since it is extrapolated from Earth and so can also the extrapolation of the boundary distances to the terminator plane do.

We can compare our observations of which factors control the location the plasma boundaries to models. The IMF direction is generally shown to be of importance in hybrid models which take kinetic effects in to account (*Böswetter et al.*, 2004; *Modolo et al.*, 2006), but is not really important in this study. Other factors seem to be more important. However, the IMF direction is, as stated before, not directly measured but rather determined through a proxy, which introduces errors. The dynamic pressure dependence is in reasonable agreement with models, both hybrid and MHD models (*Böswetter et al.*, 2004; *Modolo et al.*, 2006). The crustal fields have not been studied extensively in models but will most likely become included in most future studies. *Harnett and Winglee* (2003) have performed such a study and showed that the MPB is affected to a large extent, which is in agreement with the results presented here, while the BS was not affected, which is in disagreement. The solar EUV flux dependence has been studied by *Modolo et al.* (2006) who found a weak dependence, in contrast to the results here. It should be noted

that almost all models obtain very different results in terms of plasma escape rates as well as boundary locations, when the same input conditions are used (*Brain et al.*, 2009).

In summary, quantitative expressions for the main factors that affect that BS and the MPB have been produced. The factors that mainly affect the MPB include the solar wind dynamic pressure, crustal magnetic fields and solar EUV flux while the IMF direction has a weaker influence. For the BS, the crustal magnetic fields, the solar wind dynamic pressure and the solar EUV are again the main controlling factors while the IMF direction plays a minor role.

Chapter 6

Conclusions & future work

6.1 Conclusions

This Thesis has focused on the solar wind interaction with Mars and the boundaries and regions that form as a result of that interaction. We have studied the location, shape and dynamics of the MPB and BS and also which parameters that influence the properties of the boundaries. Throughout these studies we have used single spacecraft measurements as well as simultaneous and non-simultaneous two-spacecraft measurements.

In Chapter 3 we have used MGS data to produce best-fit statistical models of the average shape of both the MPB and BS. We have also studied the influence of the crustal magnetic fields on the two boundaries and found that the MPB is pushed upward over specific regions where the crustal magnetic field of Mars is particularly strong. Where the crustal magnetic fields are even stronger, the MPB is pushed to even higher altitudes. The BS was found to be at higher altitudes over the entire southern hemisphere, where the crustal magnetic fields are mainly located, but there was no observable difference between strong or intermediately strong crustal magnetic field regions.

The average shapes of both boundaries take the form of conic sections which has previously been determined. We have, however, extended the previous studies by including more data points which has increased the statistical accuracy as well as constrained the shape of the MPB by introducing a new method for performing the fitting. The new method takes into account the fact that there are no MPB crossings at low SZAs which otherwise introduces an error in the fitting technique. The previous models have had their lowest altitudes at a SZA of $\sim 45^\circ$ rather than at 0° which would have been expected. We therefore perform a fitting where we fix the subsolar altitude to a value based on the lowest altitude of the previous fits. The result is a more realistic model of the MPB. We have also studied the magnetic field strength inside the MPB and found that it increases toward the dayside as well as when the MPB is pushed closer to the planet.

In Chapter 4 we have used simultaneous measurement from Rosetta and MEX to study the behavior of the MPB and BS during low and high solar wind pressure. The Rosetta swingby of Mars, which took place in February 2007, enabled the first near-simultaneous two-spacecraft study of plasma boundaries at Mars as well as an opportunity for using Rosetta as a solar wind monitor while MEX sampled the MPB and BS. The near-simultaneous BS and MPB measurements took place within an interval of ~ 3 hours, during which the solar wind was quiet and slow with a normal density. We use the near-simultaneous boundary crossings to confirm the previously modelled shapes and find that both the MPB and the BS shape are in reasonable agreement with the models. The MPB is found at its average location as would be expected during quiet solar wind conditions. The BS is, however, significantly compressed during this interval, but still with a conic section

shape.

A day after the CA of Rosetta a high pressure solar wind region is observed to pass by Mars during a ~ 24 hour interval. As Rosetta monitors the solar wind and the IMF downstream of Mars, MEX observes how the MPB and BS become asymmetric in shape. The observed boundary in the northern/dawn hemisphere is closer in than the observed boundary in the southern/dusk hemisphere. We test various factors which could cause the asymmetry, such as the IMF direction and crustal magnetic fields, without finding a good explanation. The BS altitude clearly increases on one side of the planet even though the solar wind pressure increases which is rather unexpected. At the same time, a significant fraction of ionospheric ions are observed to accelerate away from the planet in the hemisphere where the boundaries are at lower altitudes. We therefore suggest that the observed boundary asymmetry is related to the ionospheric outflow as the thermal plasma pressure decreases when plasma is swept away.

In Chapter 5 we use both simultaneous and non-simultaneous two-spacecraft measurements from MEX and MGS to study some factors which have been suggested to control the altitude of the MPB and BS. First, we introduce previously produced proxies of the solar wind dynamic pressure and IMF direction based on MGS measurements as well as a proxy of the EUV flux based on F10.7 measurements at Earth. We compare the solar wind dynamic pressure proxy with the measured solar wind dynamic pressure from the IMA instrument onboard MEX and find that they are in reasonable agreement. We use the proxies to present a case study during an interval when the solar wind dynamic pressure is observed to be the governing factor of the movement of the MPB and BS. The boundaries move to lower altitudes as the

solar wind dynamic pressure increases and subsequently to higher altitudes when the pressure decreases. This case study also gives an indication of the time scale of which the plasma boundaries move when the dynamic pressure changes, which is found to be less than 20 min.

Furthermore, by using the three proxies and the measured upstream dynamic pressure, we produce analytical expressions of the altitude of the boundaries, in terms of terminator distance, as functions of solar wind dynamic pressure, solar EUV flux and crustal magnetic fields. We also study the influence of the IMF direction. The result shows that both the MPB and the BS are mainly controlled by the solar wind dynamic pressure, crustal magnetic fields and solar EUV flux while the IMF direction plays a minor role.

6.2 Future work

What is left for the future in terms of studies of plasma boundaries at Mars include determining in more detail the pressure balance between the MPB and the underlying MPR and how that effects the BS location. Also, the boundaries have not yet been studied during solar maximum and their behavior during very high solar EUV flux is unknown. Related to this is the time scale on which these boundaries, and regions, adapt to changing solar wind conditions. This time scale is expected to be on the order of minutes, or even seconds, and has not been properly explored. We do touch upon the subject in Chapter 4 and 5 but not in any great detail. Seasonal effects have not been studied in any detail in this Thesis and have been left for the future. Since the Mars rotation axis is tilted, the boundaries could possibly

be located farther in over the summer hemisphere compared to the winter hemisphere. To produce a functional fit of the boundaries is also desired. The published models of the boundaries have so far only involved producing best-fit statistical shapes but to have a model as a function of solar wind pressure, crustal magnetic field strength and solar EUV flux, for instance, would be even better. This is something that could be extracted from the quantitative expressions presented in Chapter 5 in a future study.

While the location and shape of the Martian plasma boundaries have been extensively explored by several single spacecraft missions in the past, there has not been any dedicated multi-spacecraft mission for studies of the plasma boundaries. For the future, such missions would be very advantageous in the study of the solar wind interaction with Mars. At Earth, multi-spacecraft missions such as Cluster and Themis have been very successful as they can resolve spatial from temporal variations in the plasma environment. No such dedicated mission is currently planned for Mars but there might be more occasions when two or even three individual spacecraft missions are present at the same time, with plasma instruments onboard. The Maven mission from NASA is planned to be launched in 2013 and the Russian Phobos-Grunt mission will be launched at approximately the same time which will include a Chinese orbiter, Yinghuo-1, as well. If MEX is still alive at Mars when these three spacecraft arrive there will be an unprecedented coverage of plasma measurements around Mars.

To have a long-term upstream solar wind monitor at Mars would make it possible to study the influence of different solar wind conditions on the Martian plasma environment in more detail. At present, upstream solar wind monitoring spacecraft at the Earth can be used, to some extent, even for

Mars. Especially when Mars and Earth are aligned on a straight Mars-Earth-Sun line, larger solar events such as coronal mass ejections can be tracked from the Earth to Mars. Also, during solar minimum conditions when the Sun is relatively quiet, most corotating interaction regions (CIRs) seen at Earth can easily be traced to Mars, even when the two planets are separated by as much as $\sim 120^\circ$ in longitude from each other. This is something which is presently being explored in a current study where we use Stereo and ACE data to trace CIRs to Mars. The aim is to determine what the effects these high pressure solar wind regions have on the plasma environment at Mars.

Other interesting scientific questions which still need to be addressed in the future includes the physics of the plasma environment close to the crustal magnetic fields. With both magnetic field and electric field instruments as well as ion and electron sensors several physical mechanisms such as reconnection and auroral emissions could be studied in more detail above regions of strong crustal magnetic fields. The evolution of the atmosphere of Mars is also one of the main scientific questions to be addressed. For instance, the outflow of the cold ion population has not been studied yet which is important for determining how the atmosphere has evolved in the past. All this could possibly be explored with the multi-instrument missions of Maven and Phobos-Grunt/Yinghuo-1 during the next decade.

Bibliography

- Acuña, M. H., J. E. P. Connerney, P. Wasilewski, R. P. Lin, K. A. Anderson, C. W. Carlson, J. McFadden, D. W. Curtis, D. Mitchell, H. Reme, C. Mazelle, J. A. Sauvaud, C. D'Uston, A. Cros, J. L. Medale, S. J. Bauer, P. Cloutier, M. Mayhew, D. Winterhalter, and N. F. Ness (1998), Magnetic field and plasma observations at Mars: Initial results of the Mars Global Surveyor mission, *Science*, *279*, 1676–1680.
- Acuña, M. H., J. E. P. Connerney, N. F. Ness, R. P. Lin, D. Mitchell, C. W. Carlson, J. McFadden, K. A. Anderson, H. Reme, C. Mazelle, D. Vignes, P. Wasilewski, and P. Cloutier (1999), Global distribution of crustal magnetization discovered by the Mars Global Surveyor MAG/ER experiment, *Science*, *284*, 790–793.
- Arkani-Hamed, J. (2004), A coherent model of the crustal magnetic field of Mars, *J. Geophys. Res.*, *109*, E09,005, doi:10.1029/2004JE002265.
- Auster, H. U., I. Apathy, G. Berghofer, A. Remizov, R. Roll, K.-H. Fornacon, K.-H. Glassmeier, G. Haerendel, I. Hejja, E. Kührt, W. Magnes, D. Moehlmann, U. Motschmann, I. Richter, H. Rosenbauer, C. T. Russell, J. Rustenbach, K. Sauer, K. Schwingenschuh, I. Szemerey, and R. Waesch (2007), ROMAP: Rosetta Magnetometer and Plasma Monitor, *Space Sci. Rev.*, *128*, 221–240, doi:10.1007/s11214-006-9033-x.
- Barabash, S., R. Lundin, H. Andersson, K. Brinkfeldt, A. Grigoriev, H. Gunell, M. Holmström, M. Yamauchi, K. Asamura, P. Bochsler, P. Wurz, R. Cerulli-Irelli, A. Mura, A. Milillo, M. Maggi, S. Orsini, A. J. Coates, D. R. Linder, D. O. Kataria, C. C. Curtis, K. C. Hsieh, B. R. Sandel, R. A. Frahm, J. R. Sharber, J. D. Winningham, M. Grande, E. Kallio, H. Koskinen, P. Riihelä, W. Schmidt, T. Säles, J. U. Kozyra, N. Krupp, J. Woch, S. Livi, J. G. Luhmann, S. McKenna-Lawlor, E. C. Roelof, D. J. Williams, J.-A. Sauvaud, A. Fedorov, and J.-J. Thocaven (2006), The Analyzer of Space Plasmas and Energetic Atoms (ASPERA-

- 3) for the Mars Express mission, *Space Sci. Rev.*, *126*, 113–164, doi:10.1007/s11214-006-9124-8.
- Barabash, S., A. Fedorov, R. Lundin, and J.-A. Sauvaud (2007), Martian Atmospheric Erosion Rates, *Science*, *315*, 501–503, doi:10.1126/science.1134358.
- Bertucci, C., C. Mazelle, D. H. Crider, D. Vignes, M. H. Acuña, D. L. Mitchell, R. P. Lin, J. E. P. Connerney, H. Rème, P. A. Cloutier, N. F. Ness, and D. Winterhalter (2003), Magnetic field draping enhancement at the Martian magnetic pileup boundary from Mars global surveyor observations, *Geophys. Res. Lett.*, *30*(2), 1099, doi:10.1029/2002GL015713.
- Bertucci, C., C. Mazelle, M. H. Acuña, C. T. Russell, and J. A. Slavin (2005), Structure of the magnetic pileup boundary at Mars and Venus, *J. Geophys. Res.*, *110*, A01,209, doi:10.1029/2004JA010592.
- Boesswetter, A., U. Auster, I. Richter, M. Fränz, B. Langlais, S. McKenna-Lawlor, S. Simon, U. Motschmann, K. H. Glassmeier, N. J. T. Edberg, and R. Lundin (2009), Rosetta swing-by at mars - an analysis of the romap measurements in comparison with results of 3-d multi-ion hybrid simulations and mex/aspera-3 data, *Ann. Geophys.*, *27*(6), 2383–2398.
- Bößwetter, A., T. Bagdonat, U. Motschmann, and K. Sauer (2004), Plasma boundaries at Mars: a 3-D simulation study, *Ann. Geophys.*, *22*, 4363–4379.
- Brain, D., S. Barabash, A. Boesswetter, S. Bougher, S. Brecht, G. Chanteur, D. Crider, E. Dubinin, X. Fang, M. Fraenz, J. Halekas, E. Harnett, M. Holmstrom, E. Kallio, H. Lammer, S. Ledvina, M. Liemohn, K. Liu, J. Luhmann, Y. Ma, R. Modolo, A. Nagy, U. Motschmann, H. Nilsson, H. Shinagawa, S. Simon, and N. Terada (2009), A comparison of global models for the solar wind interaction with mars, *Icarus*, *In Press*, doi:10.1016/j.icarus.2009.06.030.
- Brain, D. A., F. Bagenal, M. H. Acuña, and J. E. P. Connerney (2003), Martian magnetic morphology: Contributions from the solar wind and crust, *J. Geophys. Res.*, *108*(A12), 1424, doi:10.1029/2002JA009482.
- Brain, D. A., J. S. Halekas, R. Lillis, D. L. Mitchell, R. P. Lin, and D. H. Crider (2005), Variability of the altitude of the Martian sheath, *Geophys. Res. Lett.*, *32*, L18,203, doi:10.1029/2005GL023126.
- Brain, D. A., D. L. Mitchell, and J. S. Halekas (2006), The magnetic field draping direction at Mars from April 1999 through August 2004, *Icarus*, *182*, 464–473, doi:10.1016/j.icarus.2005.09.023.

- Brecht, S. H., and S. A. Ledvina (2006), The Solar Wind Interaction With the Martian Ionosphere/Atmosphere, *Space Sci. Rev.*, *126*, 15–38, doi:10.1007/s11214-006-9084-z.
- Burch, J. L., R. Goldstein, T. E. Cravens, W. C. Gibson, R. N. Lundin, C. J. Pollock, J. D. Winningham, and D. T. Young (2007), RPC-IES: The Ion and Electron Sensor of the Rosetta Plasma Consortium, *Space Sci. Rev.*, *128*, 697–712, doi:10.1007/s11214-006-9002-4.
- Cain, J. C., B. B. Ferguson, and D. Mozzoni (2003), An $n = 90$ internal potential function of the Martian crustal magnetic field, *J. Geophys. Res.*, *108*(E2), 5008, doi:10.1029/2000JE001487.
- Carlsson, E., D. Brain, J. Luhmann, S. Barabash, A. Grigoriev, H. Nilsson, and R. Lundin (2008), Influence of IMF draping direction and crustal magnetic field location on Martian ion beams, *Planet. and Space Sci.*, *56*, 861–867, doi:10.1016/j.pss.2007.12.016.
- Chapman, S. (1931a), The absorption and dissociative or ionizing effect of monochromatic radiation in an atmosphere on a rotating earth, *Proc. of the Phys. Soc.*, *43*, 26–45, doi:10.1088/0959-5309/43/1/305.
- Chapman, S. (1931b), The absorption and dissociative or ionizing effect of monochromatic radiation in an atmosphere on a rotating earth part II. Grazing incidence, *Proc. of the Phys. Soc.*, *43*, 483–501, doi:10.1088/0959-5309/43/5/302.
- Connerney, J. E. P., M. H. Acuña, N. F. Ness, G. Kletetschka, , D. L. Mitchell, R. P. Lin, and H. Rème (2005), Tectonic implications of Mars crustal magnetism, *Proc. Natl. Acad. Sci.*, *102*(42), 14,970–14,975, doi:10.1073/pnas.0507469102.
- Crider, D., M. Acuña, J. Connerney, D. Mitchell, R. Lin, P. Cloutier, H. Rème, C. Mazelle, D. Brain, N. Ness, and S. Bauer (2001), Magnetic field draping around Mars: Mars Global Surveyor results, *Adv. Space Res.*, *27*, 1831–1836.
- Crider, D. H., M. H. Acuña, J. E. P. Connerney, D. Vignes, N. F. Ness, A. M. Krymskii, T. K. Breus, H. Rème, C. Mazelle, D. L. Mitchell, R. P. Lin, P. A. Cloutier, and D. Winterhalter (2002), Observations of the latitude dependence of the location of the martian magnetic pileup boundary, *Geophys. Res. Lett.*, *29*(L8), 1170, doi:10.1029/2001GL013860.
- Crider, D. H., D. Vignes, A. M. Krymskii, T. K. Breus, N. F. Ness, D. L. Mitchell, J. A. Slavin, and M. H. Acuña (2003), A proxy for determining solar wind dynamic pressure at Mars using Mars Global Surveyor data, *J. Geophys. Res.*, *108*(A12), 1461, doi:10.1029/2003JA009875.

- Crider, D. H., D. A. Brain, M. H. Acuña, D. Vignes, C. Mazelle, and C. Bertucci (2004), Mars Global Surveyor observations of solar wind magnetic field draping around Mars, *Space Sci. Rev.*, *111*, 203–221, doi:10.1023/B:SPAC.0000032714.66124.4e.
- Dubinin, E., M. Fränz, J. Woch, E. Roussos, S. Barabash, R. Lundin, J. D. Winningham, R. A. Frahm, and M. Acuña (2006), Plasma morphology at Mars: Aspera-3 observations, *Space Sci. Rev.*, *126*, 209–238, doi:10.1007/s11214-006-9039-4.
- Dubinin, E., R. Modolo, M. Fränz, J. Woch, F. Akalin, D. Gurnett, R. Lundin, S. Barabash, J. J. Plaut, and G. Picardi (2008a), Structure and dynamics of the solar wind/ionosphere interface on Mars. MEX-ASPERA-3 and MEX-MARSIS observations, *Geophys. Res. Lett.*, *35*, L11,103, doi:10.1029/2008GL033730.
- Dubinin, E., M. Fraenz, J. Woch, F. Duru, D. Gurnett, R. Modolo, S. Barabash, and R. Lundin (2009), Ionospheric storms on Mars: Impact of the corotating interaction region, *Geophys. Res. Lett.*, *36*, L01,105, doi:10.1029/2008GL036559.
- Dubinin, E. M., M. Fraenz, J. Woch, E. Roussos, J. D. Winningham, R. A. Frahm, A. Coates, F. Leblanc, R. Lundin, and S. Barabash (2008b), Access of solar wind electrons into the Martian magnetosphere, *Ann. Geophys.*, *26*, 3511–3524.
- Duru, F., D. A. Gurnett, D. D. Morgan, R. Modolo, A. F. Nagy, and D. Najib (2008), Electron densities in the upper ionosphere of Mars from the excitation of electron plasma oscillations, *J. Geophys. Res.*, *113*, A07,302, doi:10.1029/2008JA013073.
- Edberg, N. J. T., M. Lester, S. W. H. Cowley, and A. I. Eriksson (2008), Statistical analysis of the location of the martian magnetic pileup boundary and bow shock and the influence of crustal magnetic fields, *J. Geophys. Res.*, *113*, A08,206, doi:10.1029/2008JA013096.
- Edberg, N. J. T., U. Auster, S. Barabash, A. Bößwetter, D. A. Brain, C. M. Carr, S. W. H. Cowley, E. Cupido, F. Duru, A. I. Eriksson, M. Fränz, K.-H. Glassmeier, R. Goldstein, M. Lester, R. Lundin, R. Modolo, H. Nilsson, I. Richter, M. Samara, and J. G. Trotignon (2009a), Rosetta and Mars Express observations of the influence of high solar wind dynamic pressure on the Martian plasma environment, *Submitted to Ann. Geophys.*
- Edberg, N. J. T., D. A. Brain, M. Lester, S. W. H. Cowley, R. Modolo, M. Fränz, and S. Barabash (2009b), Plasma boundary variability at Mars

- as observed by Mars Global Surveyor and Mars Express, *Ann. Geophys.*, *27*, 3537–3550.
- Edberg, N. J. T., A. I. Eriksson, U. Auster, S. Barabash, A. Bößwetter, C. M. Carr, S. W. H. Cowley, E. Cupido, M. Fränz, K.-H. Glassmeier, R. Goldstein, M. Lester, R. Lundin, R. Modolo, H. Nilsson, I. Richter, M. Samara, and J. G. Trotignon (2009c), Simultaneous measurements of Martian plasma boundaries by Rosetta and Mars Express, *Planet. and Space Sci.*, *57*, 1085–1096, doi:10.1016/j.pss.2008.10.016.
- Eriksson, A. I., and E. Winkler (2008), Photoemission currents, solar EUV flux and spacecraft potential, *Submitted to IEEE Proc. Plasma Sci.*
- Eriksson, A. I., R. Boström, R. Gill, L. Åhlén, S.-E. Jansson, J.-E. Wahlund, M. André, A. Mälkki, J. A. Holtet, B. Lybekk, A. Pedersen, and L. G. Blomberg (2007), RPC-LAP: The Rosetta Langmuir Probe Instrument, *Space Sci. Rev.*, *128*, 729–744, doi:10.1007/s11214-006-9003-3.
- Espley, J. R., W. M. Farrell, D. A. Brain, D. D. Morgan, B. Cantor, J. J. Plaut, M. H. Acuña, and G. Picardi (2007), Absorption of MARSIS radar signals: Solar energetic particles and the daytime ionosphere, *Geophys. Res. Lett.*, *34*, L09,101, doi:10.1029/2006GL028829.
- Fedorov, A., E. Budnik, J.-A. Sauvaud, C. Mazelle, S. Barabash, R. Lundin, M. Acuña, M. Holmström, A. Grigoriev, M. Yamauchi, H. Andersson, J.-J. Thocaven, D. Winningham, R. Frahm, J. R. Sharber, J. Scherrer, A. J. Coates, D. R. Linder, D. O. Kataria, E. Kallio, H. Koskinen, T. Säles, P. Riihelä, W. Schmidt, J. Kozyra, J. Luhmann, E. Roelof, D. Williams, S. Livi, C. C. Curtis, K. C. Hsieh, B. R. Sandel, M. Grande, M. Carter, S. McKenna-Lawler, S. Orsini, R. Cerulli-Irelli, M. Maggi, P. Wurz, P. Bochsler, N. Krupp, J. Woch, M. Fränz, K. Asamura, and C. Dierker (2006), Structure of the Martian wake, *Icarus*, *182*, 329–336, doi:10.1016/j.icarus.2005.09.021.
- Fox, J. L. (1997), Upper limits to the outflow of ions at Mars: Implications for atmospheric evolution, *Geophys. Res. Lett.*, *24*, 2901–2904, doi:10.1029/97GL52842.
- Frahm, R. A., J. R. Sharber, J. D. Winningham, P. Wurz, M. W. Liemohn, E. Kallio, M. Yamauchi, R. Lundin, S. Barabash, A. J. Coates, D. R. Linder, J. U. Kozyra, M. Holmström, S. J. Jeffers, H. Andersson, and S. McKenna-Lawler (2006), Locations of Atmospheric Photoelectron Energy Peaks Within the Mars Environment, *Space Sci. Rev.*, *126*, 389–402, doi:10.1007/s11214-006-9119-5.

- Fränz, M., E. Dubinin, E. Roussos, J. Woch, J. D. Winningham, R. Frahm, A. J. Coates, A. Fedorov, S. Barabash, and R. Lundin (2006a), Plasma moments in the environment of Mars, *Space Sci. Rev.*, *126*, 165–207, doi: 10.1007/s11214-006-9115-9.
- Fränz, M., J. D. Winningham, E. Dubinin, E. Roussos, J. Woch, S. Barabash, R. Lundin, M. Holmström, H. Andersson, M. Yamauchi, A. Grigoriev, R. A. Frahm, J. R. Sharber, J. R. Scherrer, A. J. Coates, Y. Soobiah, D. R. Linder, D. O. Kataria, E. Kallio, T. Säles, P. Riihelä, W. Schmidt, H. E. J. Koskinen, J. Kozyra, J. Luhmann, E. Roelof, D. Williams, S. Livi, C. C. Curtis, K. C. Hsieh, B. R. Sandel, M. Grande, M. Carter, J.-A. Sauvaud, A. Fedorov, J.-J. Thocaven, S. McKenna-Lawler, S. Orsini, R. Cerulli-Irelli, M. Maggi, P. Wurz, P. Bochsler, N. Krupp, K. Asamura, and C. Dierker (2006b), Plasma intrusion above Mars crustal fields – Mars Express ASPERA-3 observations, *Icarus*, *182*, 406–412, doi: 10.1016/j.icarus.2005.11.016.
- Glassmeier, K.-H., I. Richter, A. Diedrich, G. Musmann, U. Auster, U. Motschmann, A. Balogh, C. Carr, E. Cupido, A. Coates, M. Rother, K. Schwingenschuh, K. Szegö, and B. Tsurutani (2007), RPC-MAG The Fluxgate Magnetometer in the ROSETTA Plasma Consortium, *Space Sci. Rev.*, *128*, 649–670, doi:10.1007/s11214-006-9114-x.
- Grard, R., A. Pedersen, S. Klimov, S. Savin, and A. Skalskii (1989), First measurements of plasma waves near Mars, *Nature*, *341*, 607–609, doi: 10.1038/341607a0.
- Gurnett, D. A., D. L. Kirchner, R. L. Huff, D. D. Morgan, A. M. Persoon, T. F. Averkamp, F. Duru, E. Nielsen, A. Safaeinili, J. J. Plaut, and G. Picardi (2005), Radar Soundings of the Ionosphere of Mars, *Science*, *310*, 1929–1933, doi:10.1126/science.1121868.
- Halekas, J., and D. Brain (2009), Global distribution, structure, and solar wind control of low altitude current sheets at mars, *Icarus*, *In Press*, doi: 10.1016/j.icarus.2008.12.032.
- Halekas, J. S., D. A. Brain, R. J. Lillis, M. O. Fillingim, D. L. Mitchell, and R. P. Lin (2006), Current sheets at low altitudes in the Martian magnetotail, *Geophys. Res. Lett.*, *33*, L13,101, doi:10.1029/2006GL026229.
- Hanson, W. B., S. Sanatani, and D. R. Zuccaro (1977), The Martian ionosphere as observed by the Viking retarding potential analyzers, *J. Geophys. Res.*, *82*, 4351–4363.

- Harnett, E. M., and R. M. Winglee (2003), The influence of a mini-magnetopause on the magnetic pileup boundary at Mars, *Geophys. Res. Lett.*, *30*, 10–1.
- Harnett, E. M., and R. M. Winglee (2007), High-resolution multifluid simulations of the plasma environment near the Martian magnetic anomalies, *J. Geophys. Res.*, *112*, A05,207, doi:10.1029/2006JA012001.
- Hinson, D. P., R. A. Simpson, J. D. Twicken, G. L. Tyler, and F. M. Flasar (1999), Initial results from radio occultation measurements with Mars Global Surveyor, *J. Geophys. Res.*, *104*(E11), 26,997–27,012, doi:10.1029/1999JE001069.
- Israelevich, P. L., F. M. Neubauer, and A. I. Ershkovich (1994), The induced magnetosphere of comet Halley: Interplanetary magnetic field during Giotto encounter, *J. Geophys. Res.*, *99*(A4), 6575–6583.
- Kallio, E., and P. Janhunen (2002), Ion escape from Mars in a quasi-neutral hybrid model, *Journal of Geophysical Research (Space Physics)*, *107*, A31,035, doi:10.1029/2001JA000090.
- Kallio, E., A. Fedorov, E. Budnik, S. Barabash, R. Jarvinen, and P. Janhunen (2008), On the properties of O^+ and O_2^+ ions in a hybrid model and in Mars Express IMA/ASPERA-3 data: A case study, *Planet. and Space Sci.*, *56*, 1204–1213, doi:10.1016/j.pss.2008.03.007.
- Kaneda, K., N. Terada, and S. Machida (2009), Solar-wind control of the hot oxygen corona around Mars, *Journal of Geophysical Research (Planets)*, *114*, E02,007, doi:10.1029/2008JE003234.
- Langlais, B., M. E. Purucker, and M. Manda (2004), Crustal magnetic field of Mars, *J. Geophys. Res.*, *109*, E02,008, doi:10.1029/2003JE002048.
- Lundin, R., H. Borg, B. Hultqvist, A. Zakharov, and R. Pellinen (1989), First measurements of the ionospheric plasma escape from Mars, *Nature*, *341*, 609–612, doi:10.1038/341609a0.
- Lundin, R., A. Zakharov, R. Pellinen, H. Borg, B. Hultqvist, N. Pissarenko, E. M. Dubinin, S. W. Barabash, I. Liede, and H. Koskinen (1990), Plasma composition measurements of the Martian magnetosphere morphology, *Geophys. Res. Lett.*, *17*, 877–880.
- Lundin, R., S. Barabash, A. Fedorov, M. Holmström, H. Nilsson, J.-A. Sauvaud, and M. Yamauchi (2008), Solar forcing and planetary ion escape from Mars, *Geophys. Res. Lett.*, *35*, L09,203, doi:10.1029/2007GL032884.

- Ma, Y., A. F. Nagy, I. V. Sokolov, and K. C. Hansen (2004), Three-dimensional, multispecies, high spatial resolution MHD studies of the solar wind interaction with Mars, *J. Geophys. Res.*, *109*, A07,211, doi:10.1029/2003JA010367.
- Mazelle, C., D. Winterhalter, K. Sauer, J. G. Trotignon, M. H. Acuña, K. Baumgärtel, C. Bertucci, D. A. Brain, S. H. Brecht, M. Delva, E. Dubinin, M. Øieroset, and J. Slavin (2004), Bow Shock and Upstream Phenomena at Mars, *Space Sci. Rev.*, *111*, 115–181, doi:10.1023/B:SPAC.0000032717.98679.d0.
- Mitchell, D. L., R. P. Lin, C. Mazelle, H. Rème, P. A. Cloutier, J. E. P. Connerney, M. H. Acuña, and N. F. Ness (2001), Probing Mars' crustal magnetic field and ionosphere with the MGS Electron Reflectometer, *J. Geophys. Res.*, *106*(E10), 23,419 – 23,427, doi:10.1029/2000JE001435.
- Modolo, R., G. M. Chanteur, E. Dubinin, and A. P. Matthews (2006), Simulated solar wind plasma interaction with the Martian exosphere: influence of the solar EUV flux on the bow shock and the magnetic pile-up boundary, *Ann. Geophys.*, *24*, 3403–3410.
- Morgan, D. D., D. A. Gurnett, D. L. Kirchner, J. L. Fox, E. Nielsen, and J. J. Plaut (2008), Variation of the Martian ionospheric electron density from Mars Express radar soundings, *J. Geophys. Res.*, *113*, A09,303, doi:10.1029/2008JA013313.
- Nagy, A. F., D. Winterhalter, K. Sauer, T. E. Cravens, S. Brecht, C. Mazelle, D. Crider, E. Kallio, A. Zakharov, E. Dubinin, M. Verigin, G. Kotova, W. I. Axford, C. Bertucci, and J. G. Trotignon (2004), The plasma environment of Mars, *Space Sci. Rev.*, *111*, 33–114, doi:10.1023/B:SPAC.0000032718.47512.92.
- Nilsson, H., E. Carlsson, D. A. Brain, M. Yamauchi, M. Holmström, S. Barabash, R. Lundin, and Y. Futaana (2009), Ion escape from mars as a function of solar wind conditions: A statistical study, *Icarus*, *In press*, doi:10.1016/j.icarus.2009.03.006.
- Pätzold, M., S. Tellmann, B. Häusler, D. Hinson, R. Schaa, and G. L. Tyler (2005), A Sporadic Third Layer in the Ionosphere of Mars, *Science*, *310*, 837–839, doi:10.1126/science.1117755.
- Pedersen, A., B. Lybekk, M. André, A. Eriksson, A. Masson, F. Mozer, P.-A. Lindqvist, P. Décréau, I. Dandouras, J.-A. Sauvaud, A. Fazakerley, G. Taylor, G. Paschmann, K. Svenes, K. Torkar, and E. Whipple (2008), Electron density estimations derived from spacecraft potential measurements

- on Cluster in tenuous plasma regions, *J. Geophys. Res.*, *113*, A07S33, doi:doi:10.1029/2007JA012636.
- Pérez-de-Tejada, H., R. Lundin, H. Durand-Manterola, and M. Reyes-Ruiz (2009), Solar wind erosion of the polar regions of the Mars ionosphere, *J. of Geophys. Res.*, *114*, A02,106, doi:10.1029/2008JA013295.
- Purucker, M., D. Ravat, H. Frey, C. Voorhies, T. Sabaka, and M. Acuña (2000), An altitude-normalized magnetic map of Mars and its interpretation, *Geophys. Res. Lett.*, *27*, 2449–2452, doi:10.1029/2000GL000072.
- Rosenbauer, H., M. I. Verigin, G. A. Kotova, S. Livi, A. P. Remizov, W. Riedler, K. Schwingenschuh, N. M. Shutte, J. A. Slavin, and K. Szego (1994), The relationship between the magnetic field in the Martian magnetotail and upstream solar wind parameters, *J. Geophys. Res.*, *99*(A9), 17,199–17,204, doi:10.1029/94JA00946.
- Russell, C. T., E. Chou, J. G. Luhmann, P. Gazis, L. H. Brace, and W. R. Hoegy (1988), Solar and interplanetary control of the location of the Venus bow shock, *J. Geophys. Res.*, *93*, 5461–5469, doi:10.1029/JA093iA06p05461.
- Sauer, K., T. Roatsch, U. Motschmann, D. Moehlmann, K. Schwingenschuh, R. Lundin, H. Rosenbauer, and S. Livi (1992), Multiple-ion effects at Martian plasma boundaries, *Adv. Space Res.*, *12*, 275–278, doi:10.1016/0273-1177(92)90340-4.
- Schwingenschuh, K., W. Riedler, H. Lichtenegger, Y. Yeroshenko, K. Sauer, J. G. Luhmann, M. Ong, and C. T. Russell (1990), Martian bow shock - Phobos observations, *Geophys. Res. Lett.*, *17*(9), 889–892.
- Slavin, J. A., and R. E. Holzer (1981), Solar wind flow about the terrestrial planets. I - Modeling bow shock position and shape, *J. Geophys. Res.*, *86*(A13), 11,401–11,418.
- Slavin, J. A., K. Schwingenschuh, W. Riedler, and E. Eroshenko (1991), The solar wind interaction with Mars - Mariner 4, Mars 2, Mars 3, Mars 5, and PHOBOS 2 observations of bow shock position and shape, *J. Geophys. Res.*, *96*(A7), 11,235–11,241.
- Smith, E. J., L. J. Davis, P. J. Coleman, Jr., and D. E. Jones (1965), Magnetic Field Measurements near Mars, *Science*, *149*, 1241–1242, doi:10.1126/science.149.3689.1241.
- Spreiter, J. R., and S. S. Stahara (1980), Solar wind flow past Venus - Theory and comparisons, *J. Geophys. Res.*, *85*, 7715–7738, doi:10.1029/JA085iA13p07715.

- Terada, N., Y. N. Kulikov, H. Lammer, H. I. M. Lichtenegger, T. Tanaka, H. Shinagawa, and T. Zhang (2009), Atmosphere and Water Loss from Early Mars Under Extreme Solar Wind and Extreme Ultraviolet Conditions, *Astrobiology*, *9*, 55–70, doi:10.1089/ast.2008.0250.
- Thiebault, B., A. Hilgers, A. Masson, C. P. Escoubet, and H. Laakso (2006), Simulation of the Cluster-spacecraft floating probe potential, *IEEE Proc. Plasma Sci.*, *34*, 2078–2083, doi:10.1109/TPS.2006.883407.
- Trotignon, J. G., R. Grard, and S. Savin (1991), Plasma wave system measurements of the Martian bow shock from the Phobos 2 spacecraft, *J. Geophys. Res.*, *96*(A7), 11,253–11,264.
- Trotignon, J. G., R. Grard, and A. Skalsky (1993), Position and shape of the Martian bow shock - The Phobos 2 plasma wave system observations, *Planet. Space Sci.*, *41*, 189–198, doi:10.1016/0032-0633(93)90058-A.
- Trotignon, J. G., E. Dubinin, R. Grard, S. Barabash, and R. Lundin (1996), Martian planetopause as seen by the plasma wave system onboard Phobos 2, *J. Geophys. Res.*, *101*(A11), 24,965–24,978, doi:10.1029/96JA01898.
- Trotignon, J. G., C. Mazelle, C. Bertucci, and M. H. Acuña (2006), Martian shock and magnetic pile-up boundary positions and shapes determined from the Phobos 2 and Mars Global Surveyor data sets, *Planet. Space Sci.*, *54*, 357–369, doi:10.1016/j.pss.2006.01.003.
- Verigin, M. I., K. I. Gringauz, G. A. Kotova, A. P. Remizov, N. M. Shutte, H. Rosenbauer, S. Livi, A. Richter, W. Riedler, K. Schwingenschuh, K. Szego, I. Apathy, and M. Tatrallyay (1993), The dependence of the Martian magnetopause and bow shock on solar wind Ram pressure according to PHOBOS 2 TAUS ion spectrometer measurements, *J. Geophys. Res.*, *98*(A2), 1303–1309, doi:10.1029/92JA01666.
- Vignes, D., C. Mazelle, H. Reme, M. H. Acuña, J. E. P. Connerney, R. P. Lin, D. L. Mitchell, P. Cloutier, D. H. Crider, and N. F. Ness (2000), The solar wind interaction with Mars: locations and shapes of the bow shock and the magnetic pile-up boundary from the observations of the MAG/ER experiment onboard Mars Global Surveyor, *Geophys. Res. Lett.*, *27*(1), 49–52, doi:10.1029/1999GL010703.
- Vignes, D., M. H. Acuña, J. E. P. Connerney, D. H. Crider, H. Rème, and C. Mazelle (2002), Factors controlling the location of the bow shock at Mars, *Geophys. Res. Lett.*, *29*(9), 1328, doi:10.1029/2001GL014513.
- Withers, P. (2009), A review of observed variability in the dayside ionosphere of mars, *Adv. Space Res.*, *44*(3), 277 – 307, doi:10.1016/j.asr.2009.04.027.

-
- Withers, P., M. Mendillo, H. Rishbeth, D. P. Hinson, and J. Arkani-Hamed (2005), Ionospheric characteristics above Martian crustal magnetic anomalies, *Geophys. Res. Lett.*, *32*, L16,204, doi:10.1029/2005GL023483.